

**Block Copolymer Photonic Crystals:
Towards Self-Assembled Active Optical Elements**

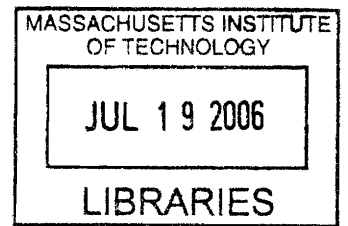
by
Jongseung Yoon

B.Sc. Fiber and Polymer Science, *Summa Cum Laude*
Seoul National University, February 1996

Submitted to the Department of Materials Science and Engineering
In Partial Fulfillment of the Requirements for the Degree of

DOCTOR OF PHILOSOPHY IN POLYMERS
at the
MASSACHUSETTS INSTITUTE OF TECHNOLOGY
June 2006

© 2006 Massachusetts Institute of Technology.
All rights reserved.



ARCHIVES

Signature of Author:
Department of Materials Science and Engineering
May 26, 2006

Certified by:
Edwin L. Thomas
Morris Cohen Professor of Materials Science and Engineering
Thesis Supervisor

Accepted by:
Samuel M. Allen
POSCO Professor of Physical Metallurgy
Chairman, Department Committee on Graduate Students

Block Copolymer Photonic Crystals: Towards Self-Assembled Active Optical Elements

by
Jongseung Yoon

Submitted to the Department of Materials Science and Engineering
on May 26, 2006 in Partial Fulfillment of the Requirements for the Degree of
Doctor of Philosophy in Materials Science and Engineering

ABSTRACT

Block copolymers have proven to be a unique materials platform for easily fabricated large-area photonic crystals. While the basic concept of block copolymer based photonic band gap materials has been well demonstrated, little work has been achieved yet in terms of realizing optically active devices using these materials. In this thesis, the utilization of block copolymer photonic crystals for creating self-assembled active optical elements has been experimentally explored with a special emphasis on optically driven lasing and stimulus responsive tunable reflectors. In pursuing these primary objectives, control of thin film microdomain orientation and novel three-dimensional (3D) optical characterization of block copolymer photonic crystals have been also achieved, both of which can greatly help optimize the properties of block copolymer photonic crystals.

First, a laser cavity using block copolymer based one-dimensional (1D) photonic crystals has been demonstrated. Optically pumped surface-emitting lasing has been obtained using a dye-doped polymers as the organic gain medium and the self-assembled block copolymer as the spectral-band selective distributed Bragg reflector feedback element. We also developed a novel organic/inorganic hybrid photonic crystal containing a dye-doped defect layer for defect-mode photonic bandgap lasing. Low threshold lasing has been demonstrated at a single defect-mode wavelength of the 1D photonic bandgap structure resulting from the inhibited density of states of photons within the stop band and the enhanced rates of spontaneous emission at the localized resonant defect mode.

Second, stimulus responsive tunable self-assembled reflectors based on 1D block copolymer photonic crystals have been studied. Three external stimuli such as solvent, temperature, and compressive mechanical strain have been employed to modulate microstructural and material properties of block copolymer photonic crystals, resulting in effective tuning of the spectral characteristics of block copolymer photonic structures.

Finally, control of the microdomain orientation of 1D and 2D block copolymer photonic crystals has been achieved over a large area via directional solidification of solvent. Moreover, an intriguing ordering behavior of these ultrahigh molecular weight block copolymers has been revealed, which is dramatically different from that of typical molecular weight block copolymers. These highly oriented thin film microdomain patterns have been explored via 3D optical imaging using laser scanning confocal microscopy.

Thesis Supervisor: Edwin L. Thomas

Title: Morris Cohen Professor of Materials Science and Engineering

TABLE OF CONTENTS

List of Figures	6
List of Tables	15
Acknowledgements	16
Foreword	18
Motivation and Objective	18
Thesis Overview	19
Chapter 1. Introduction to Block Copolymer based Photonic Bandgap Materials	22
1.1. Photonic Crystals	23
1.2. 1D, 2D, and 3D Block Copolymer Photonic Crystals	25
1.3. Nanocomposite Block Copolymer Photonic Materials	34
1.4. Switchable Block Copolymer Photonics	36
1.5. Challenges, Advantages, and Applications	37
1.6. References	40
Chapter 2. Materials and Experimental Methods	46
2.1. High Molecular Weight Block Copolymers	47
2.1.1. Purification of glassware, syringes, needles	48
2.1.2. Purification of solvents	49
2.1.3. Purification of monomers	49
2.1.4. Polymerization and molecular characterization	50
2.2. Microstructural Characterization	52
2.2.1. Solution casting	52
2.2.2. Cryomicrotomy and transmission electron microscopy (TEM)	52
2.2.3. Laser scanning confocal microscopy (LSCM)	53
2.2.4. Ultrasmall angle X-ray scattering (USAXS)	53
2.3. Optical Characterization	54
2.3.1. Reflectivity measurement	54
2.3.2. Absorption and emission measurements	55
2.3.3. Lasing measurements	56
2.4. References	58

Chapter 3. Defect-Mode Mirror-less Lasing in a Dye-doped Organic/Inorganic.....	59
Hybrid 1D Photonic Crystal	
3.1 Introduction	60
3.2 Results and Discussion	61
3.3 Conclusion.....	71
3.4 References	73
Chapter 4. Optically Pumped Surface-Emitting Lasing using Self-Assembled.....	76
Distributed Bragg Reflectors from 1D Block Copolymer Photonic Crystal	
4.1 Introduction	77
4.2 Results and Discussion	78
4.3 Conclusion.....	90
4.4 References	91
Chapter 5. Chemically, Thermally, Mechanically Responsive Tunable	94
Self-Assembled Reflectors based on Block Copolymer Photonic Crystals	
5.1 Introduction	95
5.2 Results and Discussion	96
5.3 Conclusion.....	123
5.4 References	126
Chapter 6. Highly Oriented Thin Film Microdomain Patterns of Ultrahigh	129
Molecular Weight Photonic Block Copolymers via Directional Solidification	
of a Solvent	
6.1 Introduction	130
6.2 Results and Discussion	131
6.3 Conclusion.....	143
6.4 References	145
Chapter 7. Summary and Future Work	149
7.1. Research Summary.....	150
7.2. Future Work.....	152
7.3. References	157

Appendix. Polyolefin based Photonic Bandgap Materials.....	159
A.1 Introduction	160
A.2 Experimental.....	161
A.2.1.1. Synthesis.....	161
A.2.1.2. Characterization.....	162
A.3 Results and Discussion	165
A.4 Conclusion	181
A.5 References.....	183

LIST OF FIGURES

Figure 1.1: A schematic diagram of 1D, 2D, 3D periodic photonic crystals composed of high (blue) and low (green) refractive index domains. This diagram was adopted from [5].

..... 24

Figure 1.2: A schematic diagram showing various bulk morphologies of linear diblock copolymer, poly(A-b-B), as a function of volume fraction of A block (The double diamond bicontinuous network structure does not occur for simple diblocks). This diagram was adopted from Dr. Banita Dair..... 27

Figure 1.3: 1D, 2D, 3D photonic crystals from (a) lamellar (from [26]) (b) cylindrical (from [32]) and (c) double gyroid (from [36]) morphologies of PS-b-PI block copolymers, respectively. Figure 1.3(a) is a TEM image of an OsO₄ stained PS-b-PI diblock, Figure 1.3(b) is an AFM image of cylindrical PS-b-PI diblock, Figure 1.3 (c) is a SEM image of ozone-etched double gyroid PS-b-PI diblock..... 28

Figure 1.4: A band diagram (dimensionless frequency vs. dimensionless wavevector) using the refractive indices of polystyrene ($n_{PS} = 1.59$) and polyisoprene ($n_{PI} = 1.51$) and the layer thicknesses of a PS-b-PI block copolymer ($d_{PS} = d_{PI} = 100$ nm). The transverse-electric (TE) polarization modes are on the right side, and the left side is for the transverse-magnetic (TM) polarized light. The numerical code was written by Dr. Martin Maldovan at MIT. (c: speed of light in a vacuum, a: lamellar domain periodicity = $d_{PS} + d_{PI}$)..... 30

Figure 1.5: Reflectivity plot constructed by the transfer matrix method for a 20-period stack of alternating PS ($n = 1.59$) and PI ($n = 1.51$) layers (glass substrate-(PS layer-PI layer)²⁰-air), for TM (left) and TE polarization (right), respectively. Each layer is assumed to be 100 nm thick. The color represents the strength of the reflectivity at a particular polarization, frequency, and angle of incidence of incident light. 31

Figure 2.1: A schematic of the experimental setup for measuring emission and lasing spectra..... 57

Figure 3.1: Bright-field TEM micrograph of surface-protected titania (TiO ₂) nanoparticles on carbon film, in which well-dispersed and monodisperse nanoparticles having an average diameter of about 4 nm are evident.	62
Figure 3.2: Powder XRD spectrum of surface-protected titania (TiO ₂) nanoparticles, in which the reflection peaks are well matched with those of <i>anatase</i> phase titania.	63
Figure 3.3: Linear absorption and photoluminescence spectra of DCM (0.5 wt %, 400 nm excitation) in PMMA. The molecular structure of DCM is shown in the inset. The FWHM of the PL spectrum is about 75 nm and the peak of the spontaneous emission occurs at 582 nm.	63
Figure 3.4: Schematic of dye-doped defect-mode 1D photonic crystal, glass-(PMMA-TiO ₂) ¹⁵ -(DCM/PMMA)-(TiO ₂ -PMMA) ¹⁵ -air.	65
Figure 3.5: TMM calculated reflectivity spectrum of the defect-mode 1D photonic crystal, glass-(PMMA-TiO ₂) ¹⁵ -(DCM/PMMA)-(TiO ₂ -PMMA) ¹⁵ -air, at normal incidence. Arrows indicate the localized defect-modes created by the PMMA defect layer.	66
Figure 3.6; Calculated density of states of photons, $\rho(\omega) \equiv dk/d\omega$, of the defect-mode 1D photonic crystal, glass-(PMMA-TiO ₂) ¹⁵ -(DCM/PMMA)-(TiO ₂ -PMMA) ¹⁵ -air, in which the y-axis shows the normalized $\rho(\omega)$ with respect to the value in vacuum ($\rho(\omega)_{vac} = 1/c$)..	66
Figure 3.7: Measured reflectivity spectrum of the fabricated defect-mode 1D photonic crystal at near normal incidence using a reflection-mode optical microscope connected to a fiber-optic spectrometer, in which the spectrum represents a convolution of multiple reflectivity spectra over the incidence angles of 0° to ~17.5° due to the numerical aperture of the objective lens (10X, N.A. = 0.3). Experimental features indicative of the two defect modes are shown..	67
Figure 3.8: Photograph of the 582 nm lasing from the defect-mode 1-D photonic crystal. A highly directional lasing in the backward direction was observed on a white background.	68

Figure 3.9: The lasing spectrum obtained at a pump power of 1 mW, above the lasing threshold. The two small peaks beside the lasing line at 582 nm correspond to the excitation light (532 nm) and to the low frequency defect mode (at 620 nm, below its lasing threshold for this pump power). 70

Figure 3.10: Emission intensity and line-width (the full width at half maximum, FWHM) at the lasing wavelength (582 nm) as a function of pump power. The behavior of the intensity and the FWHM clearly demonstrate a threshold for lasing around 0.6 mW pump power (12 μ J pulse energy). 70

Figure 4.1: Bright-field TEM micrograph of cryomicrotomed PS-b-PI block copolymer showing a 1D periodic lamellar morphology, in which the dark regions correspond to PI domains preferentially stained with OsO₄ and the bright regions correspond to PS domains. The domain periodicity is approximately 140 nm (PS: 76 nm, PI: 64 nm)..... 79

Figure 4.2: Experimental reflectivity spectrum of the fabricated block copolymer based distributed Bragg reflector at near normal incidence using a reflection-mode optical microscope connected to a fiber-optic spectrometer. The inset shows a calculated reflectivity spectrum using the transfer matrix method at a normal incidence for a finite 1D periodic structure, assuming 300 layers of PS (76 nm, $n = 1.59$) and PI domains (64 nm, $n = 1.51$)..... 80

Figure 4.3: Photoluminescence (PL) spectrum from a solid film of Bis-MSB (0.1 wt %, 355 nm excitation) in PMMA. The FWHM of the PL spectrum is about 75 nm. The inset shows the absorption spectrum from the same sample, where the absorption maximum is located at around 350 nm..... 82

Figure 4.4: Schematic of the block copolymer based laser cavity, comprised of a gain medium, Bis-MSB and PMMA, enclosed between two block copolymer based distributed Bragg reflectors. The thicknesses of PS and PI domains are estimated values at 10 wt % solvent concentration based on the peak position and FWHM of the reflectivity spectrum. 83

Figure 4.5: A model laser cavity composed of a gain medium (length L) and two dielectric mirrors having reflectivity values of R_1 ($z = 0$) and R_2 ($z = L$). The blue arrow represents the power of the oscillating radiation. 84

Figure 4.6: Photograph of the 410 nm lasing from the block copolymer based laser structure. A highly directional lasing output in the backward direction was observed on a white background. 86

Figure 4.7: The emission spectra obtained at various pump powers. The FWHM of the lasing peak is 1 nm. Inset shows the emission intensity at the lasing wavelength (410 nm) as a function of pump power, which clearly shows a threshold for lasing at around 4 mW pump power (0.2 mJ pulse energy). 88

Figure 4.8: Lasing spectrum from a solid film of Bis-MSB (0.1 wt %) in PMMA sandwiched between an aluminum-coated mirror and a glass slide pumped by 355 nm pulse laser, where the lasing peak occurs at 425 nm and the FWHM is 4 nm. The inset shows a schematic of the sample..... 89

Figure 5.1: A schematic of a model 1D photonic crystal, air-(high index layer-low index layer)^N-glass substrate, with incident electromagnetic wave of a transverse-electric (TE) polarization (the electric field vector (\mathbf{E}) is perpendicular to the plane of incidence or parallel to the z -axis (\mathbf{z})). 97

Figure 5.2: Reflectivity spectra of model 1D photonic crystals at normal incidence as a function of the domain periodicity ($L = d_H + d_L$, $d_H = d_L$), assuming constant refractive indices ($n_H = 1.59$, $n_L = 1.51$) and fixed total number of layers ($2N = 50$). The peak reflectivity wavelength at each domain periodicity is shown in the inset. 98

Figure 5.3: Reflectivity spectra at normal incidence of a model 1D photonic crystal (Figure 5.1) as a function of the refractive index contrast (n_H/n_L), assuming constant domain thicknesses ($d_H = d_L = 100$ nm) and a fixed total number of layers ($2N = 20$). 100

Figure 5.4: Peak reflectivity of quarter-wave multilayer stacks (see the inset) at normal

incidence as a function of refractive index contrast (n_H/n_L) and a total number of layers ($2N$) from Equation 5.1. ($d_H = \lambda_0/4n_H$, $d_L = \lambda_0/4n_L$, \mathbf{k}_i : incident wave vector, \mathbf{k}_r : reflected wave vector, \mathbf{k}_t : transmitted wave vector). 100

Figure 5.5: Schematic of 1D photonic crystals having different domain orientations with respect to a certain direction of incident light (\mathbf{k}_i), (a) $\theta = 0^\circ$, (b) $\theta > 0^\circ$ 101

Figure 5.6: Reflectivity map computed by TMM for a 15-period ($2N = 30$) stack of alternating high and low index layers for (a) low refractive index contrast ($n_H/n_L = 1.59/1.51$) and (b) high refractive index contrast ($n_H/n_L = 2.27/1.51$) for TE (right) and TM (left) polarizations, assuming quarter-wave layer thicknesses of 500 nm and total 30 layers. The color represents the strength of the reflectivity at a particular frequency, a polarization, and an angle of incidence. The omnidirectional reflectivity band is shown for the high refractive index contrast 1D photonic crystal. 102

Figure 5.7: Bright field TEM micrograph of crymicrotomed PS-b-PI block copolymer, in which PI domains are preferentially stained with OsO₄. The domain periodicity from the TEM micrograph is approximately 200 nm (PS: 110 nm, PI: 90 nm). 104

Figure 5.8: A series of pictures taken from confined block copolymer gel at different solvent evaporation times (e.g. 2:40 means 2 h 40 min). These pictures were taken by Felice Frankel at MIT. 105

Figure 5.9: Reflectivity spectra taken in the early stage of solvent evaporation at various radial positions from the center to the edge with normal incident light using a microscope spectrometer. Note the continuous change in the peak wavelength with radial distance from the sample center. The sample in the photograph appears to the eye as having a large single color near the center, but the measured spectra show a significant variation of the actual color with radial position. 106

Figure 5.10: Effective refractive indices of PS (thick line) and PI (thin line) microdomains as a function of solvent concentration at various solvent refractive indices, (a) $n_s = 1.61 > n_H > n_L$, (b) $n_H > n_s = 1.55 > n_L$, (c) $n_H > n_L > n_s = 1.49$. Case (c) is relevant to the experiments on PS-b-PI with cumene ($n = 1.49$). 110

Figure 5.11: Average effective refractive indices ($n_{\text{avg}} = (n_{\text{eff, H}} + n_{\text{eff, L}})/2$) as a function of solvent concentration at various solvent refractive indices, (a) $n_s = 1.61 > n_H > n_L$, (b) $n_H > n_s = 1.55 > n_L$, (c) $n_H > n_L > n_s = 1.49$. Case (c) is relevant to the experiments on PS-b-PI with cumene ($n = 1.49$)..... 111

Figure 5.12: Measured reflectivity spectra of the block copolymer lamellar photonic gel at various temperatures between 30 °C and 140 °C..... 113

Figure 5.13: Peak reflectivity wavelengths obtained from TMM calculations with temperature-dependent refractive indices (red data points), with temperature-dependent domain thicknesses (blue data points), and with both temperature-dependent refractive indices and domain thicknesses at various temperatures. The observed peak reflectivity wavelengths (black data points) are also shown..... 120

Figure 5.14: Measured peak reflectivity wavelength (blue data points) versus sample thickness of mechanochromic block copolymer gel. The orange line is obtained from the TMM calculation. Inset shows photographs taken from the sample at different sample thicknesses..... 122

Figure 6.1: Reflection mode LSCM image (xy-scan) of PS-b-PI block copolymers showing highly-oriented lamellar microdomains in a thin film obtained from directional solidification process with benzoic acid (BA). Inter-material dividing surfaces (IMDSs) are principally aligned perpendicular to the fast growing direction of benzoic acid (the b-axis of BA crystal). The inset is a high magnification image of the edge-on lamellae, for which the lamellar periodicity ($d_{\text{LAM}} \sim 210$ nm) is shown..... 133

Figure 6.2: Reflection mode LSCM image (xy-scan) of PS-b-PI block copolymers showing highly-oriented cylindrical microdomains in a thin film obtained from directional solidification process with benzoic acid (BA). Inter-material dividing surfaces (IMDSs) are principally aligned perpendicular to the fast growing direction of benzoic acid (the b-axis of BA crystal) The inset is a high magnification image of the in-plane cylinders, for which the inter-cylinder spacing ($d_{\text{CYL}} \sim 260$ nm) is shown. 134

Figure 6.3: A low magnification LSCM image (xy-scan) of SI_{CYL} showing the relative orientation of cylindrical microdomains with respect to the fast-growth direction of BA crystal. 135

Figure 6.4: 3D reconstruction of reflection mode LSCM image of a highly-ordered lamellar PS-b-PI block copolymer in a thin film obtained from the DS process. 3D imaging revealed that lamellae were tilted by about 60° to the fast-growth direction of BA. Corresponding schematic with the direction of BA crystallization is also shown. 136

Figure 6.5: 3D reconstruction of reflection mode LSCM image of a highly-ordered cylindrical PS-b-PI block copolymer in a thin film obtained from the DS process. 3D imaging revealed cylindrical microdomains were hexagonally packed in the xz-plane. Corresponding schematic with the direction of BA crystallization is also shown. 137

Figure 6.6: Reflection-mode LSCM images (xy-scan) of PS-b-PI block copolymer (SI_{CYL}) taken every 220 nm along the z-axis on the same sample position. In each figure, three circled regions show the alternating registration of PS cylindrical domains (bright region) in PI matrix (dark region) along the z axis. 138

Figure 6.7: Schematic diagrams showing the hypothetical concentration profiles of block copolymer (ϕ_{BCP}) along \mathbf{b}_{BA} , the fast-growth direction of benzoic acid (BA) crystal during the DS process for (a) high and (b) low molecular weight block copolymer samples. The dotted lines represent BA crystallization front (α) and block copolymer microphase separation front (β). The insets show respective schematics of corresponding microdomain orientations with respect to \mathbf{b}_{BA} induced during the DS process. 141

Figure 7.1: Emission spectra of the self-assembled distributed feedback (DFB) laser structure enabled with PS-b-PI (320k/270k) block copolymer and Bis-MSB. The inset shows the pump power dependence of emission intensity of the block copolymer based DFB structure. 153

Figure A.1: Refractive index as a function of wavelength for polyolefin random copolymers measured by a spectroscopic ellipsometry, (a) poly(E-co-N) (entry 1 in Table 1),

(b) poly(MCP-*co*-VTM) (entry 3), (c) poly(E-*co*-P) (entry 2)..... 168

Figure A.2: Bright field TEM micrograph of cryomicrotomed section of the poly[(MCP-*co*-VTM)-*b*-(E-*co*-N)] block copolymer showing a lamellar morphology (domain periodicity ~ 170 nm). The dark regions ($l_{\text{MCP-}co\text{-VTM}} = 68$ nm) correspond to poly(MCP-*co*-VTM) microdomains preferentially stained with osmium tetroxide (OsO_4) and the bright regions ($l_{\text{E-}co\text{-N}} = 102$ nm) are poly(E-*co*-N) microdomains. 169

Figure A.3: Measured reflectivity spectrum of poly[(MCP-*co*-VTM)-*b*-(E-*co*-N)] lamellar film by a CARY spectrophotometer equipped with a diffusive reflectivity accessory. The peak reflectivity wavelength is around 470 nm..... 172

Figure A.4: Calculated reflectivity map of a multilayer stack having the same layer thickness and refractive index as poly[(MCP-*co*-VTM)-*b*-(E-*co*-N)] as a function of the incidence angle (x-axis), the polarization (x-axis), and the wavelength (y-axis) of the incident light, assuming the thickness of high (E-*co*-N)/low (MCP-*co*-VTM) index layer is 102 nm/68 nm, the refractive index of high/low index layer is 1.52/1.50, and a total number of 100 layers. The inset shows the reflectivity spectrum at normal incidence (incidence angle = 0°) as a function of wavelength, in which the peak reflectivity wavelength is 515 nm. 173

Figure A.5: Bright field TEM micrograph of cryomicrotomed section of the poly[(E-*co*-P)-*b*-(E-*co*-N)], in which the domain periodicity is 91 nm ($l_{\text{E-}co\text{-N}} = 56$ nm, $l_{\text{E-}co\text{-P}} = 35$ nm). The dark regions correspond to poly(E-*co*-N) microdomains preferentially stained with ruthenium tetroxide (RuO_4) and the bright regions correspond to poly(E-*co*-P) microdomains. Small particle-like entities in the micrographs come from ruthenium tetroxide (staining agent) aggregations..... 175

Figure A.6: Bright field TEM micrograph of cryomicrotomed section of the poly[(E-*co*-P)-*b*-(E-*co*-N)] ternary blend containing 20 wt % (10/10) homopolymers. The domain periodicity is 127 nm ($l_{\text{E-}co\text{-N}} = 79$ nm, $l_{\text{E-}co\text{-P}} = 48$ nm)..... 176

Figure A.7: Bright field TEM micrograph of cryomicrotomed section of the poly[(E-*co*-P)-

b-(*E-co-N*)] ternary blend containing 40 wt % (10/10) homopolymers. The domain periodicity is 152 nm ($l_{E-co-N} = 88$ nm, $l_{E-co-P} = 64$ nm)..... 177

Figure A.8: Smearred USAXS 1D line source data obtained from the polyolefin block copolymer films of (a) the poly[(*E-co-P*)-*b*-(*E-co-N*)] and ternary blends of the diblock containing (b) 20 wt % and (c) 40 wt % homopolymers. The (001) peaks for all three samples correspond well to the lamellar periods measured from TEM micrographs. 178

Figure A.9: Measured reflectivity spectra of (a) the poly[(*E-co-P*)-*b*-(*E-co-N*)] and ternary blends of the diblock containing (b) 20 wt % and (c) 40 wt % homopolymers by a CARY spectrophotometer equipped with a diffusive reflectivity accessory. The peak reflectivity wavelengths are (a) 268 nm (host diblock), (b) 335 nm (20 wt % blend), and (c) 448 nm (40 wt % blend), respectively..... 179

Figure A.10: Calculated reflectivity maps (for TE polarization of incident light) of multilayer stacks having the same layer thickness and refractive index as (a) poly[(*E-co-P*)-*b*-(*E-co-N*)], (b) 20 wt%, and (c) 40 wt% ternary blend as a function of the incidence angle (*x*-axis) and the wavelength (*y*-axis) of incident light, assuming that the thickness of high (*E-co-N*)/low (*E-co-P*) index layers are (a) 56 nm/35 nm, (b) 79 nm/48 nm, (c) 88 nm/64 nm as obtained from TEM, the refractive index of high/low index layer is 1.52/1.47 as obtained from ellipsometry, and a total number of 100 layers..... 180

LIST OF TABLES

Table 2.1: Molecular characteristics of the four photonic PS-b-PI block copolymers used in this thesis.	51
Table 5.1: Calculated normal incidence peak reflectivity wavelengths of a PS-b-PI photonic gel in a range of domain thicknesses with 10 wt % solvent concentration, assuming refractive indices of high and low index layers as 1.580 and 1.508, a fixed ratio of PS and PI domain thicknesses ($d_{PS}/d_{PI} = 1.1/0.9$), and total 400 layers.	114
Table 5.2: Effective refractive indices and effective domain thicknesses of PS and PI domains at various solvent concentrations determined from TMM calculations, which give a peak wavelength of the corresponding reflectivity spectrum at 510 nm.	115
Table 5.3: Effective refractive indices of PS and PI domains and peak reflectivity wavelengths at various temperatures obtained from TMM calculations, in which the domain spacings of the respective domains are held constant as the estimated values at 30 °C.	117
Table 5.4: Effective domain spacings of PS and PI domains and peak reflectivity wavelengths at various temperatures obtained from TMM calculations, in which the refractive indices of respective domains are held constant as the estimated values at 30 °C.	118
Table 5.5: Effective refractive indices, effective domain thicknesses of PS and PI domains, and peak reflectivity wavelengths at various temperatures obtained from TMM calculations.	119
Table A.1. Materials data for polyolefin copolymers.	166

ACKNOWLEDGEMENTS

Foremost, I am deeply indebted to Prof. Edwin L. Thomas, my Ph.D. advisor for his continuous support, encouragement, and insightful guidance. Ned has been my role model of a great scientist, advisor, and educator. All of my academic achievements at MIT would not have been possible without his sincere dedication to his students and his willingness to share his knowledge, motivation, and ideas.

I am also very grateful to my thesis committee members, Prof. Samuel Allen and Prof. Michael Rubner for their valuable comments and suggestions on my thesis.

I would also like to express my gratitude to my academic advisors at Seoul National University, Prof. Jae-Ryun Youn, and Prof. Won-Ho Jo for their support in my pursuing Ph. D. at MIT.

I have been fortunate over the past years to have many precious collaborators. I am particularly grateful to Dr. Wonmok Lee for his unselfish mentoring and help in many aspects of my thesis work. It is particularly memorable to me when we made our first breakthrough in the synthesis of ultrahigh molecular weight block copolymers after overcoming many obstacles. I am very grateful to Dr. Robert Mathers and Prof. Geoffrey Coates of Cornell University for their contribution to develop polyolefin based photonic bandgap materials. I would also like to express my gratitude to Dr. Peter DeRege and Dr. Apostolos Avgeropoulos for their useful advice on polymer synthesis. I would like to thank Dr. Jean-Michel Caruge, Dr. Steven Kooi, Dr. Jeff Baur, and Dr. Seong-Ho Cho of MIT for their help on optical measurements. I extend my thanks also to Prof. Rajeev Ram and Prof. Erich Ippen of MIT for their valuable comments on my research.

I am very thankful to Dr. Jinsang Kim and Dr. Cheolmin Park for their mentoring and guidance in my early years at MIT.

I would like to appreciate all members of Thomas group at MIT for their support and friendship, which made my life at MIT enjoyable. In particular, I would like to

acknowledge Augustine Urbas, Michael Bockstaller, Jiwoong Park, Chinedum Osuji, Chaitanya Ullal, Panitarn Wanakamol, Ion Bitu, Hyunjung Lee, Jihyun Jang, Joe Walish, Rafal Mickiewicz, Nick Tsui, Taeyi Choi, Melinda Cromie, Rachel Pytel, Taras Gorishnyy, and Martin Maldovan.

I also have so many wonderful Korean friends. I thank all Korean friends at MIT for their support and friendship. I extend my thanks to my lifetime friends including Sungjun Im, Woojin Chang, Wanhee Kim, and Youngjo Song.

I am grateful beyond words to my parents, Drs. Hyungwon Yoon and Kyungran Jeon for their unconditional love and sacrifice. I thank my sisters, Sumi and Suyoung, and my brother-in-law, Sangkwon Lee for their continued support. I would also like to express my deep gratitude to my uncle, Seokwon Yoon, and aunts for their endless support and encouragement. Among all I am eternally grateful to my grandmother for always believing in me, encouraging me, and teaching me so many invaluable lessons in life.

I dedicate this thesis to my greatest family.

Foreword

Motivation and Objective

Self-assembled block copolymer systems with an appropriate molecular weight to produce a domain size comparable to the wavelength of light have attained increasing attention as alternative building blocks to fabricate photonic crystals in the visible and near-IR frequencies. 1D, 2D, and 3D photonic crystals have been successfully demonstrated with various microdomain structures created through microphase separation of block copolymers. The size and shape of periodic microstructures of block copolymers can be readily tuned by controlling molecular parameters such as molecular weight, relative composition, chain architecture, and persistence length, or by blending with homopolymer or plasticizer. The versatility of block copolymer based photonic crystals is further increased by incorporating inorganic nanoparticles, liquid crystalline guest molecules (or using a liquid crystalline block) or selectively etching one of microdomains with the possibility to backfill with high index materials. There are many advantages for employing self-assembled block copolymers for photonic applications, which include the ease of processing; the ability to include both inorganic and organic materials within the block copolymer photonic crystal; and the fact that it is relatively easy to manipulate block copolymer photonic structures via numerous external fields.

Over the past decade, block copolymers have proven to be a unique and versatile materials platform for constructing large-area well-ordered photonic bandgap structures. While the idea of using block copolymer based photonic band gap materials as passive photonic structures has been well established, little work has been achieved yet for

realizing active photonic devices using these materials. The objective of this research is to create active photonic elements based on block copolymer photonic crystals, including photonic microcavities for optically driven lasing and stimulus responsive self-assembled reflectors for sensing and display applications. In pursuing these primary objectives, novel processing and characterization methods for optimizing photonic properties of block copolymer photonic crystals will be also explored.

Thesis Overview

This thesis is composed of seven chapters and one appendix. References are provided at the end of each chapter.

Chapter 1 serves as an introduction to block copolymer based photonic crystals and as a review on the previous studies of these materials upon which this thesis work has been built. The morphologies and optical properties of block copolymer based photonic crystals and block copolymer–nanoparticle composites are discussed and 1D, 2D, and 3D photonic crystals from lamellar-, cylinder-, and double-gyroid-forming diblock copolymers are illustrated. Nanocomposite photonic materials based on block copolymers and inorganic nanocrystals provide an essential way to enhance the inherent low dielectric contrast of neat block copolymers. Examples of switchable block copolymer-based photonic materials using external stimuli such as thermal and mechanical forces have been also demonstrated. The challenges in making block copolymers more useful as photonic materials are discussed, including attaining large

domain periodicities, attaining a high dielectric contrast, controlling the long-range domain order, and purposefully introducing specific defects.

Chapter 2 provides information about materials and experimental methods used in this research. Synthetic procedures and molecular characterizations of ultrahigh molecular weight poly(styrene-*b*-isoprene) (PS-*b*-PI) diblock copolymers are presented. Experimental techniques for microstructural characterization of the block copolymers such as ultrasmall angle X-ray scattering (USAXS), transmission electron microscopy (TEM), and laser scanning confocal microscopy (LSCM) are described. Finally, various spectroscopic techniques for optical characterization of block copolymer photonic crystals, organic laser dyes, and devices using these materials are summarized.

Chapter 3 describes results from our investigation of optically-pumped defect-mode lasing with a dye-doped organic/inorganic hybrid 1D photonic crystal. This defect-mode laser structure has been studied as a “model” system from which a basic understanding of the main factors affecting optically pumped lasing with dye-doped photonic crystals has been developed.

Chapter 4 explores a laser cavity enabled with block copolymer based photonic crystal. Polymeric distributed Bragg reflectors (DBRs) were prepared through the self-assembly of PS-*b*-PI lamellar diblock copolymer having a 1D photonic bandgap matching with the fluorescent emission spectrum of a gain medium. Optically pumped surface-emitting lasing is then demonstrated using the polymeric self-assembled DBR as a spectral-band selective feedback element.

Chapter 5 presents stimulus responsive tunable self-assembled reflectors using a lamellar block copolymer based photonic crystal. Three external stimuli, solvent, temperature, and compressive mechanical strain, have been used to modulate

microstructural and material properties of the PS-b-PI photonic block copolymer system, resulting in effective tuning of the spectral response of the self-assembled reflectors.

Chapter 6 shows how we can achieve excellent control of thin film microdomain orientation of lamellar- and cylinder-forming block copolymer photonic crystals over a large area via directional solidification of a solvent. Moreover, an intriguing ordering behavior of these ultrahigh molecular weight block copolymers, which is dramatically different from that of typical molecular weight block copolymers, has been revealed by 3D optical imaging via laser scanning confocal microscopy.

Chapter 7 presents a summary of accomplishments of this thesis work and suggests future research opportunities that can be continued based on the present work.

Appendix covers the results of the study into polyolefin based photonic bandgap materials, in which random copolymerization of olefin monomers was employed to tune the refractive index of each block and to suppress the crystallinity for optical transparency of the polyolefin based photonic structures.

Chapter 1.

Introduction to Block Copolymer based Photonic Bandgap Materials

Block copolymers spontaneously phase separate to form interesting microdomains on the length scale of the respective blocks. Various periodic microdomain structures of block copolymers can be created by tailoring molecular parameters such as molecular weight, composition, chain architecture, and the persistence lengths of constituent blocks. With advances in synthetic capability to prepare ultrahigh molecular weight (> 500 kg/mol) block copolymers having large domain sizes that can interact strongly with light of visible wavelength, block copolymers have emerged as promising candidate materials for constructing photonic crystals at optical and near infrared frequencies. In this chapter, we will briefly review the recent progress in the development of photonic-bandgap materials enabled with self-assembly of block copolymers, discussing the morphology and photonic properties of various block copolymer based photonic materials and nanocomposite additives.

Parts of this chapter were featured in: J. Yoon, W. Lee, E. L. Thomas *MRS Bulletin* 2005 721-726.

1.1. Photonic Crystals

Since their first concept was independently proposed by Yablonovitch¹ and John² in 1987, photonic crystals have been of intense interest for researchers because of their unique electromagnetic properties, particularly their ability to trap and guide the propagation of light, thus promising many revolutionary applications in the fields of optical communication and optoelectronics.^{3,4} Photonic crystals are defined as ordered structures with a periodic variation of the dielectric constants.⁵ The spatial periodicity and dimensionality of the crystal determine the photonic bandgap, a range of frequencies in which the propagation of electromagnetic waves is prohibited in certain crystallographic directions.^{6,7} For example, if the spatial periodicity of refractive index is along one direction, we call it a one-dimensional (1D) photonic crystal and a propagation of light having a wave vector component parallel to this direction is significantly affected due to the Bragg scattering at interfaces. Two- (2D) and three-dimensional (3D) photonic crystals are defined in a similar manner as schematically shown in Figure 1.1. The size of respective domains or the lattice constant of the photonic crystal is on the order of the wavelength of relevant electromagnetic waves.

Experimentally, a variety of processing methods have been used to construct photonic crystals operating at near-IR and optical frequencies. Lithographic methods based upon semiconductor fabrication techniques using masks have been widely utilized to make 2D photonic crystals and even some 3D photonic crystals, although fabrication of 3D photonic crystals by this approach requires many processing steps.⁸⁻¹⁰ Holography or

multiple-beam interference lithography holds much promise, especially for making 3D photonic structures with much less effort than conventional lithographic tools.^{11, 12} Many unconventional schemes such as two-photon lithography^{13, 14}, ink deposition¹⁵, and phase mask lithography¹⁶ have been also proposed to fabricate 3D photonic structures.

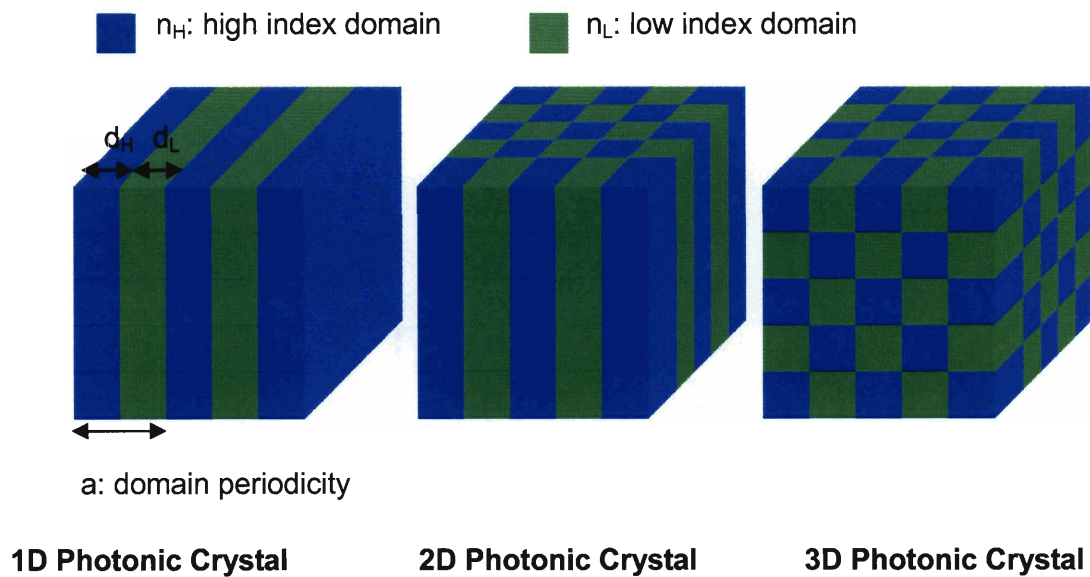


Figure 1.1: A schematic diagram of 1D, 2D, 3D periodic photonic crystals composed of high (blue) and low (green) refractive index domains. This diagram was adopted from [5].

Besides these *top-down* lithographic approaches, *bottom-up* self-assembly methods have also been actively pursued for making photonic-bandgap structures. Synthetic opals made of spherical silica or polymeric colloidal particles have been extensively studied.^{17, 18} The closed-packed structures yield the face-centered cubic (FCC) structure or, after infiltration by a second material and removal of the original spheres, the inverse FCC structure.¹⁹ More recently, block copolymers have emerged as alternative platform material for fabricating photonic crystals, because of their inherent flexibility in accessing a variety

of 1D, 2D, and 3D periodic structures; their ability to incorporate a wide choice of materials including the possibility of high-dielectric and optically active nanoparticle additives; and their relatively straightforward, cost-effective processing methods.²⁰

1.2. 1D, 2D, and 3D Block Copolymer Photonic Crystals

Photonic crystals will be an important part of future optical systems. For example, a discrete region of different index or geometry that serves to break the symmetry inside the photonic crystal can serve as an optical cavity, while a line defect can act as a waveguide and a surface defect can act like a mirror. As these features are all on the size scale of the wavelength of light, this affords both integration and miniaturization of optical devices. Even the most basic photonic crystal, a 1D multilayer stack in which the dielectric constant varies along only one direction, can act as a notch filter (a filter that can pass a narrow wavelength range of incident light) by incorporating a single defect layer in the stack. Multilayer devices are normally fabricated by various layer-by-layer approaches such as vacuum deposition, sputtering, co-extrusion, or spin-coating methods. Another way to produce 1D photonic crystals is by self-assembly of lamellar block copolymers.

Block copolymers, macromolecules comprising chemically distinct polymer chains covalently connected to each other, self-assemble to create a variety of periodic structures.²¹ The self-assembly of block copolymers is driven by a competition between the positive enthalpy of mixing of the respective block chains and the tendency for the

polymers to desire a random coil configuration. When χN is larger than a certain value (e.g., 10.5 for symmetric diblocks), where χ is the Flory–Huggins interaction parameter between blocks and N is the total degree of polymerization (equal to the total numbers of A monomers and B monomers) of the block copolymer, microphase separation into well-defined domain structures occurs on the length scale of the respective blocks. For example, in the case of simple linear A–B diblock copolymers, the volume fraction f and χN determine the four equilibrium morphologies: lamellae, double gyroid networks, hexagonally packed cylinders, and body-centered cubic (BCC) spheres, as schematically shown in Figure 1.2. The diversity of block copolymer microstructures in terms of microdomain size and shape is greatly increased by changing the number of components, the architecture, the persistence length (a measure of the local straightness of the polymer chain) of the constituting chains, or by blending with additives (homopolymers, plasticizers, etc.). For example, A–B–C terpolymers, in which three chemically different blocks are either connected in a series via two junctions or connected to a single junction to form miktoarm (“mixed arm” in Greek) star polymers, exhibit a range of more complex morphologies compared with simple diblock copolymers.²² The wide range of microstructures accessible from the self-assembly of block copolymers has made them excellent candidate materials for numerous nanotechnological applications, including photonic-bandgap materials.^{20, 23}

Block copolymers of typical molecular weight (~ 50 kg/mol) form microdomains on a typical length scale (~ 20 nm) that is insufficient for optical applications. What is needed in order to produce a bandgap at visible or near-IR wavelengths is to increase the average

domain size to on the order of $\lambda/4n_i$, where n_i is the index of refraction of the respective block and λ is the wavelength of light. For 600 nm visible (red) light, and for a typical polymer index of 1.5, this calls for an individual block layer thickness of approximately 100 nm, requiring a block molecular weight of ~ 500 kg/mol and a total polymer molecular weight of around 1,000 kg/mol. Such large domain spacings can also be accessed by employing somewhat lower-molecular-weight copolymers (e.g., ~ 200 kg/mol per block) and swelling the respective domains by blending with low-molecular-weight homopolymers or nonvolatile plasticizers, or by employing rigid, rodlike polymers with a large persistence length.

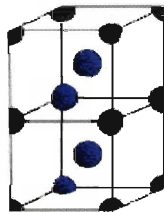
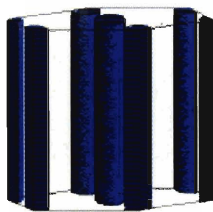
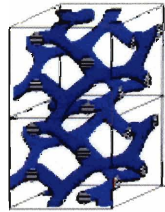
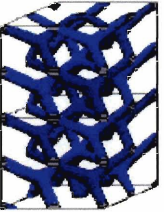

Nature of patterns	Spheres (SPH) (3D)	Cylinders (CYL) (2D)	Double gyroid (DG) (3D)	Double diamond (DD) (3D)	Lamellae (LAM) (1D)
Space group	$Im\bar{3}m$	$p6mm$	$Ia\bar{3}d$	$Pn\bar{3}m$	pm
Blue domains: A block					
Volume fraction of A block	0-21%	21-33%		33-37%	37-50%

Figure 1.2: A schematic diagram showing various bulk morphologies of linear diblock copolymer, poly(A-b-B), as a function of volume fraction of A block (The double diamond bicontinuous network structure does not occur for simple diblocks). This diagram was adopted from Dr. Banita Dair.

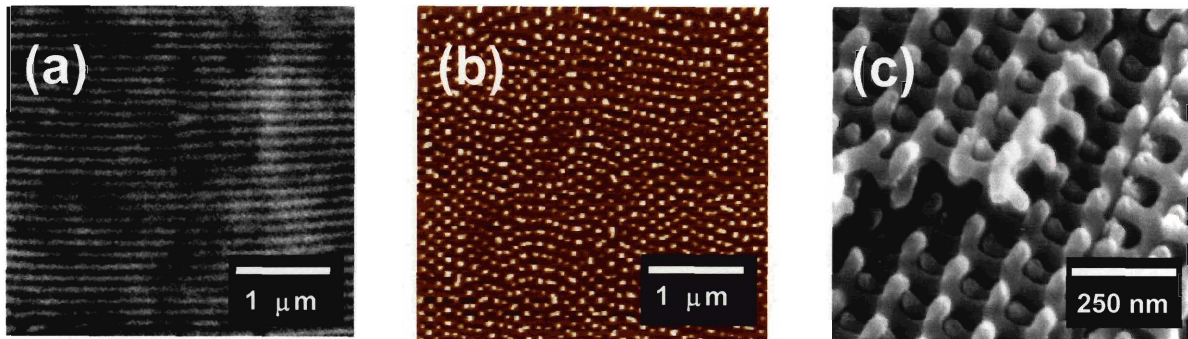


Figure 1.3: 1D, 2D, 3D photonic crystals from (a) lamellar (from [26]) (b) cylindrical (from [32]) and (c) double gyroid (from [36]) morphologies of PS-*b*-PI block copolymers, respectively. Figure 1.3(a) is a TEM image of an OsO₄ stained PS-*b*-PI diblock, Figure 1.3(b) is an AFM image of cylindrical PS-*b*-PI diblock, Figure 1.3 (c) is a SEM image of ozone-etched double gyroid PS-*b*-PI diblock.

The first example of a visible block copolymer photonic crystal was achieved by using a symmetric poly(styrene-*b*-isoprene) (PS-*b*-PI) diblock copolymer with approximate molecular weights of 200 kg/mol per block and forming a 60/20/20 ternary blend with the respective homopolymer of each block.^{24, 25} Indeed, the systematic blending of low-molecular-weight homopolymers into the host block copolymer provides a way to open the photonic bandgap (the so called “stop band”) across the entire visible wavelength range by simply controlling the amount of blended homopolymers.²⁶ More recently, block copolymers based on readily available olefins were developed to construct self-assembled photonic crystals of improved thermal stability and processability. Random copolymerization of olefin monomers provided a route to tune the refractive index of each block as well as to suppress the crystallinity for optical transparency. This work was in

collaboration with Dr. Robert Mathers and Prof. Geoffrey Coates at Cornell University (see appendix). Some examples of block copolymer based 1D, 2D, 3D photonic crystals are depicted in Figure 1.3.

A convenient way to understand the optical properties of a photonic crystal is to examine the dispersion relationship between the frequency ω and the direction of the wave vector \mathbf{k} of incident light. If we consider an infinite periodic medium, the $\omega(\mathbf{k})$ relationship can be derived from solutions to Maxwell's equations and is displayed as a band diagram.²⁷ The dispersion relationship of a 1D photonic crystal has been also analytically derived by Yeh et al.²⁸ Figure 1.4 is an illustration of the band diagram for a multilayer system with layer thicknesses and refractive indices illustrative of 1D photonic crystal of a lamellar-forming PS-b-PI block copolymer, and provides information on sample reflectivity as a function of incidence angle and polarization of the incident electromagnetic waves.^{29, 30} The areas between the first band (blue) and the second band (red) and above the third (red) band on the diagram represent propagating modes, while the areas between the second and the third band represent the nonpropagating evanescent modes. Light in this range of wavelengths incident for the particular $\mathbf{k}_{//}$ vector (a projected \mathbf{k} vector parallel to the interface between two domains) is reflected by constructive interference from the set of periodically spaced interfaces between the two types of domain. The plot also shows how the center wavelength of the bandgap is shifted to a shorter wavelength (or a higher frequency) as the incidence angle moves from normal ($\mathbf{k}_{//} = 0$) toward grazing (light line). Thus, a film appearing green when viewed at normal incidence appears blue when viewed at an angle far off the normal.

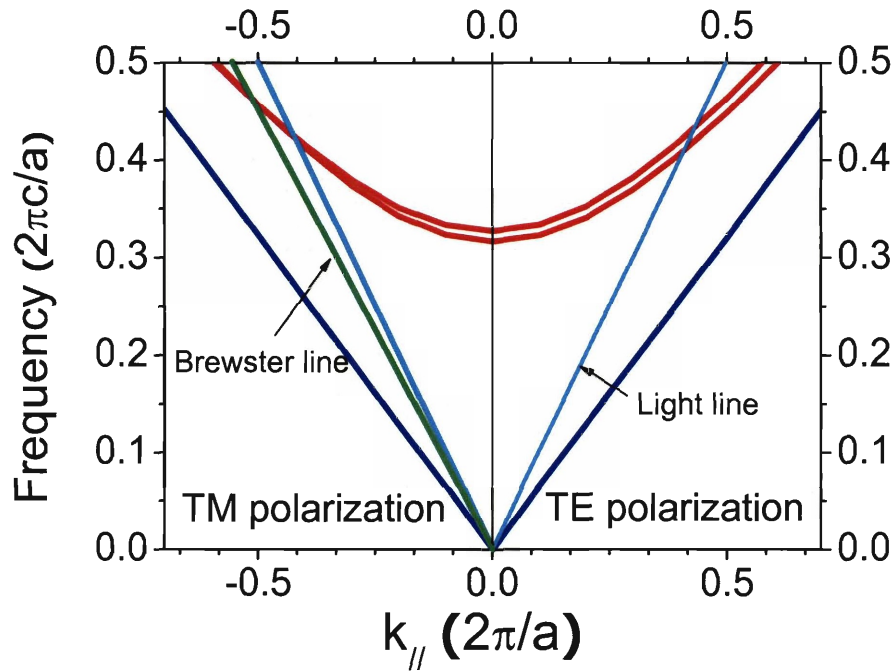


Figure 1.4: A band diagram (dimensionless frequency vs. dimensionless wavevector) using the refractive indices of polystyrene ($n_{PS} = 1.59$) and polyisoprene ($n_{PI} = 1.51$) and the layer thicknesses of a PS-*b*-PI block copolymer ($d_{PS} = d_{PI} = 100$ nm). The transverse-electric (TE) polarization modes are on the right side, and the left side is for the transverse-magnetic (TM) polarized light. The numerical code was written by Dr. Martin Maldovan at MIT. (c : speed of light in a vacuum, a : lamellar domain periodicity = $d_{PS} + d_{PI}$)

A second way to understand the same sort of reflectance data for a *finite* photonic crystal, which is more experimentally relevant, is to plot the magnitude of the reflectivity (this depends on the dielectric contrast (ϵ_2/ϵ_1) and, importantly, on the number of periods in the photonic crystal) as a function of polarization, wavelength, and incident angle of light as shown in Figure 1.5. This type of calculation can be done using the transfer matrix method³¹, which also allows one to include finite material absorption in the calculation as well as optical anisotropy.

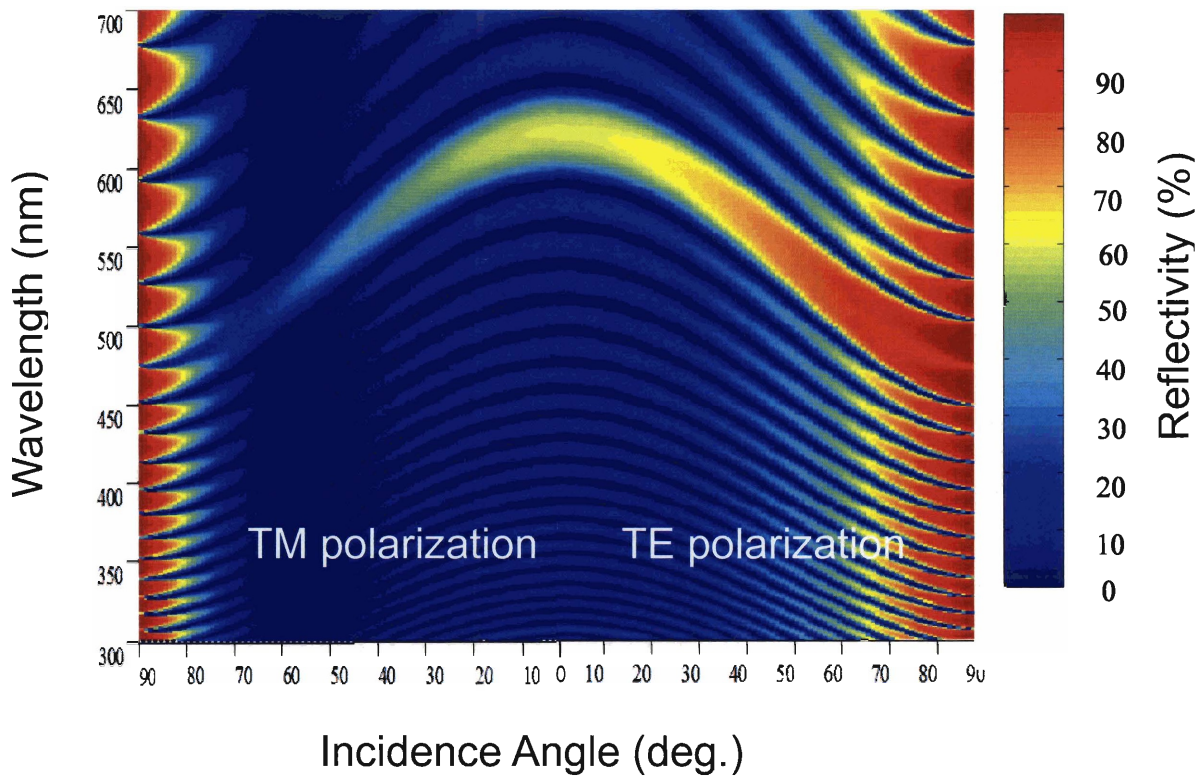


Figure 1.5: Reflectivity plot constructed by the transfer matrix method for a 20-period stack of alternating PS ($n = 1.59$) and PI ($n = 1.51$) layers (glass substrate-(PS layer-PI layer)²⁰-air), for TM (left) and TE polarization (right), respectively. Each layer is assumed to be 100 nm thick. The color represents the strength of the reflectivity at a particular polarization, frequency, and angle of incidence of incident light.

Two-dimensionally periodic block copolymer photonic crystals have been also demonstrated using self-assembly. In this case, a cylinder-forming PS-*b*-PI diblock copolymer was roll-cast to realize a long-range-ordered 2D periodic photonic crystal structure.³² The bandgap exists in the plane of the domain periodicity; thus, light propagating perpendicular to the cylinder axis is reflected. The small dielectric contrast

(~1.1) in the PS/PI material produced only a partial photonic bandgap. In order to achieve a complete bandgap for both transverse-electric (TE) and transverse-magnetic (TM) polarizations in the hexagonal cylinder structure, a minimum dielectric contrast of 7.2:1 is necessary. This illustrates the challenge to somehow access a much higher dielectric contrast than is inherent to polymeric systems.

A three-dimensionally periodic photonic crystal with a complete photonic bandgap in the optical or near-IR frequencies has been one of the main challenges for researchers since the inception of the field in 1987. Yablonovitch first proposed that a FCC arrangement of dielectric cubes would provide the sought-after complete bandgap.³³ Researchers attempted to create such a FCC photonic crystal structure using close-packed spheres, but the bandgap occurs at a relatively low volume fraction of dielectric, so infiltration of a high dielectric material about a template of FCC packed spheres, followed by etching to create an air lattice of spheres in a high dielectric was done.¹⁹ Unfortunately, the FCC structure does not have a complete bandgap between low-order bands, and the complete gap opens up between the eighth and ninth bands only at a relatively large dielectric contrast of nearly 9:1.³⁴ Since then, researchers have sought alternative structures that would provide a robust gap at a lower dielectric contrast that could also be readily fabricated. Interestingly, the current champion photonic-crystal structure is that of an interconnected diamond network first discovered by the Iowa State University group in 1991.³⁵ The 19 vol % diamond dielectric network displays a complete bandgap between the second and third bands at the record low dielectric contrast of 3.6:1 (note: attaining an

index contrast of 1.9:1 in a diamond network structure is not out of the question for polymer:air structures).

Block polymers can provide many possible intricate 3D structures through microphase separation. The first 3D block copolymer photonic crystal having a partial photonic bandgap was based on the bicontinuous double gyroid cubic morphology.³⁶ Here a PS-b-PI block copolymer with total molecular weight of 750 kg/mol provided domain sizes sufficient to interact with visible light.³⁶ The double gyroid morphology was further treated with UV and ozone to degrade the polyisoprene phase, leaving the polystyrene double gyroid network with increased refractive-index contrast (polystyrene versus air, 1.6:1, see Figure 1.3(c)).³⁶

However, it turns out that the double gyroid network structure does not possess a complete gap, no matter how high the dielectric contrast. This makes clear the need to perform simulations of potential structures to explore for robust bandgaps prior to undertaking extensive experiments. The Thomas group at MIT have used numerical calculations employing the plane wave method³⁴ to examine a host of network structures having various cubic symmetries.³⁷ What is done is to systematically explore the range of volume fractions and dielectric contrasts for a given structure to see if it displays a complete gap and then to construct a “gap map”—that is, a plot of the width of the complete gap (the difference in frequency of the lowest frequency of the upper band and the highest frequency of the lower band versus dielectric contrast at a fixed volume fraction). Of particular concern is finding the structure and the volume fraction of the structure at which a complete gap first opens at the lowest possible dielectric contrast. This

volume fraction will give the widest gap for a given dielectric contrast. It is noteworthy that neither the double gyroid nor the double diamond structures exhibit complete bandgaps, while both of the corresponding single network structures do, with the single diamond network as the current *champion* complete gap structure. The single gyroid morphology is also a quite favorable photonic crystal structure—a complete photonic bandgap opens at a index contrast of 2.3:1.³⁷

1.3. Nanocomposite Block Copolymer Photonic Materials

Given the inherently low refractive index contrast (n_2/n_1) in block copolymer-based photonic crystals (typically on the order of 1.1:1 for polymer:polymer structures and 1.5:1 for polymer:air structures) it is essential to enhance the index contrast in order to produce a more robust (or even complete) photonic bandgap. One method that has been successfully demonstrated is to selectively sequester high-refractive-index inorganic nanocrystals into the microdomains of a block copolymer to form an inorganic/organic microstructured nanocomposite photonic structure. For example, CdSe particles with trioctyl phosphine oxide (TOPO) surface ligands (CdSe refractive index, ~ 2.7) were successfully sequestered into the poly(vinyl pyridine) domains in a poly(styrene-*b*-isoprene-*b*-vinyl pyridine) block terpolymer.^{24, 29} In order to target the high-index nanoparticles to the higher-index block domains, one needs to tailor the nanocrystal surface to have compatibilizing groups (typically oligomeric homopolymers) similar to the host block domains. Thus, amine- or

thiol-terminated polystyrene was used to compatibilize CdSe nanocrystals into PS-*b*-PI block copolymers by ligand-exchange reactions. Since the electronic bandgap of semiconductor nanocrystals is inversely proportional to the size of the nanocrystals, the absorption band of nanocrystals is shifted to a shorter wavelength than in bulk materials, making the nanocrystals effectively transparent in the optical regime.

Metallic nanoparticles are also of interest for their extremely high dielectric constants. The optical response of block copolymer/metallodielectric nanocrystal photonic structures can be dramatically influenced by the spatial distribution of metallodielectric nanocrystals because of the dipolar coupling between closely spaced metal particles. For example, a metallodielectric photonic structure based on poly(styrene-*b*-ethylene/propylene) diblock copolymer and gold nanocrystals was coassembled using gold nanocrystals with a size well below the scattering limit.^{38, 39} The gold particles were surface-grafted with different chemical groups, such as thiol-terminated oligomeric polystyrene or thiol-terminated alkanes, to target a given type of microdomain in the block copolymer template. Two distinct spatial distributions of gold nanocrystals were observed: (1) interfacial segregation between the two block domains, or (2) preferential uniform distribution within one type of domain. These morphologies were dependent on the surface chemistry and size of the ligands attached to the particles.⁴⁰ The confinement of the nanocrystals to the narrow interface between domains results in a high local particle concentration and therefore a small average distance between particles, leading to different optical properties of the respective nanocomposite structures.⁴⁰

Thermodynamic prediction of block copolymer–nanoparticle phase diagrams is thus of importance in designing nanocomposites for applications. Balazs’ group has combined density functional theory and self-consistent field theory to simulate the behavior of nanoparticles of diameter d in block copolymer domains of period L . They showed that the interfacial segregation of nanoparticles with neutral ligands (i.e., $\chi = 0$) occurs for small particles ($d/L < 0.2$), whereas for $d/L \sim 0.3$, the particles locate in the center of the domain^{41, 42}, which was in reasonable agreement with experiments as well.^{39, 43} There are a host of parameters to explore concerning the localization of particles within block copolymer microdomains. These include the particle size and shape, ligand size and chemistry, and the size and shape of the particular host microdomain.⁴⁴ Information about the solubility limits of various particles in block copolymers is the key in understanding the attainable limits to the effective dielectric constant via blending. Clearly, there is much still to be done to control the hierarchical structures in block copolymer–nanoparticle assemblies that can enhance nanocomposite photonic properties.

1.4. Switchable BCP Photonics

Block copolymer-based photonic-bandgap materials that can be readily tuned or switched by applying various external fields can provide a route to fabricate multifunctional and optically responsive photonic structures. There is a host of ways to induce changes of

optical properties via alteration of the periodicity, symmetry, or dielectric constants of the material.

Thermally tunable block copolymer-based photonic-bandgap materials have been constructed by incorporating *guest* liquid-crystalline molecules into one domain of *host* block copolymers by hydrogen-bonding interaction to form a hierarchical photonic structure. Either the effective refractive index⁴⁵ or the lattice spacing⁴⁶ of liquid-crystal-containing domains could be changed as the temperature of the materials was changed, leading to the tailoring of the position and strength of the photonic stop band of the system.

Another way to alter the microdomain spacing in a block copolymer is to apply mechanical force. Elastomeric block copolymer photonic crystals have been prepared by blending with a nonvolatile plasticizer to form a block copolymer gel. The local deformation of the photonic gel's microstructure yields a tunable photonic bandgap with applied tensile strains.³⁰

Recently, chemically, thermally, mechanically responsive self-assembled reflectors based on PS-*b*-PI block copolymer solution have been nicely demonstrated and will be presented in Chapter 5 of this thesis.

1.5. Challenges, Advantages, and Applications

In order to maximize the usefulness of self-assembled block copolymer platforms, one has to address three major challenges: attaining large domain spacings, achieving high

dielectric contrast, and controlling long-range microdomain order. The occurrence of randomly located defects that accompany the self-assembly process must be avoided. In this regard, there have been numerous efforts to establish a single-crystal-like microdomain structure, employing various external fields such as mechanical flow fields, electric fields, temperature gradients, directional solidification, and surface interactions to obtain purposefully long-range domain order during the self-assembly process. However, the very high molecular weight block copolymers that are typical of photonic crystals presents the problem that the order–disorder transition is unattainable via temperature, so that solvents must be used to process the materials into their final structures, restricting the applicability of some of these techniques.

Advantages for employing self-assembled block copolymers as visible wavelength photonic materials include the ease of processing (e.g. conformal coating on essentially any substrate); the ability to incorporate both inorganic (e.g. quantum dots) and organic additives (e.g. laser dyes, liquid crystals, homopolymers, and plasticizers, etc.) within the block copolymer microdomains; and the relatively easy manipulation of block copolymer microstructures via various external fields such as mechanical force, temperature, and electric fields, etc.

As mentioned in the introduction, attainment of well-ordered photonic crystals is only a necessary requirement. Actual useful optical devices need *controlled defects* to localize and guide light. One interesting application is the use of the self-assembled block copolymer photonic crystal to define a microcavity for modifying the spontaneous emission of optically active materials, ultimately leading to an optically pumped, all-organic, self-

assembled laser. Clearly, 1D self-assembled photonic crystals from lamellar-forming block copolymers can act as a Bragg reflector. Two different types of laser structures can then be envisioned: (1) a distributed-feedback band-edge laser and (2) a defect-mode microcavity laser. For the distributed-feedback structure, a gain medium such as an organic laser dye is dispersed throughout the layered block copolymer structure. In the defect-mode approach, a layer of precise dimension containing the gain medium is employed as the microcavity, sandwiched by outside block copolymer Bragg reflectors. In both cases, controlling the microdomain orientation of the block copolymer lamellae is the key to obtaining the high quality factor (a ratio of the energy stored in resonant cavity to the energy lost per cycle) that is essential to enable lasing. This block copolymer enabled lasing device is one of main themes of this thesis work. Optically driven lasing using self-assembled distributed Bragg reflectors formed from a 1D block copolymer photonic crystal will be described in Chapter 4.

1.6. References

1. Yablonovitch, E. "Inhibited Spontaneous Emission in Solid-State Physics and Electronics" *Physical Review Letters* **1987**, 58, 2059-2062.
2. John, S. "Strong Localization of Photons in Certain Disordered Dielectric Superlattices" *Physical Review Letters* **1987**, 58, 2486-2489.
3. Vlasov, Y. A.; O'Boyle, M.; Hamann, H. F.; McNab, S. J. "Active control of slow light on a chip with photonic crystal waveguides" *Nature* **2005**, 438, 65-69.
4. Bayindir, M.; Sorin, F.; Abouraddy, A. F.; Viens, J.; Hart, S. D.; Joannopoulos, J. D.; Fink, Y. "Metal-insulator-semiconductor optoelectronic fibres" *Nature* **2004**, 431, 826-829.
5. Joannopoulos, J. D.; Meade, R. D.; Winn, J. N., *Photonic Crystals: Molding the Flow of Light*. Princeton University Press: Princeton, 1995.
6. Yablonovitch, E. "Photonic Band-Gap Structures" *Journal of the Optical Society of America B-Optical Physics* **1993**, 10, 283-295.
7. Joannopoulos, J. D.; Villeneuve, P. R.; Fan, S. H. "Photonic crystals: Putting a new twist on light" *Nature* **1997**, 386, 143-149.
8. Krauss, T. F.; DeLaRue, R. M.; Brand, S. "Two-dimensional photonic-bandgap structures operating at near infrared wavelengths" *Nature* **1996**, 383, 699-702.
9. Noda, S.; Tomoda, K.; Yamamoto, N.; Chutinan, A. "Full three-dimensional photonic bandgap crystals at near-infrared wavelengths" *Science* **2000**, 289, 604-

606.

10. Qi, M. H.; Lidorikis, E.; Rakich, P. T.; Johnson, S. G.; Joannopoulos, J. D.; Ippen, E. P.; Smith, H. I. "A three-dimensional optical photonic crystal with designed point defects" *Nature* **2004**, 429, 538-542.
11. Campbell, M.; Sharp, D. N.; Harrison, M. T.; Denning, R. G.; Turberfield, A. J. "Fabrication of photonic crystals for the visible spectrum by holographic lithography" *Nature* **2000**, 404, 53-56.
12. Ullal, C. K.; Maldovan, M.; Thomas, E. L.; Chen, G.; Han, Y. J.; Yang, S. "Photonic crystals through holographic lithography: Simple cubic, diamond-like, and gyroid-like structures" *Applied Physics Letters* **2004**, 84, 5434-5436.
13. Cumpston, B. H.; Ananthavel, S. P.; Barlow, S.; Dyer, D. L.; Ehrlich, J. E.; Erskine, L. L.; Heikal, A. A.; Kuebler, S. M.; Lee, I. Y. S.; McCord-Maughon, D.; Qin, J. Q.; Rockel, H.; Rumi, M.; Wu, X. L.; Marder, S. R.; Perry, J. W. "Two-photon polymerization initiators for three-dimensional optical data storage and microfabrication" *Nature* **1999**, 398, 51-54.
14. Kawata, S.; Sun, H. B.; Tanaka, T.; Takada, K. "Finer features for functional microdevices - Micromachines can be created with higher resolution using two-photon absorption" *Nature* **2001**, 412, 697-698.
15. Gratson, G. M.; Garcia-Santamaria, F.; Lousse, V.; Xu, M. J.; Fan, S. H.; Lewis, J. A.; Braun, P. V. "Direct-write assembly of three-dimensional photonic crystals: Conversion of polymer scaffolds to silicon hollow-woodpile structures" *Advanced Materials* **2006**, 18, 461-465.

16. Jeon, S.; Park, J. U.; Cirelli, R.; Yang, S.; Heitzman, C. E.; Braun, P. V.; Kenis, P. J. A.; Rogers, J. A. "Fabricating complex three-dimensional nanostructures with high-resolution conformable phase masks" *Proceedings of the National Academy of Sciences of the United States of America* **2004**, 101, 12428-12433.
17. Holland, B. T.; Blanford, C. F.; Stein, A. "Synthesis of macroporous minerals with highly ordered three-dimensional arrays of spheroidal voids" *Science* **1998**, 281, 538-540.
18. Braun, P. V.; Wiltzius, P. "Microporous materials - Electrochemically grown photonic crystals" *Nature* **1999**, 402, 603-604.
19. Wijnhoven, J.; Vos, W. L. "Preparation of photonic crystals made of air spheres in titania" *Science* **1998**, 281, 802-804.
20. Edrington, A. C.; Urbas, A. M.; DeRege, P.; Chen, C. X.; Swager, T. M.; Hadjichristidis, N.; Xenidou, M.; Fetters, L. J.; Joannopoulos, J. D.; Fink, Y.; Thomas, E. L. "Polymer-based photonic crystals" *Advanced Materials* **2001**, 13, 421-425.
21. Thomas, E. L.; Lescanec, R. L. "Phase morphology in Block Copolymer Systems" *Philosophical Transactions of the Royal Society of London A* **1994**, 348, 149-166.
22. Abetz, V., *Supramolecular Polymers, Chapter 6*. 2nd ed.; Marcel Dekker: New York, 2000.
23. Park, C.; Yoon, J.; Thomas, E. L. "Enabling nanotechnology with self assembled block copolymer patterns" *Polymer* **2003**, 44, 6725-6760.
24. Fink, Y.; Urbas, A. M.; Bawendi, M. G.; Joannopoulos, J. D.; Thomas, E. L. "Block

- copolymers as photonic bandgap materials" *Journal of Lightwave Technology* **1999**, 17, 1963-1969.
25. Urbas, A.; Fink, Y.; Thomas, E. L. "One-dimensionally periodic dielectric reflectors from self assembled block copolymer blends" *Macromolecules* **1999**, 32, 4748.
 26. Urbas, A.; Sharp, R.; Fink, Y.; Thomas, E. L.; Xenidou, M.; Fetters, L. J. "Tunable block copolymer/homopolymer photonic crystals" *Advanced Materials* **2000**, 12, 812-814.
 27. Plihal, M.; Maradudin, A. A. "Photonic Band-Structure Of 2-Dimensional Systems - The Triangular Lattice" *Physical Review B* **1991**, 44, 8565-8571.
 28. Yeh, P.; Yariv, A.; Hong, C. S. "Electromagnetic Propagation In Periodic Stratified Media.1. General Theory" *Journal of the Optical Society of America* **1977**, 67, 423-438.
 29. Fink, Y. *Polymeric Photonic Crystals. Ph.D. Thesis*, Massachusetts Institute of Technology, Cambridge, 2000.
 30. Urbas, A. M. *Block Copolymer Photonic Crystals. Ph. D. Thesis*, Massachusetts Institute of Technology, Cambridge, 2003.
 31. Born, M.; Wolf, E., *Principle of Optics*. 7th ed.; Cambridge University Press: Cambridge, 1999.
 32. Deng, T.; Chen, C. T.; Honeker, C.; Thomas, E. L. "Two-dimensional block copolymer photonic crystals" *Polymer* **2003**, 44, 6549-6553.
 33. Yablonovitch, E.; Gmitter, T. J. "Photonic Band Structure: The Face-Centered-Cubic case" *Physical Reivew Letters* **1989**, 63, 1950.

34. Sozuer, H. S.; Haus, J. W.; Inguva, R. "Photonic Bands - Convergence Problems with the Plane-Wave Method" *Physical Review B* **1992**, 45, 13962-13972.
35. Chan, C. T.; Ho, K. M.; Soukoulis, C. M. "Photonic Band-Gaps in Experimentally Realizable Periodic Dielectric Structures" *Europhysics Letters* **1991**, 16, 563-568.
36. Urbas, A. M.; Maldovan, M.; DeRege, P.; Thomas, E. L. "Bicontinuous cubic block copolymer photonic crystals" *Advanced Materials* **2002**, 14, 1850-1853.
37. Maldovan, M.; Urbas, A. M.; Yufa, N.; Carter, W. C.; Thomas, E. L. "Photonic properties of bicontinuous cubic microphases" *Physical Review B* **2002**, 65, 165123.
38. Bockstaller, M.; Kolb, R.; Thomas, E. L. "Metallodielectric photonic crystals based on diblock copolymers" *Advanced Materials* **2001**, 13, 1783-1786.
39. Bockstaller, M. R.; Lapetnikov, Y.; Margel, S.; Thomas, E. L. "Size-selective organization of enthalpic compatibilized nanocrystals in ternary block copolymer/particle mixtures" *Journal of the American Chemical Society* **2003**, 125, 5276-5277.
40. Bockstaller, M. R.; Thomas, E. L. "Proximity effects in self-organized binary particle-block copolymer blends" *Physical Review Letters* **2004**, 93, 166106.
41. Huh, J.; Ginzburg, V. V.; Balazs, A. C. "Thermodynamic behavior of particle/diblock copolymer mixtures: Simulation and theory" *Macromolecules* **2000**, 33, 8085-8096.
42. Thompson, R. B.; Ginzburg, V. V.; Matsen, M. W.; Balazs, A. C. "Predicting the mesophases of copolymer-nanoparticle composites" *Science* **2001**, 292, 2469-2472.
43. Chiu, J. J.; Kim, B. J.; Kramer, E. J.; Pine, D. J. "Control of nanoparticle location in

- block copolymers" *Journal of the American Chemical Society* **2005**, 127, 5036-5037.
44. Bockstaller, M. R.; Mickiewicz, R. A.; Thomas, E. L. "Block Copolymer Nanocomposites: Perspectives for Tailored Functional Materials" *Advanced Materials* **2005**, 17, 1331.
45. Osuji, C.; Chao, C. Y.; Bitá, I.; Ober, C. K.; Thomas, E. L. "Temperature-dependent photonic bandgap in a self-assembled hydrogen-bonded liquid-crystalline diblock copolymer" *Advanced Functional Materials* **2002**, 12, 753-758.
46. Valkama, S.; Kosonen, H.; Ruokolainen, J.; Haatainen, T.; Torkkeli, M.; Serimaa, R.; Ten Brinke, G.; Ikkala, O. "Self-assembled polymeric solid films with temperature-induced large and reversible photonic-bandgap switching" *Nature Materials* **2004**, 3, 872-876.

Chapter 2.

Materials and Experimental Methods

In this chapter, information on materials and experimental methods used in this research are provided. Synthetic procedures and molecular characterizations of ultrahigh molecular weight poly(styrene-*b*-isoprene) (PS-*b*-PI) block copolymers are presented in the first section. The second section summarizes experimental techniques for microstructural characterization of the block copolymers such as ultrasmall angle X-ray scattering (USAXS), transmission electron microscopy (TEM), and laser scanning confocal microscopy (LSCM). Finally, various spectroscopic techniques for optical characterization of photonic block copolymers, organic laser dyes, and devices using these materials are described.

2.1. High Molecular Weight Block Copolymers

High molecular weight lamellar-forming PS-*b*-PI diblock copolymers are the main materials used in this thesis and were prepared via living anionic polymerization technique by sequential addition of monomers. Dr. Wonmok Lee made an equal contribution in preparing the lamellar block copolymer samples. Dr. Peter DeRege provided the cylinder-forming PS-*b*-PI block copolymer sample for directional solidification and confocal microscopy study (in Chapter 6).

Since its discovery by Szwarc in 1956¹, *living* anionic polymerization has been extensively used for the synthesis of model polymer systems with well-controlled molecular weight, molecular weight distribution, composition, and chain architectures. While a high vacuum technique² has been the most widely used method for living anionic polymerization due to its excellent control of impurities such as oxygen and water, some disadvantages such as time-consuming and laborious glass-blowing, and difficulty to accurately measure the quantity of monomer for desired molecular weight and composition have made researchers implement an alternative approach using an inert atmosphere technique.³ In the case of the inert atmosphere technique, a slight overpressure of N₂ or Ar is used to maintain a dry and oxygen-free condition, and the preparation and the actual polymerization run are relatively easier and faster than the high vacuum technique with comparable control of molecular weight and molecular weight distribution. In this thesis, a modified version of the inert atmosphere technique was employed to synthesize high molecular weight (500-1000 kg/mol) lamellar-forming PS-*b*-PI diblock copolymers using a

glove box (Innovative Technology) equipped with catalyst system for removing organic vapor, oxygen (O₂) and moisture (H₂O). All of these impurities can interfere with the polymerization reaction to terminate the living anions and thus must be minimized in order to achieve well-controlled molecular weight and molecular weight distribution. The proper control of impurities is especially crucial for the synthesis of ultrahigh molecular weight samples where the amount of initiator is extremely small. In the following sections we summarize the experimental procedures for the synthesis of ultrahigh molecular weight block copolymers including glassware preparation, purification of monomers/solvents, polymerization reaction by sequential addition, and molecular characterization for determining molecular weight and composition. More thorough and extensive information about living anionic polymerization techniques can be obtained from the literature.^{2,3}

2.1.1. Purification of glassware, syringes, and needles

All pre-cleaned glassware such as flasks and distillation adapters was repeatedly rinsed with deionized water, tetrahydrofuran (THF), and isopropanol. The rinsed and dried glassware was then baked in a furnace (Thermolyne 30400 in Prof. Yoel Fink's group at MIT) at 500 °C for 2-3 hours to relax residual stresses. This annealing process was followed by additional baking at 570 °C for 2 hours to remove any remaining organic contaminants on the surface. Before purification or polymerization steps, the baked glassware was connected to a vacuum manifold and thoroughly flame-baked under vacuum to minimize any residual water adsorbed to the glass surface. Gastight syringes and metal needles were also cleaned and baked before use.

2.1.2. Purification of solvents

A mixture of benzene and cyclohexane (4:1, v/v) was used as solvent for polymerization. Benzene (Aldrich, 99+%) was stirred over concentrated sulfuric acid (100mL/L) for a week to remove impurities such as thiophenes and substituted phenyl compounds followed by a repeated wash with an aqueous solution of NaOH (or NaHCO₃) and deionized water. After the neutralization step, benzene was dried with finely grounded CaH₂ for 24 h and filtered. Cyclohexane (anhydrous, 99.5%) was stirred over CaH₂ for 24 h and filtered. The mixture of benzene and cyclohexane (4:1, v/v) was then transferred to the purification flask and degassed by one or two freeze-pump-thaw cycles. Before vacuum distillation, it was once more purified with *n*-butyllithium (*n*-BuLi, Aldrich: 1.6M in hexane, 5 mL per 1L of solvent) and styrene (Aldrich 99%, 4 mL per 1L of solvent) until the orange color of the living polystyryl anions persisted, which indicates the purity of the solvent mixture. The vacuum distilled solvent was then isolated and stored in the N₂ atmosphere inside the glove box.

2.1.3. Purification of monomers

Styrene (Aldrich, 99%) was first dried over CaH₂ for 24 h and is degassed and vacuum distilled. The dried styrene monomer was then purified with dibutyl magnesium (DBM, Aldrich: 1.0 M in heptane, [styrene]:[DBM solution] = 20:1) for 4 ~ 5 hours at room temperature before vacuum distillation until a persistent bright yellow-green color was observed. Isoprene (Aldrich, 99%) was also dried over CaH₂ (Aldrich, 90-95%) for 24 h and was degassed and vacuum distilled. It was then purified with *n*-BuLi at 0 °C for 1~ 2

h. It is very important to maintain the temperature of the purifying solution of isoprene and *n*-BuLi at or below 0 °C to avoid a runaway polymerization. The vacuum distilled monomers were then isolated and stored under vacuum in the N₂ atmosphere inside the glove box refrigerator maintained at -30 °C.

2.1.4. Polymerization and molecular characterization

Reactor purification and polymerization steps were conducted under N₂ atmosphere inside the glove box. A round bottom flask (1000 mL) with a Teflon stir bar was washed with *sec*-BuLi (Aldrich: 1.3M in cyclohexane) to remove any remaining impurities and rinsed two or three times with the purified mixed solvent. The purified mixed solvent (benzene: cyclohexane = 4:1, v/v) and styrene monomer were then transferred into the reactor using a gastight syringe filled with activated basic alumina (For activation, alumina was baked at 500 °C for 24 h and slowly cooled.). An initiator solution was prepared by diluting *sec*-BuLi (Aldrich: 1.3M in cyclohexane) to ~ 0.02 mM with the mixed solvent. The active initiator concentration was determined using the Gilman double titration method.⁴ When the temperature of the reactor was stabilized at 40 °C, polymerization was initiated by adding the initiator solution through the gas tight syringe and the solution developed a bright yellow color. After 6 h with stirring, the isoprene was then added through the gas tight syringe with activated alumina and the pale green color of isopropylolithium anions developed. The solution was stirred for additional 48 h before termination. The reaction was terminated with 1.0 mL of deoxygenated methanol. The polymer was precipitated and washed with methanol containing 2,6-di-*tert*-butyl-4-

methylphenol (BHT, 0.1 wt% to methanol) as an antioxidant and dried under vacuum at room temperature.

The molecular weights (M_n and M_w) and polydispersity indices (M_w/M_n) have been determined by a Hewlett-Packard Series 1100 size exclusion chromatograph (SEC). THF was eluted from the SEC columns (3 PLgel 5 μ m) at 1.0 mL/min. The molecular weights (M_n and M_w) were obtained relative to a polystyrene calibration curve. The compositions of the block copolymers were determined by nuclear magnetic resonance (^1H NMR, 300 MHz) using CDCl_3 as a solvent based on the ratio of integrated intensities of aromatic protons to vinylic protons.⁵ Volume fractions were then calculated based on known densities of PS (1.04 g/cm³) and PI (0.913 g/cm³).⁶ Table 2.1 summarizes the sample information of the block copolymers used in this thesis.

Sample ID.	Total M_n (PS-b-PI) (g/mol)	M_n (PS) (g/mol)	M_n (PI) (g/mol)	PDI	PS wt %	PS vol %
LY0423	840,000	480,000	360,000	1.08	57	54
LY0421	650,000	360,000	290,000	1.09	55	52
LY0401	590,000	320,000	270,000	1.09	54	51
PDR 091	1,100,000	240,000	860,000	1.05	22	20

Table 2.1: Molecular characteristics of the four photonic PS-b-PI block copolymers used in this thesis.

2.2. Microstructural Characterization

2.2.1. Solution casting

The first step for microstructural characterization of high molecular weight block copolymers is to form dry films by a solution casting process. Solutions of block copolymer samples in toluene were made at a concentration of ~ 50 mg/mL at room temperature. In order to protect samples from degradation in solution, the antioxidant (BHT) was added to the solution at a concentration of 0.1 wt % relative to the solvent. Sample solutions were covered by aluminum foil to prevent UV exposure from room light during the stirring or the solvent evaporation process. Stirring was minimized and conducted at a very low speed to avoid mechanical degradation. After a complete solubilization of polymers, the solution was transferred into a crucible (VWR, 10 mm diameter) for the evaporation of solvent. To obtain a thermodynamically near-equilibrium morphology and to minimize defect formation during the solution casting process, a very slow evaporation condition was applied, in which the evaporation of a solvent was carried out in a solvent-saturated atmosphere with a gentle flux of air, requiring two to four weeks for sample drying. After the first evaporation step, samples were further dried in vacuum at room temperature for 24 h to remove any residual solvent. Subsequently, thermally annealing was conducted at 120 °C under vacuum for 3-5 days, producing films with a final thickness of ~ 0.1 -0.3 mm.

2.2.2. Cryomicrotomy, staining, and transmission electron microscopy (TEM)

Ultrathin sections (50-100 nm thickness) from annealed block copolymer samples

were obtained by cryomicrotomy using a Reichert-Jung Ultracut FC4E at -90 °C (for knife) and at -100 °C (for specimen). Carbon was thermal-evaporated onto the microtomed thin sections mounted on copper grids with carbon thicknesses of ~ 100 Å to enhance sample's electrical and thermal conductivity, and to provide beam damage protection in TEM. The samples were then stained in a vapor of OsO₄ for 2-3 h to improve mass thickness contrast, which preferentially binds to the PI block containing double bonds. TEM micrographs were obtained using JEOL 200CX and JEOL 2000FX transmission electron microscopes operating at 120-200 kV.

2.2.3. Laser scanning confocal microscopy (LSCM)

The directionally solidified PS-*b*-PI samples (in chapter 6) were analyzed by reflection-mode LSCM (Leica TCS SPII, located in the laboratory of Prof. Timothy Swager of MIT) using a 488 nm probe laser beam without further sample treatment. Since the PS-*b*-PI block copolymer does not contain any fluorophore, the light signal results from reflection off the PS-PI interface. Signals of the probe light were scanned for every LSCM image through an oil-immersion objective lens (Leica, HCX PL APO 63X/1.40-0.60).

2.2.4. Ultrasmall angle X-ray scattering (USAXS)

Since the periodicities of the photonic block copolymers are too large for conventional small angle X-ray scattering (SAXS), we employed ultrasmall angle X-ray scattering (USAXS) to obtain microstructural information. USAXS measurements of cast and annealed block copolymer films have been conducted at beamline X10A at Brookhaven

National Laboratory with 8 keV radiation (wavelength $\lambda = 0.1548$ nm). A Bonse-Hart camera setup⁷ was employed with single bounce Ge-111 monochromator and analyzer crystals. The slit collimated incident beam intensity was about 5×10^9 cts/s and the beam size was 0.6×0.8 mm² (V-H). Data were collected by a scintillation detector (Bicron) which was swept through an arc to collect a linear data set of intensity versus angular position. All data were acquired at room temperature and used without additional corrections.

2.3. Optical Characterization

2.3.1. Reflectivity measurement

The experimental reflectivity spectrum was measured using a microscope spectrometer, which is composed of an optical microscope (Zeiss Axioskop), a portable spectrometer (Stellarnet Inc. EPP2000) equipped with a charge-coupled-device (CCD) detector and a holographic grating, and a tungsten halogen lamp as the illumination source. Reflected light from the sample on the specimen stage is collected by an objective lens (Carl Zeiss, Neo-Fluora 10X, N.A. = 0.3) and focused to an optical fiber through a custom-made fiber-optic-adaptor having a collection lens ($f=1.2$), which is connected to the spectrometer. By adjusting an aperture between a light source and an objective lens, the probed sample area could be effectively adjusted. Due to the numerical aperture of the objective lens (N.A. = 0.3), the reflectivity spectrum is not from purely normal incidence

light but represents a convolution of multiple reflectivity spectra over the incidence angles of 0° to $\sim 17.5^\circ$.

The procedures for measuring a reflectivity spectrum using this equipment are summarized as follows: First, the tungsten lamp was turned on at ~ 12 V and warmed up for 10 min. A silver coated metallic mirror was placed under the objective lens and the light was focused onto its surface. This reflectivity spectrum was saved as 100 % reference. Then the incident light was blocked by closing the light path in the microscope and the corresponding spectrum was saved as 0% reference. After completion of the normalization steps, sample spectra were taken. Each spectrum was typically obtained with an integration time of 500-1000 ms and averaged with 5-20 measurements.

2.3.2. Absorption and emission measurements

The photophysical properties of organic laser dyes are sensitively affected by matrix materials when they are incorporated as dopants. The absorption and emission spectra of a gain medium studied in this thesis were measured from thin solid films of a dye-doped polymer. Organic laser dyes (DCM or Bis-MSB from Exciton) and polymethylmethacrylate (PMMA from Aldrich, M_w : 15000 g/mol) were dissolved in a solvent (spectroscopic grade) such as toluene or THF, in which the dye concentration to the polymer matrix was 0.1-0.5 wt %. The dye-polymer solution (~ 10 wt %) was then simple-cast onto a glass slide to make a smooth film (thickness ~ 100 μm). The absorption spectrum was obtained on a Hewlett-Packard 8453 diode array UV-VIS spectrophotometer using a bare glass slide as a blank reference. The emission spectrum was measured either by a SPEX Fluorolog- $\tau 2$

spectrofluorometer (model FL112, 450 W xenon lamp) or by a laboratory setup of a pump laser and a fiber-optic spectrometer, which was also used for measuring optically pumped lasing as described in the following section.

2.3.3. Lasing measurements

Frequency-doubled or tripled Q-switched Nd:YAG pulse lasers (Continuum NY 61, $\lambda = 532$ nm, pulse width = 5 ns, repetition rate = 50 Hz in the laboratory of Prof. Mounji Bawendi of MIT; Continuum NY 60B, $\lambda = 532$ nm/355 nm, pulse width = 10 ns, repetition rate = 20 Hz) were used as pump light source. The pump laser beam was focused onto the sample with a lens of 20 cm focal length and 5 cm diameter at an incidence angle of $30^\circ \sim 40^\circ$ (from the normal), giving a beam diameter at the sample of about 300 μm as schematically shown in Figure 2.1. Lasing occurred in both the forward and backward directions and the backward emitted light was collected and focused onto a fiber-optic spectrometer (Ocean Optics USB 2000 or HR 2000). The average power of the excitation pulses was controlled with a neutral density (ND) filter or by adjusting the input voltage of the pump laser power supply.

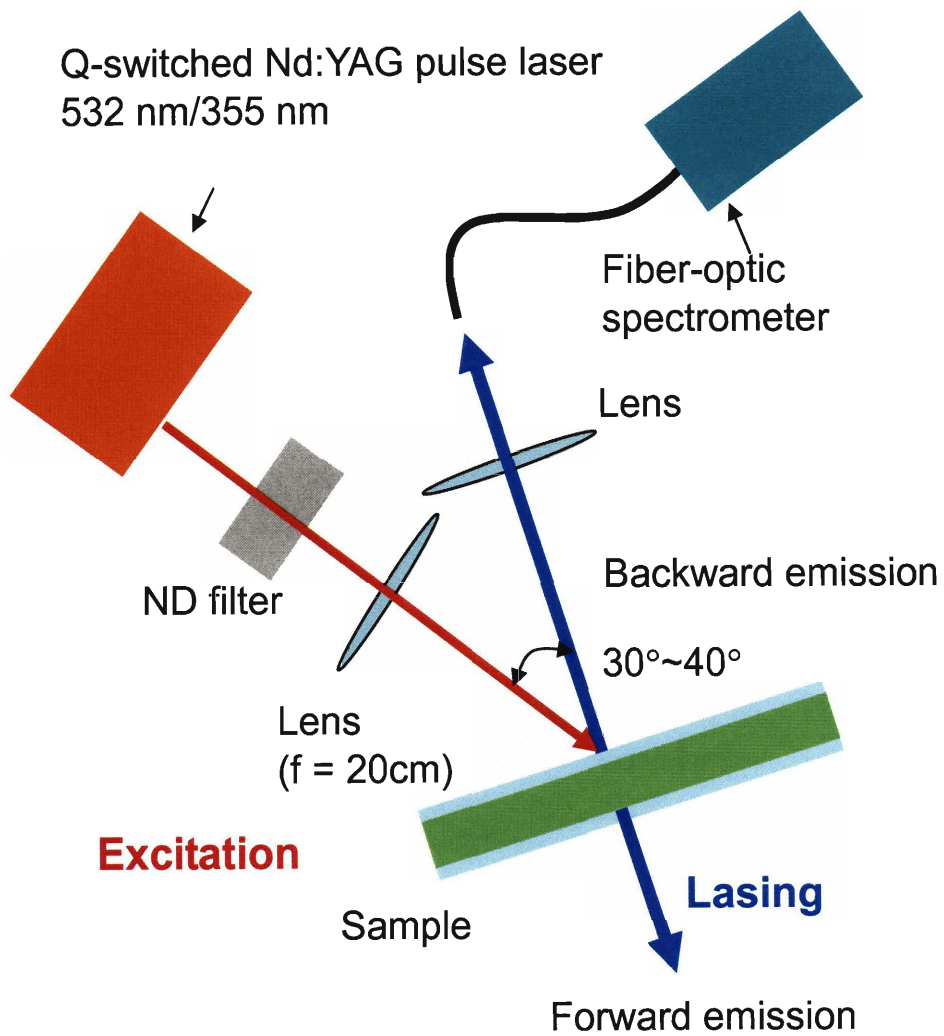


Figure 2.1: A schematic of the experimental setup for measuring emission and lasing spectra.

2.4. References

1. Szwarc, M. "Living polymers" *Nature* **1956**, 178, 1168.
2. Hadjichristidis, N.; Iatrou, H.; Pispas, S.; Pitsikalis, M. "Anionic polymerization: High vacuum techniques" *Journal of Polymer Science Part A-Polymer Chemistry* **2000**, 38, 3211-3234.
3. Ndoni, S.; Papadakis, C. M.; Bates, F. S.; Almdal, K. "Laboratory-Scale Setup For Anionic-Polymerization Under Inert Atmosphere" *Review of Scientific Instruments* **1995**, 66, 1090-1095.
4. Gilman, H.; Haubein, A. H. "The quantitative analysis of alkyllithium compounds" *Journal of the American Chemical Society* **1944**, 66, 1515.
5. Pham, Q. T.; Petiaud, R.; Waton, H., *Proton and Carbon NMR spectra of Polymers*. Wiley: New York, 2003.
6. Brandrup, J.; Immergut, E. H.; Grulke, E. A., *Polymer Handbook*. 4 ed.; Wiley-Interscience: 1999.
7. Bonse, U.; Hart, M. "Small angle X-ray scattering by spherical particles of polystyrene and polyvinyltoluene" *Zeitschrift fur Physik* **1966**, 189, 151.

Chapter 3.

Defect-Mode Mirror-less Lasing in a Dye-doped Organic/Inorganic Hybrid 1D Photonic Crystal

In this chapter we present the results from our investigation of defect-mode photonic band gap lasing with an organic/inorganic hybrid 1D photonic crystal containing a dye-doped defect layer. This defect-mode laser structure has been studied as a “model” system from which a basic understanding of the main factors affecting optically pumped lasing with dye-doped photonic crystals has been developed. The multilayer laser structure consists of alternating layers of titania (TiO_2) nanoparticles and polymethylmethacrylate (PMMA) with an active emission layer of an organic dye dispersed in PMMA. Low threshold lasing has been demonstrated at a single defect-mode wavelength of the 1D photonic bandgap structure resulting from the inhibited density of states of photons and the enhanced rates of spontaneous emission at the localized resonant defect mode within the photonic stop band.

The work on synthesis of titania nanoparticles and fabrication of multilayer structures was a collaboration with Dr. Wonmok Lee and the lasing measurements were assisted by Dr. Jean-Michel Caruge and Dr. Steven Kooi. Parts of this chapter were featured in: J. Yoon, W. Lee, J-M. Caruge, S. Kooi, M. Bawendi, E. L. Thomas *Applied Physics Letters* **2006**, 88, 0912021-0921023.

3.1. Introduction

Among the many unique properties of photonic crystals, control of spontaneous emission by means of modification of the photon density of states has been of special interest since the performance of various optoelectronic devices such as lasers,¹ light emitting diodes,² or solar cells³ is often limited by spontaneous emission. It has been shown theoretically^{4,5} as well as experimentally^{6,7} that when the transition frequency of the gain material confined within a photonic crystal is matched with the frequency range of the photonic bandgap, the spontaneous emission is rigorously inhibited by the low density of states in the gap. As the depletion of the excited state by spontaneous emission within the gap is decreased, spontaneous emission is enhanced at the band edges or at defect modes purposefully introduced into the bandgap. This can lead to low-threshold or even threshold-less lasing. In this regard, there have been considerable efforts to fabricate photonic bandgap laser devices either as distributed feedback lasing^{8,9} operating at band-edge frequencies or as defect-mode lasing^{10,11} operating at localized defect-mode frequencies within the gap. In particular, due to the relative simplicity of fabrication, 1D photonic crystal laser devices have been extensively studied.^{10,12-16} For example, Kopp et al. demonstrated photonic band-edge lasing from a 1D photonic crystal of dye-doped cholesteric liquid crystal.¹² More recently, Ozaki et al. showed electrically tunable defect-mode lasing in a 1D photonic crystal of alternating TiO₂/SiO₂ multilayers using a conducting polymer as a gain medium and a nematic liquid crystal as an electrically tunable defect layer.¹⁰ In the present study, a novel organic/inorganic hybrid 1D photonic crystal

with organic laser dyes as a gain medium has been developed to demonstrate low threshold defect-mode lasing.

3.2. Results and Discussion

We employed inorganic titania (TiO_2) nanoparticles and polymethylmethacrylate (PMMA) as high and low index dielectric materials for constructing a distributed Bragg reflector (DBR) having a 1D photonic bandgap. TiO_2 nanoparticles were prepared following the synthetic scheme reported by Sanchez et al.¹⁷. The nanocrystalline TiO_2 particles were composed of the *anatase* phase (experimental refractive index ~ 1.78 at 500 nm) with an average diameter of 4 nm as characterized by X-ray diffraction (XRD) (Rigaku High Resolution 250 mm Diffractometer), spectroscopic ellipsometry (M2000, J. A. Woollam Co., Inc) and transmission electron microscopy (TEM) (JEOL 2000FX, 200kV). Figure 3.1 and 3.2 show a bright field TEM micrograph and a powder X-ray diffractogram of the TiO_2 nanoparticles, respectively. Due to the organic surface capping group of acetylacetonone (AcAc), the TiO_2 particles were readily dissolved in a polar organic solvent such as butanol. The nanoparticles formed a thin film with excellent optical transparency, with a surface roughness in the order of a few nanometers. PMMA (Aldrich, M_w : 15,000 g/mole) was used as received and dissolved in toluene. As a defect layer containing a gain medium, the laser dye, 4-(dicyanomethylene)-2-methyl-6-(4-dimethylaminostyryl)-4H-pyran (DCM, Exciton), was dissolved in toluene at a concentration of 0.5 wt % with respect

to PMMA matrix. In order to fabricate the defect-mode 1D PBG laser structure, solutions of TiO_2 (in butanol), PMMA (in toluene) and DCM/PMMA (in toluene) were sequentially spin-coated.

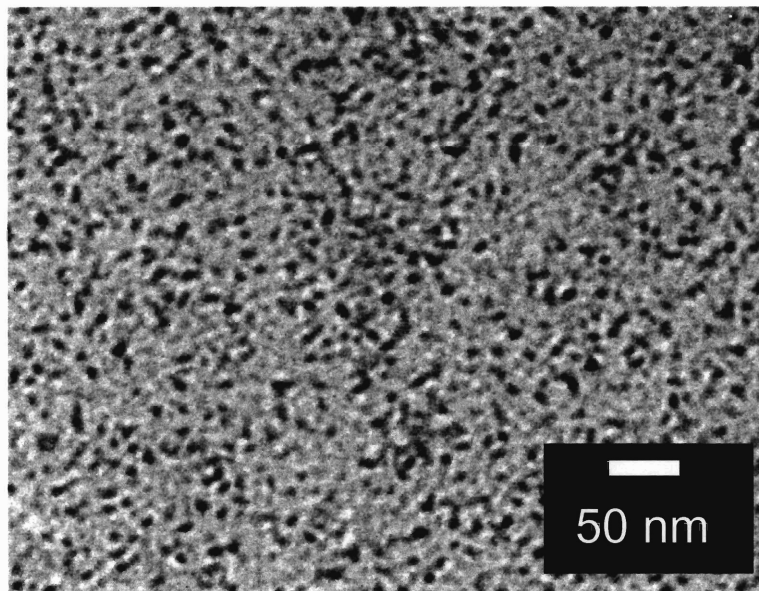


Figure 3.1: Bright-field TEM micrograph of surface-protected titania (TiO_2) nanoparticles on carbon film, in which well-dispersed and monodisperse nanoparticles having an average diameter of about 4 nm are evident.

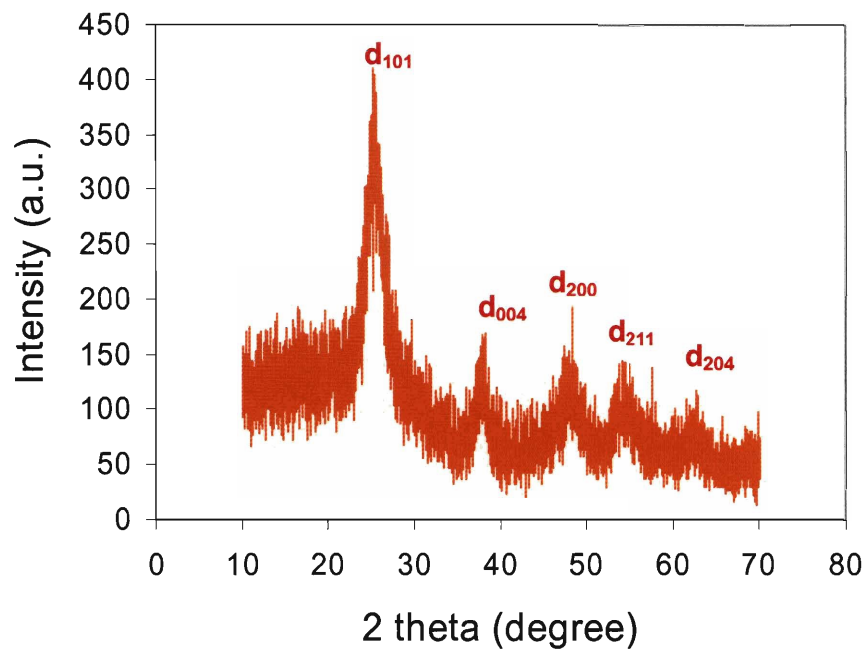


Figure 3.2: Powder XRD spectrum of surface-protected titania (TiO₂) nanoparticles, in which the reflection peaks are well matched with those of *anatase* phase titania.

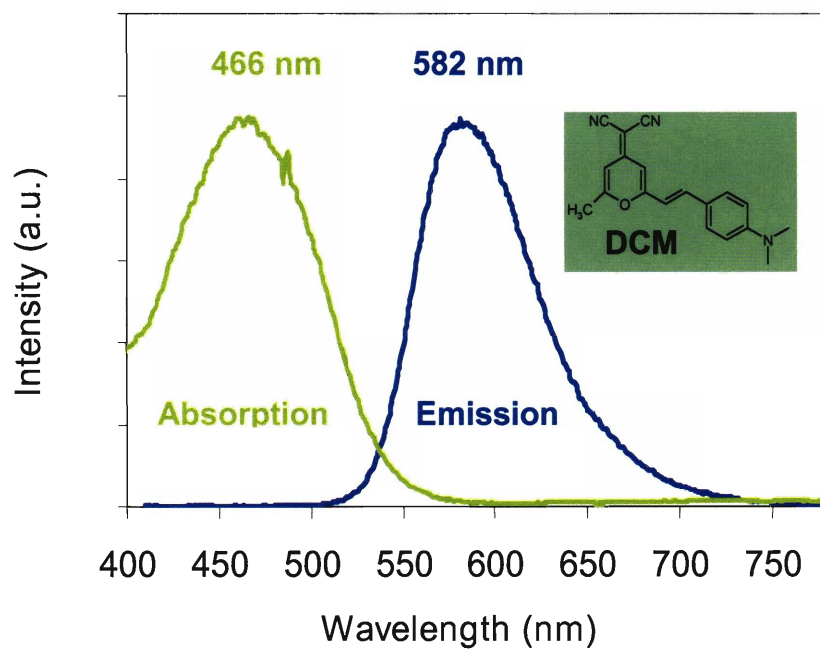


Figure 3.3: Linear absorption and photoluminescence spectra of DCM (0.5 wt %, 400 nm excitation) in PMMA. The molecular structure of DCM is shown in the inset. The FWHM of the PL spectrum is about 75 nm and the peak of the spontaneous emission occurs at 582 nm.

We designed the defect-mode laser structure built around the photophysical properties of the gain medium. The absorption spectrum was obtained on a Hewlett-Packard 8453 diode array spectrophotometer while the emission spectrum (excitation at 400 nm) was measured by a SPEX Fluorolog- $\tau 2$ spectrofluorometer. Figure 3.3 shows the linear absorption and emission spectra of the thin film of DCM (0.5 wt %) in PMMA. The peak wavelengths of absorption and emission are around 466 nm and 582 nm, respectively. The defect-mode PBG structure fabricated by a sequential spin-coating process, glass-(PMMA-TiO₂)¹⁵-(DCM/PMMA)-(TiO₂-PMMA)¹⁵-air, consists of 61 alternating layers of TiO₂, PMMA, and a central defect layer containing DCM in PMMA as schematically shown in Figure 3.4. The average refractive indices of TiO₂, PMMA, and DCM in PMMA over the visible wavelength regime (400-700 nm) were individually measured by spectroscopic ellipsometry. The thicknesses of the corresponding layers were then determined from the calculation of reflectance spectra using the transfer matrix method (TMM)¹⁸, such that defect mode of the 1-D photonic crystal was located at the peak wavelength of the gain medium emission in order to optimize the lasing probability.

The number of defect modes and their locations can be readily controlled by changing either the thickness or the refractive index of the defect layer. Figure 3.5 shows the calculated reflectivity spectrum of the defect-mode 1-D photonic crystal at normal incidence, in which the arrows indicate the defect-modes inside the stop band. The high frequency defect-mode is purposefully located at 582 nm, coincident with the peak wavelength of emission of the DCM dye in the PMMA. Figure 3.6 is the corresponding photon density of states, which is normalized with respect to the density of states in vacuum.

The experimental reflectivity spectrum in Figure 3.7 was measured using an optical microscope (Zeiss Axioscop) equipped with a fiber-optic spectrometer (Stellarnet EPP2000) with a silver-coated metallic mirror as a 100% reference. Due to the numerical aperture of the objective lens (Mag. = 10X, N.A. =0.3), the spectrum in Figure 3.7 is not a pure normal incidence reflectance but represents a convolution of multiple reflectance spectra over the incidence angles of 0° to $\sim 17.5^\circ$.

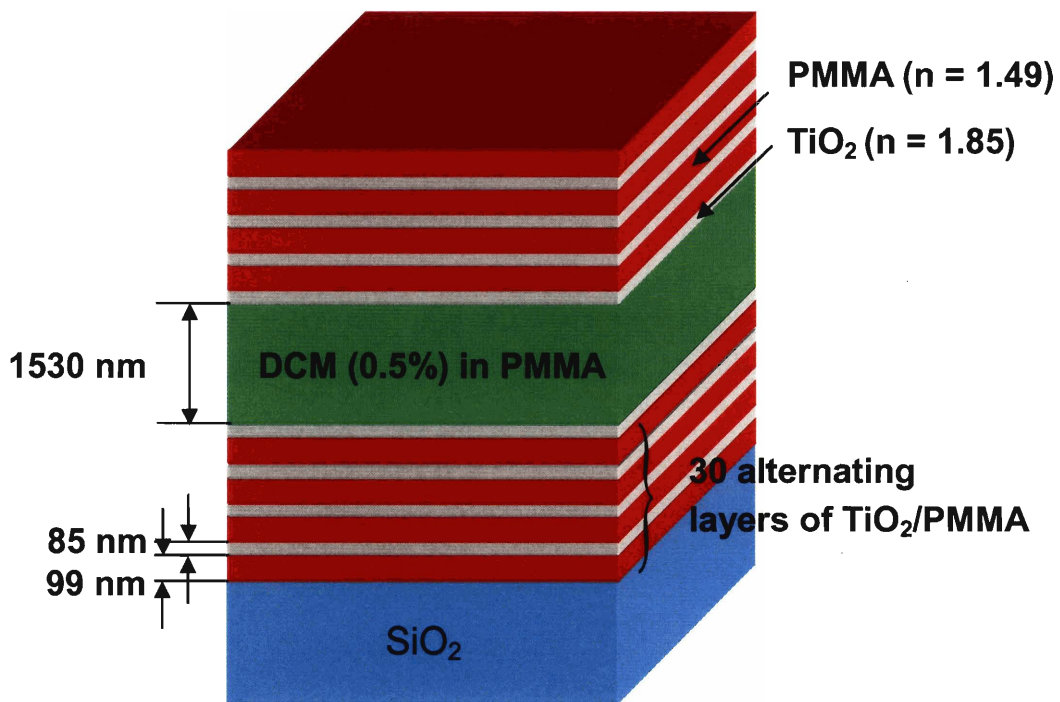


Figure 3.4: Schematic of dye-doped defect-mode 1D photonic crystal, glass-(PMMA- TiO_2)¹⁵-(DCM/PMMA)-(TiO₂-PMMA)¹⁵-air.

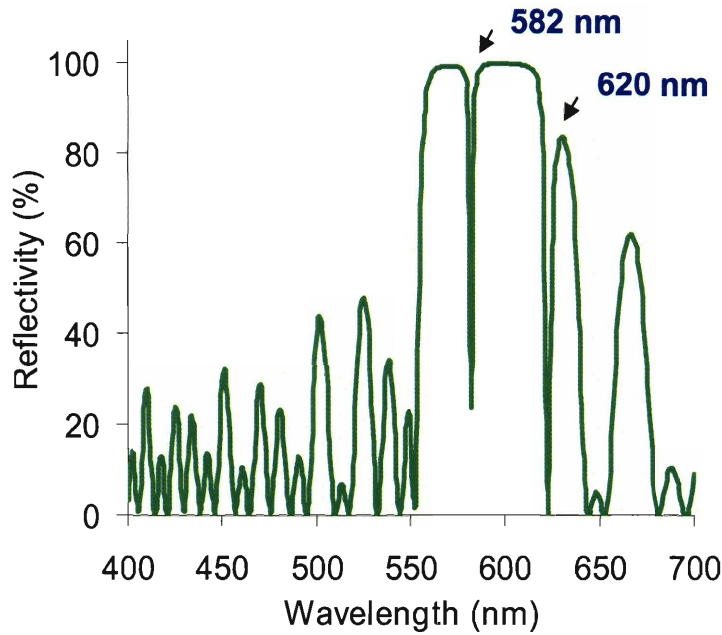


Figure 3.5: TMM calculated reflectivity spectrum of the defect-mode 1D photonic crystal, glass-(PMMA-TiO₂)¹⁵-(DCM/PMMA)-(TiO₂-PMMA)¹⁵-air, at normal incidence. Arrows indicate the localized defect-modes created by the PMMA defect layer.

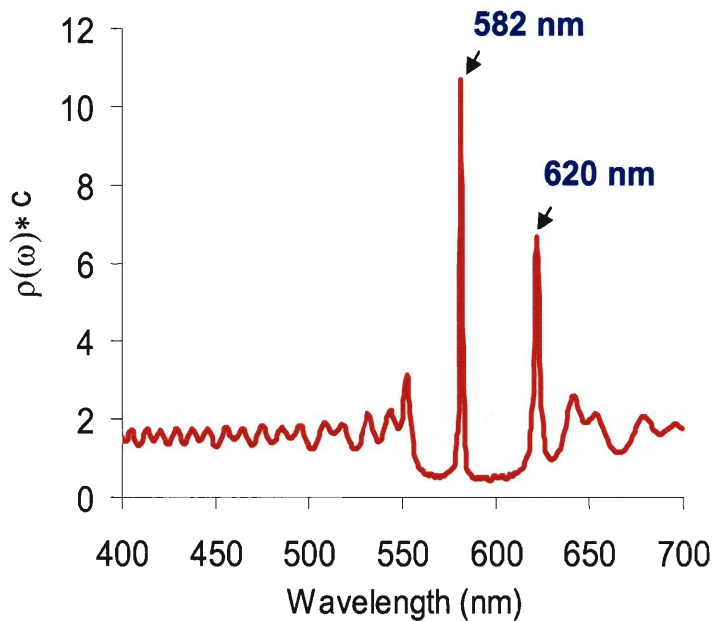


Figure 3.6: Calculated density of states of photons, $\rho(\omega) \equiv dk/d\omega$, of the defect-mode 1D photonic crystal, glass-(PMMA-TiO₂)¹⁵-(DCM/PMMA)-(TiO₂-PMMA)¹⁵-air, in which the y-axis shows the normalized $\rho(\omega)$ with respect to the value in vacuum ($\rho(\omega)_{vac} = 1/c$).

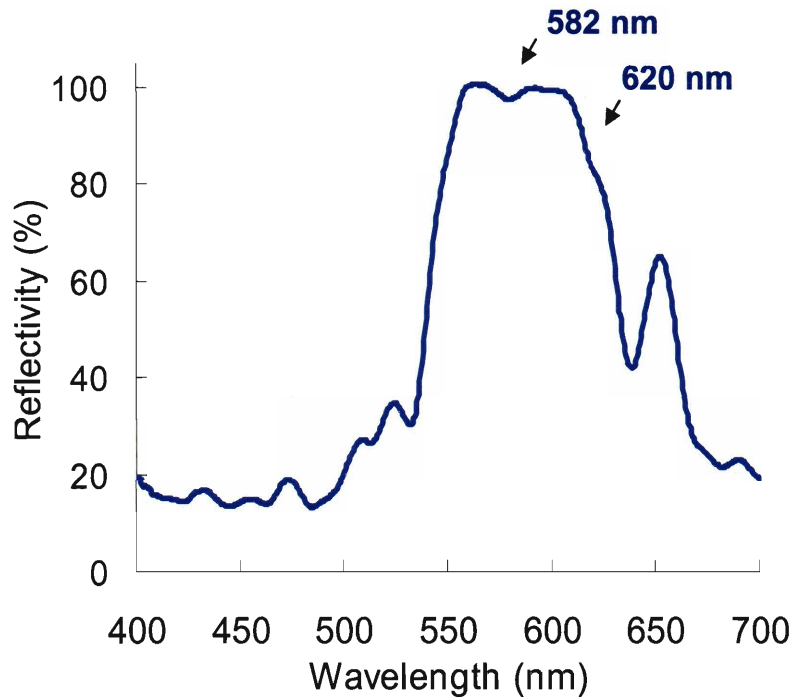


Figure 3.7: Measured reflectivity spectrum of the fabricated defect-mode 1D photonic crystal at near normal incidence using a reflection-mode optical microscope connected to a fiber-optic spectrometer, in which the spectrum represents a convolution of multiple reflectivity spectra over the incidence angles of 0° to $\sim 17.5^\circ$ due to the numerical aperture of the objective lens (10X, N.A. = 0.3). Experimental features indicative of the two defect modes are shown.

The lasing experiment was performed at room temperature with the setup shown in Figure 2.1 (in Chapter 2). The defect mode laser structure was optically pumped with frequency-doubled pulses of a Q-switched Nd:YAG laser (Continuum NY 61, $\lambda = 532$ nm, pulse width = 5 ns, repetition rate = 50 Hz). The pump laser beam was focused onto the sample with a lens of 20 cm focal length and 5 cm diameter with an incidence angle of 40° (from the normal), giving a beam diameter at the sample of about $300 \mu\text{m}$. Lasing occurred in both the forward and backward directions and the backward emitted light was collected

and focused onto a fiber-optic spectrometer (Ocean Optics USB 2000). The average power of the excitation pulses was controlled with a neutral density (ND) filter.

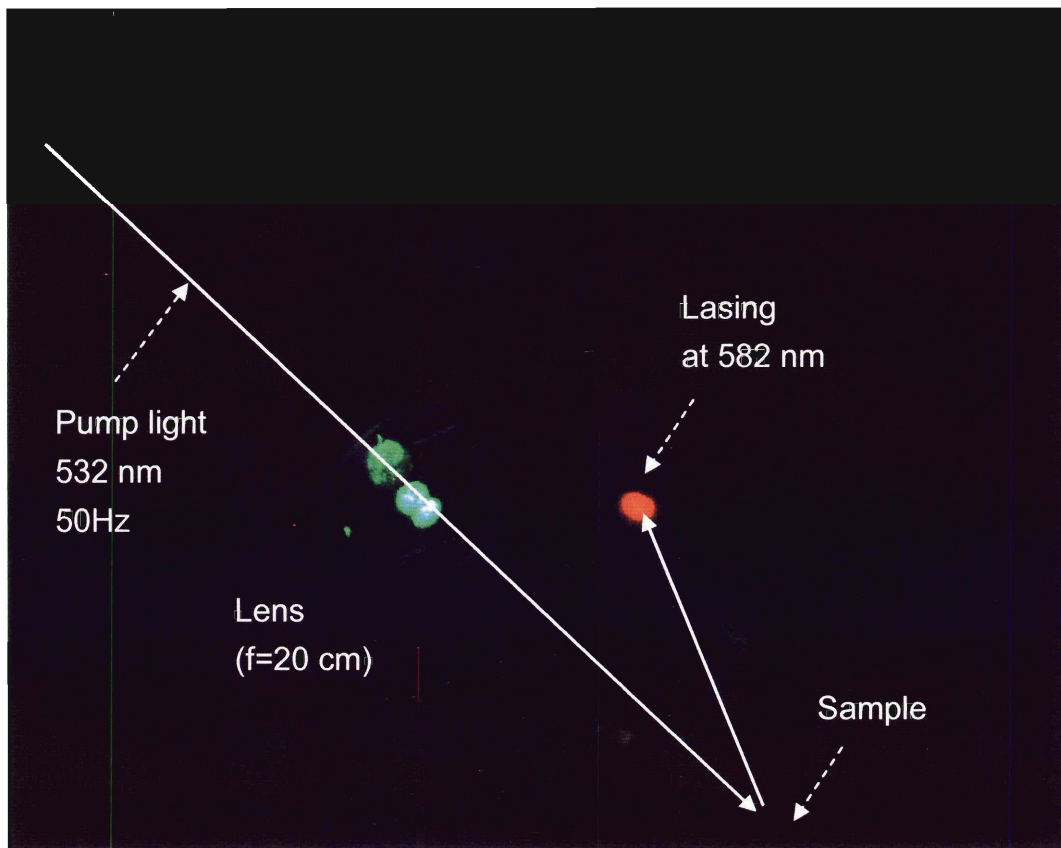


Figure 3.8: Photograph of the 582 nm lasing from the defect-mode 1-D photonic crystal. A highly directional lasing in the backward direction was observed on a white background.

Figure 3.8 shows a photograph of the red lasing beam on a white background, in which a highly directional emission parallel to the surface normal of the sample clearly indicates the lasing action as the pump power was increased above a lasing threshold. The corresponding

emission spectrum is shown in Figure 3.9, where strong single-mode lasing was observed at the expected defect-mode wavelength of 582 nm. The two small peaks in addition to the lasing line correspond to the excitation beam (532 nm) and the spontaneous emission at the lower frequency defect mode (at ~ 620 nm, and for the pump power, the emission is below the lasing threshold). In order to confirm lasing, the usual pump power dependence of the emission intensity at the 582 nm lasing wavelength was obtained as shown in Figure 3.10 (red data points). In our experimental conditions, the lasing threshold was measured to be ~ 17 mJ/cm² (12 μ J/pulse on the area of 300 μ m diameter). The expected spectral narrowing of the emission above the lasing threshold was also observed. The FWHM of the emission line at the lasing wavelength decreased from 2.1 nm to 1.0 nm as shown in Figure 3.11 (blue data points), which is limited by the spectral resolution of our experimental setup. The small FWHM (2.1 nm) before the lasing threshold in Figure 3.11 is due to the narrow width of the defect mode within the bandgap. The spectral narrowing above the lasing threshold is more significant if the FWHM of the lasing is compared with the FWHM of the spontaneous emission from a medium without any periodic structure, which is about 75 nm as shown in Figure 3.3.

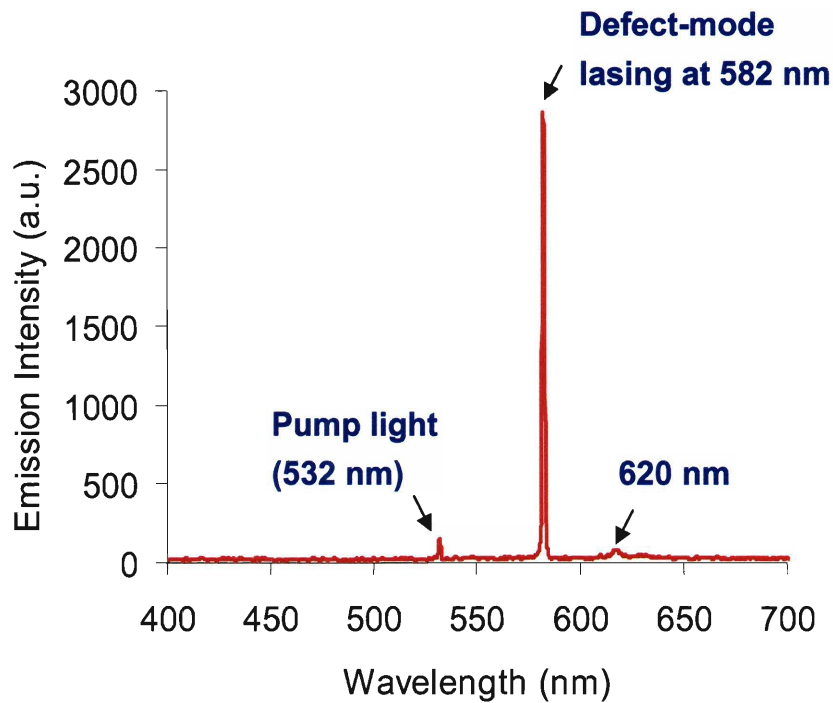


Figure 3.9: The lasing spectrum obtained at a pump power of 1 mW, above the lasing threshold. The two small peaks beside the lasing line at 582 nm correspond to the excitation light (532 nm) and to the low frequency defect mode (at 620 nm, below its lasing threshold for this pump power).

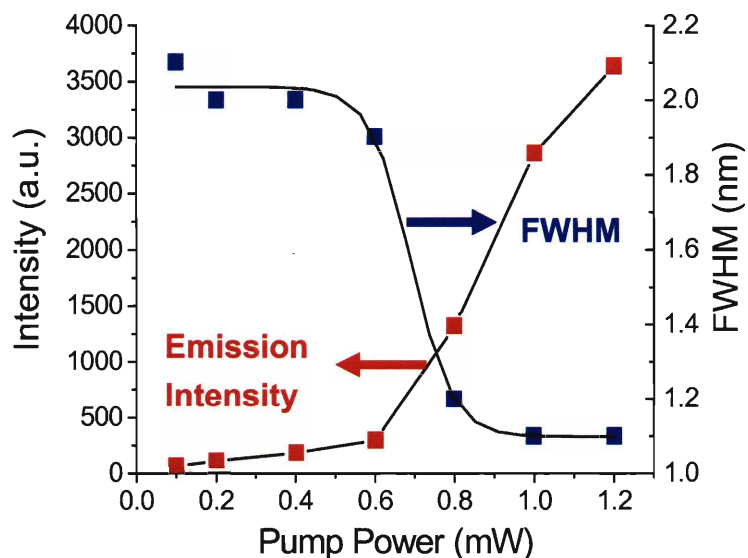


Figure 3.10: Emission intensity and line-width (the full width at half maximum, FWHM) at the lasing wavelength (582 nm) as a function of pump power. The behavior of the intensity and the FWHM clearly demonstrate a threshold for lasing around 0.6 mW pump power (12 μ J pulse energy).

The defect-mode low threshold lasing action results from the modification of the density of states and the enhanced spontaneous emission due to the placement of the gain medium within a 1-D PBG structure. According to Fermi's golden rule, the rate of spontaneous emission at a frequency ω is proportional to the density of states at that frequency, $\rho(\omega)$.¹⁹ Therefore if the gain medium is within a photonic bandgap structure, the spontaneous emission rate at a particular wavelength can be enhanced or suppressed by a factor proportional to $\rho(\omega)$. We analytically calculated via the TMM the density of states for the defect-mode finite 1-D photonic bandgap structure shown in Figure 3.4. A normalized plot of $\rho(\omega)$ with respect to the density of states in vacuum ($1/c$, c : speed of light in vacuum) is displayed in Figure 3.6.²⁰ The density of states has very low values within the photonic bandgap, except at the localized defect modes, where the rate of spontaneous emission is enhanced by a large factor. As the gain for the localized defect modes is greatly increased with the increased spontaneous emission rate, low threshold lasing can be accomplished if the gain threshold is reached.

3.3 Conclusion

In summary, we have designed and fabricated a novel organic/inorganic hybrid 1-D photonic crystal containing a dye doped defect layer and demonstrated low threshold defect-mode lasing. TiO_2 nanoparticles and PMMA were employed as high and low index materials with the organic laser dye, DCM, as the gain medium. Low threshold lasing was

induced at a localized defect-mode wavelength resulting from the suppressed density of states of photons within the photonic bandgap and the enhanced rates of spontaneous emission at the localized resonant defect mode.

3.4. References

1. Siegman, A. E., *Lasers*. University Science Books: Palo Alto, 1986.
2. Boroditsky, M.; Krauss, T. F.; Coccioli, R.; Vrijen, R.; Bhat, R.; Yablonovitch, E. "Light extraction from optically pumped light-emitting diode by thin-slab photonic crystals" *Applied Physics Letters* **1999**, *75*, 1036-1038.
3. Gratzel, M. "Photoelectrochemical cells" *Nature* **2001**, *414*, 338-344.
4. John, S.; Quang, T. "Spontaneous emission near the edge of a photonic band-gap" *Physical Review A* **1994**, *50*, 1764-1769.
5. Dowling, J. P.; Bowden, C. M. "Atomic emission rates in inhomogeneous-media with applications to photonic band structures" *Physical Review A* **1992**, *46*, 612-622.
6. Lodahl, P.; van Driel, A. F.; Nikolaev, I. S.; Irman, A.; Overgaag, K.; Vanmaekelbergh, D. L.; Vos, W. L. "Controlling the dynamics of spontaneous emission from quantum dots by photonic crystals" *Nature* **2004**, *430*, 654-657.
7. Fujita, M.; Takahashi, S.; Tanaka, Y.; Asano, T.; Noda, S. "Simultaneous inhibition and redistribution of spontaneous light emission in photonic crystals" *Science* **2005**, *308*, 1296-1298.
8. Meier, M.; Mekis, A.; Dodabalapur, A.; Timko, A.; Slusher, R. E.; Joannopoulos, J. D.; Nalamasu, O. "Laser action from two-dimensional distributed feedback in photonic crystals" *Applied Physics Letters* **1999**, *74*, 7-9.
9. Mekis, A.; Meier, M.; Dodabalapur, A.; Slusher, R. E.; Joannopoulos, J. D. "Lasing

- mechanism in two-dimensional photonic crystal lasers" *Applied Physics A-Materials Science & Processing* **1999**, 69, 111-114.
10. Ozaki, R.; Matsuhisa, Y.; Ozaki, M.; Yoshino, K. "Electrically tunable lasing based on defect mode in one-dimensional photonic crystal with conducting polymer and liquid crystal defect layer" *Applied Physics Letters* **2004**, 84, 1844-1846.
 11. Painter, O.; Lee, R. K.; Scherer, A.; Yariv, A.; O'Brien, J. D.; Dapkus, P. D.; Kim, I. "Two-dimensional photonic band-gap defect mode laser" *Science* **1999**, 284, 1819-1821.
 12. Kopp, V. I.; Fan, B.; Vithana, H. K. M.; Genack, A. Z. "Low-threshold lasing at the edge of a photonic stop band in cholesteric liquid crystals" *Optics Letters* **1998**, 23, 1707-1709.
 13. Ozaki, R.; Matsui, T.; Ozaki, M.; Yoshino, K. "Electrically color-tunable defect mode lasing in one-dimensional photonic-band-gap system containing liquid crystal" *Applied Physics Letters* **2003**, 82, 3593-3595.
 14. Jakubiak, R.; Bunning, T. J.; Vaia, R. A.; Natarajan, L. V.; Tondiglia, V. P. "Electrically switchable, one-dimensional polymeric resonators from holographic photopolymerization: A new approach for active photonic bandgap materials" *Advanced Materials* **2003**, 15, 241-244.
 15. Schmidtke, J.; Stille, W.; Finkelmann, H. "Defect mode emission of a dye doped cholesteric polymer network" *Physical Review Letters* **2003**, 90.
 16. Finkelmann, H.; Kim, S. T.; Munoz, A.; Palffy-Muhoray, P.; Taheri, B. "Tunable mirrorless lasing in cholesteric liquid crystalline elastomers" *Advanced Materials*

- 2001, 13, 1069-1072.
17. Scolan, E.; Sanchez, C. "Synthesis and characterization of surface-protected nanocrystalline titania particles" *Chemistry of Materials* **1998**, 10, 3217-3223.
 18. Born, M.; Wolf, E., *Principles of Optics, 7th edition*. Cambridge University Press: Cambridge, 1999.
 19. Yokoyama, H.; Ujihara, K., *Spontaneous emission and laser oscillation in microcavities*. CRC Press: Boca Raton, 1995.
 20. Bendickson, J. M.; Dowling, J. P.; Scalora, M. "Analytic expressions for the electromagnetic mode density in finite, one-dimensional, photonic band-gap structures" *Physical Review E* **1996**, 53, 4107-4121.

Chapter 4.

Optically Pumped Surface-Emitting Lasing using Self-Assembled Distributed Bragg Reflectors from 1D Block Copolymer Photonic Crystal

In this chapter, we demonstrate a thin film organic laser cavity using a block copolymer based one-dimensional (1D) photonic crystal. Polymeric distributed Bragg reflectors (DBRs) were prepared through the self-assembly of a lamellar poly(styrene-*b*-isoprene) (PS-*b*-PI) diblock copolymer having a 1D photonic stop band overlapping with the fluorescence spectrum of a gain medium. Optically pumped surface-emitting lasing was obtained using polymethylmethacrylate (PMMA) doped with 1,4-di-(2-methylstyryl)benzene (Bis-MSB) as an organic gain medium and the polymeric self-assembled DBR as a spectral-band selective feedback element.

Dr. Wonmok Lee contributed to this work in the synthesis of high molecular weight block copolymers. Parts of this chapter will appear in: J. Yoon, W. Lee, E. L. Thomas *Nano Letters* (submitted)

4.1. Introduction

Over the past years, block copolymers have been considered as a unique materials platform for fabricating large-area well-ordered photonic bandgap structures.¹ Block copolymers microphase separate into periodic microdomains on the length scale of the blocks driven by a competition between a tendency to reduce the interfacial free energy and to increase the conformational entropy of the constituting polymer chains.^{2, 3} With an appropriate microdomain size (d_i) that is large enough to interact with visible light ($d_i \sim \lambda/4n_i$, n_i is the refractive index of the respective microdomain, λ is wavelength of light in vacuum), block copolymers can create periodic dielectric structures having a photonic stop band in the optical frequency range. Various block copolymer systems, such as lamellar, cylindrical, and double gyroid diblock copolymers,⁴⁻⁷ blends of diblock copolymer with homopolymers or plasticizers,^{8, 9} and block copolymer nanocomposites doped with inorganic nanoparticles, or liquid crystals,¹⁰⁻¹² were successfully used to prepare 1D, 2D, and 3D visible wavelength photonic crystals (see the more detailed review in Chapter 1).

While the basic concept of self-assembled block copolymer based photonic bandgap materials as *passive* photonic structures has been well demonstrated, little work has been done in terms of realizing *active* photonic devices using these materials. Though the performance of block copolymer based photonic structures is somewhat limited by the relatively low dielectric contrast and intrinsic defect formation during self-assembly, these materials could be employed where precision performance is not required since they offer many advantages such as a range of easily accessible periodic structures, light weight,

mechanical flexibility and low cost processing over a large area. One potential application of such self-assembled polymeric photonic crystals is to use them as a resonator in a photonic microcavity to provide spectrally-selective feedback for lasing.¹³⁻¹⁵ Here we illustrate that thin films of a high molecular weight lamellar-forming poly(styrene-*b*-isoprene) (PS-*b*-PI) block copolymer, can be utilized to produce self-assembled distributed Bragg reflectors which can act as a narrow spectral-band selective element for defining a photonic microcavity. Optically pumped surface-emitting lasing has been demonstrated with fluorescent organic laser dyes in a polymer matrix as a gain medium deposited between block copolymer based Bragg reflectors.

4.2. Results and Discussion

The high molecular weight photonic PS-*b*-PI block copolymer was synthesized via anionic polymerization with sequential addition of styrene and isoprene monomer in cyclohexane/benzene mixed solvent.¹⁶ The molecular weight and composition of the block copolymer are 5.90×10^5 g/mol (PDI: 1.09), 54/46 (PS/PI, wt/wt) as measured by gel permeation chromatography (GPC) and nuclear magnetic resonance (NMR) analysis. Figure 4.1 shows a bright field transmission electron microscopy (TEM) micrograph from the cryomicrotomed sample of the PS-*b*-PI block copolymer exhibiting the 1D periodic lamellar morphology, in which the dark regions correspond to the PI domains preferentially stained with osmium tetroxide (OsO_4) and the bright regions correspond to the PS domains.

The domain periodicity from the TEM micrograph is approximately 140 nm (PS: 76 nm, PI: 64 nm).

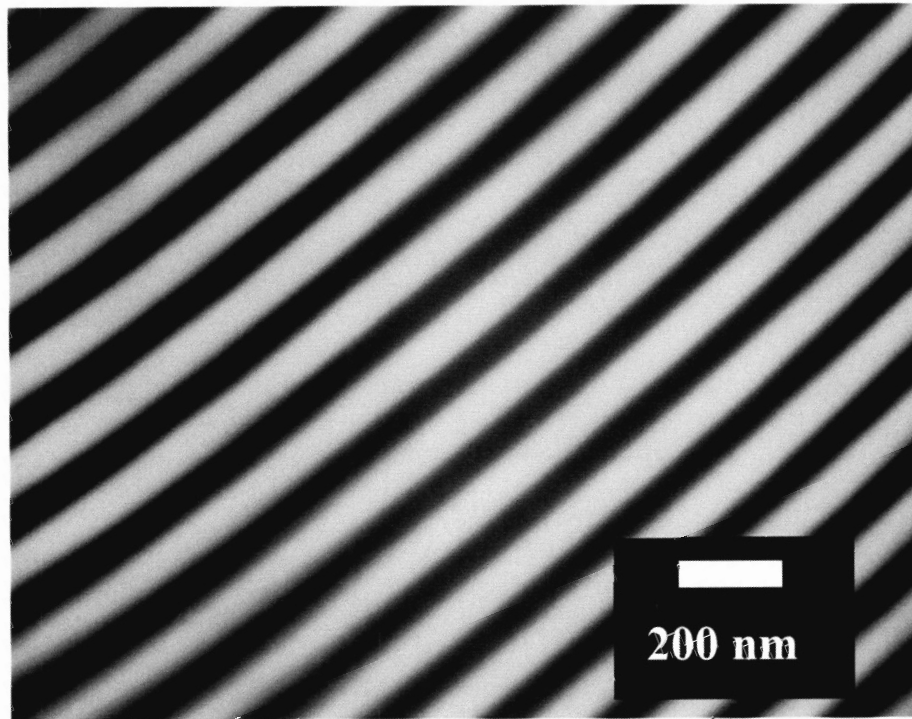


Figure 4.1: Bright-field TEM micrograph of cryomicrotomed PS-b-PI block copolymer showing a 1D periodic lamellar morphology, in which the dark regions correspond to PI domains preferentially stained with OsO_4 and the bright regions correspond to PS domains. The domain periodicity is approximately 140 nm (PS: 76 nm, PI: 64 nm).

The resulting 1D periodic dielectric structure selectively reflects light of a range of frequencies due to a constructive interference at the set of interfaces between high (PS, $n = 1.59$) and low (PI, $n = 1.51$) refractive index domains. Figure 4.2 shows the experimentally measured reflectivity spectrum of the self-assembled distributed Bragg reflector at near normal incidence of light, in which the peak reflectivity occurs at 410 nm and the width of the stop band (the full width of half maximum: FWHM) is about 14 nm.

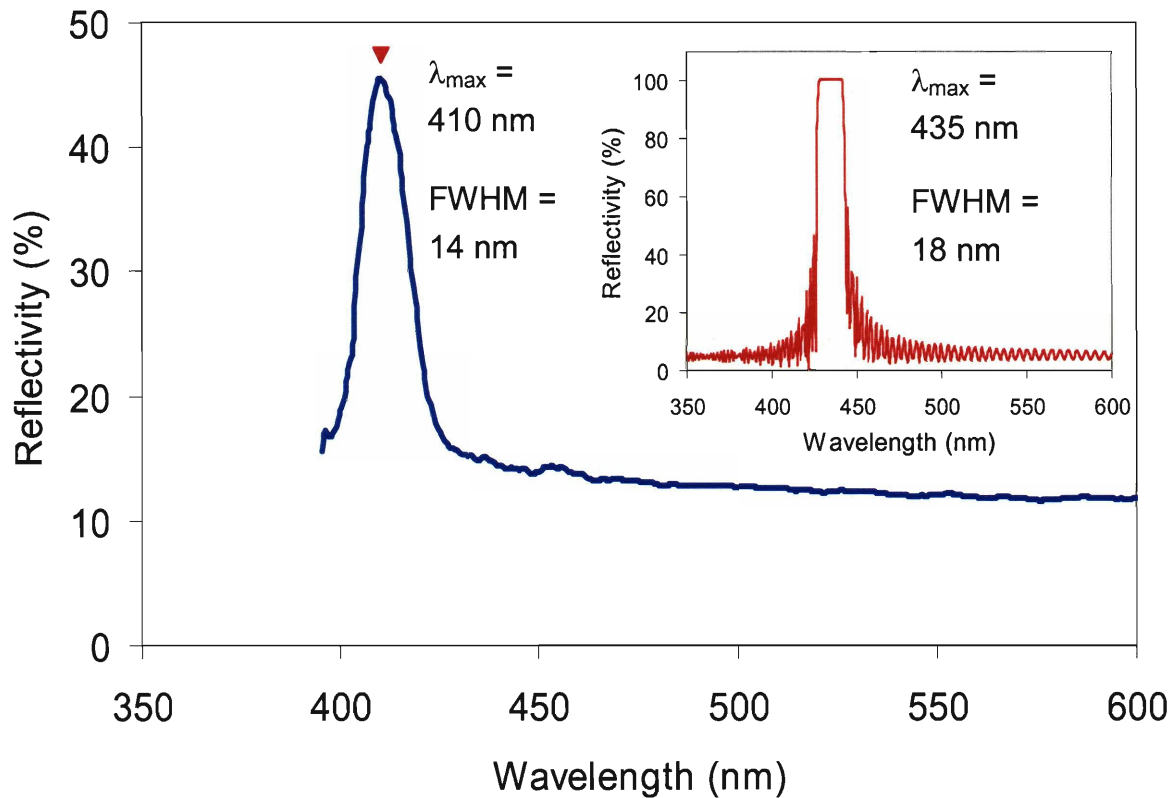


Figure 4.2: Experimental reflectivity spectrum of the fabricated block copolymer based distributed Bragg reflector at near normal incidence using a reflection-mode optical microscope connected to a fiber-optic spectrometer. The inset shows a calculated reflectivity spectrum using the transfer matrix method at a normal incidence for a finite 1D periodic structure, assuming 300 layers of PS (76 nm, $n = 1.59$) and PI domains (64 nm, $n = 1.51$).

This reflectivity spectrum was obtained using an optical microscope (Zeiss Axioscop) equipped with a fiber-optic spectrometer (Stellarnet EPP2000) using a silver-coated metallic mirror as a 100 % reference. Due to the numerical aperture of the objective lens (Carl Zeiss, Neo-Fluora 10X, N.A. = 0.3), the spectrum is not from a pure normal incidence reflectance but represents a convolution of multiple reflectance spectra over the incidence angles of 0° to $\sim 17.5^\circ$. The inset in Figure 4.2 shows a calculated reflectivity spectrum at a normal incidence of light by transfer matrix method¹⁷ for a finite 1D periodic structure assuming 300 layers of PS (76 nm, $n = 1.59$) and PI domains (64 nm, $n = 1.51$), for which the FWHM is 18 nm and the bandgap center is located at 435 nm. The relatively narrow experimental reflectivity band (FWHM ~ 14 nm) of the sample suggests that the effective dielectric contrast between PS and PI domains is reduced due to the effect of some retained solvent (cumene: $n \sim 1.49$). The narrow band-width also indicates that the parallel alignment of the lamellar microdomain orientation is quite good due to the influence of the substrate. Given the measured peak wavelength position (410 nm) and the width (FWHM: 14 nm) of the reflectivity band, we can estimate the solvent concentration approximately 10 wt % by assuming a parallel orientation of lamellae, a uniform distribution of solvent in PS and PI domains (i.e. neutral solvent), and a constant ratio of PS and PI domain thicknesses (i.e. $d_{PS}/d_{PI} = 76/64$ as obtained from TEM). The spectral response of this block copolymer based distributed Bragg reflector can be readily tuned by simply controlling the solvent concentration in the block copolymer solution, which can affect the spacings and the effective refractive indices of the respective microdomains (see the more detailed treatment of this solvatochromic effect in Chapter 5).

For the gain medium, an organic chromophore, (1,4-di-(2-methylstyryl)benzene (Bis-MSB, Exciton), was dissolved in PMMA at a concentration of 0.1 wt % (to PMMA) using tetrahydrofuran (THF) as the solvent. Figure 4.3 is the photoluminescence spectrum from a solid film (thickness ~ 1 mm) of Bis-MSB in PMMA cast on a glass substrate excited by a 355 nm pulse, in which the peak fluorescence occurs at 425 nm and the FWHM is 41 nm. The inset in Figure 4.3 shows the absorption spectrum from the same sample obtained on a Hewlett-Packard 8453 diode array spectrophotometer, where the absorption maximum is around 350 nm.

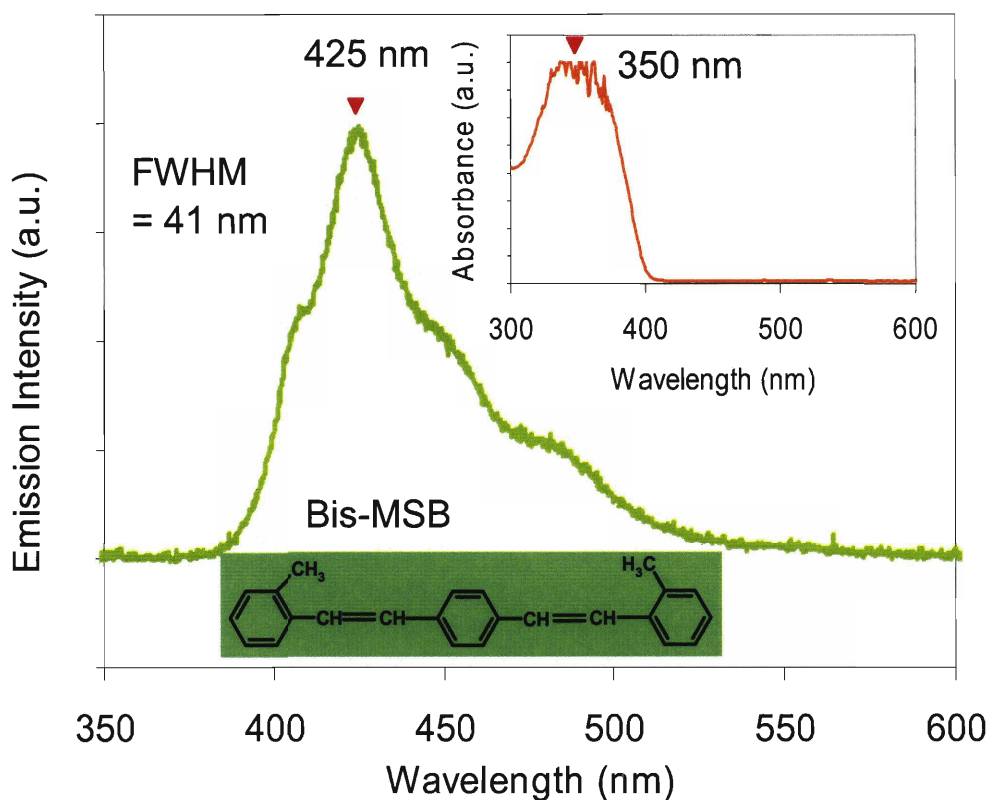


Figure 4.3: Photoluminescence (PL) spectrum from a solid film of Bis-MSB (0.1 wt %, 355 nm excitation) in PMMA. The FWHM of the PL spectrum is about 75 nm. The inset shows the absorption spectrum from the same sample, where the absorption maximum is located at around 350 nm.

A thin film organic laser cavity was fabricated by sandwiching the gain medium between two block copolymer based reflectors as schematically shown in Figure 4.4. First, the self-assembled reflectors were prepared from the solvent containing PS-b-PI cast between a microscope slide glass and a cover glass. After measuring the reflectivity data from the reflectors, the gain medium of PMMA/Bis-MSB in THF was then incorporated between the two reflectors with a thickness of about 300 μm using a spacer.

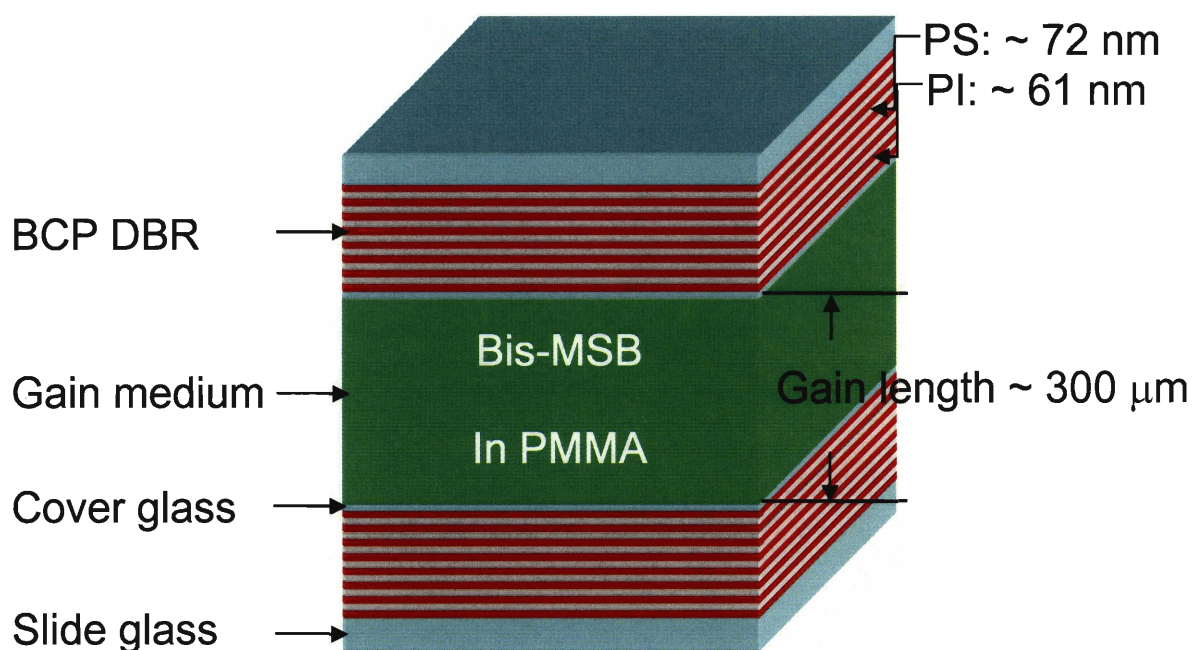


Figure 4.4: Schematic of the block copolymer based laser cavity, comprised of a gain medium, Bis-MSB and PMMA, enclosed between two block copolymer based distributed Bragg reflectors. The thicknesses of PS and PI domains are estimated values at 10 wt % solvent concentration based on the peak position and FWHM of the reflectivity spectrum.

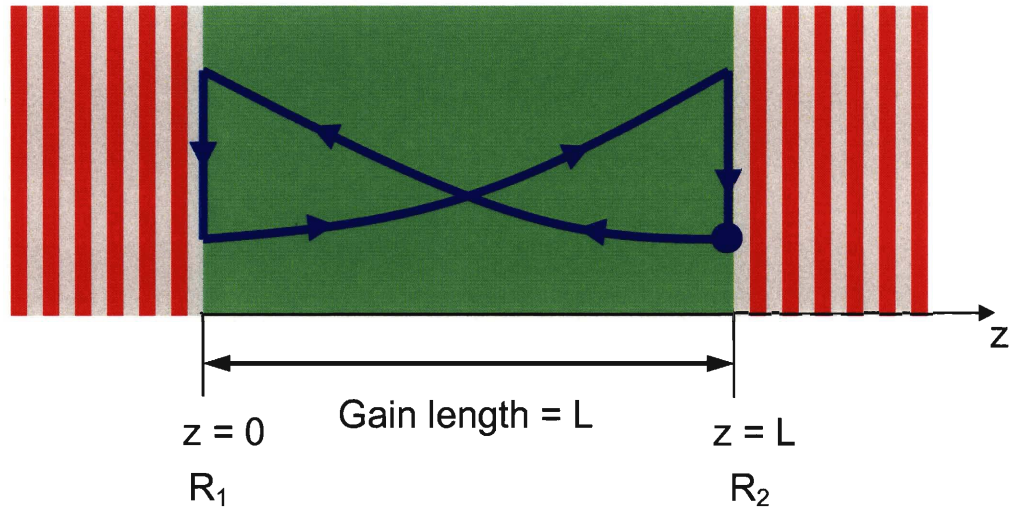


Figure 4.5: A model laser cavity composed of a gain medium (length L) and two dielectric mirrors having reflectivity values of R_1 ($z = 0$) and R_2 ($z = L$). The blue arrow represents the power of the oscillating radiation.

Figure 4.5 shows a model laser cavity composed of a gain medium of the length L enclosed between two dielectric mirrors having reflectivity values of R_1 (at $z = 0$) and R_2 (at $z = L$) for a simple cavity analysis. As the spontaneous emission from the gain medium oscillates between two mirrors along the axis of the cavity, there exist both amplification (due to the gain) and attenuation (due to the absorption and the loss at mirrors) in the intensity of the oscillating radiation. Therefore, the power of the oscillating radiation, $P(z)$, can be expressed as

$$P(z) = P(0)e^{Gz}e^{-\alpha z} \quad (4.1)$$

where $P(0)$ is the power of the radiation at $z = 0$, G is the gain coefficient of the gain

medium, α is the absorption coefficient of the gain medium. The steady-state oscillation condition then requires that the net gain must be the same as the net losses or the power of the radiation must be maintained constant on each round trip. Equation 4.2 shows a steady-state lasing condition for the cavity in Figure 4.5, where G_{th} is the threshold gain coefficient of the gain medium.¹⁸

$$e^{(G_{th}-\alpha)L} R_1 e^{(G_{th}-\alpha)L} R_2 = 1 \quad (4.2)$$

The approximate threshold gain coefficient for lasing (neglecting absorption, $\alpha = 0$) is then written in Equation 4.3.

$$G_{th} \approx \frac{1}{2L} \ln \left(\frac{1}{R_1 R_2} \right) \quad (4.3)$$

On the basis of above-described simple order-of-magnitude cavity analysis with the known gain length ($L = 300 \mu\text{m}$) and experimentally measured reflectivity of the block copolymer distributed Bragg reflector ($R_1 = R_2 \sim 0.48$), we can estimate the threshold gain coefficient required for lasing, which is about 24.5 cm^{-1} . Although the exact optical gain coefficient of the gain medium (Bis-MSB in PMMA) in our laser system was not measured in this study, this estimated threshold gain coefficient is in a reasonable range which can be achieved with typical organic dyes.^{19,20}

The experimental setup for the lasing experiment conducted at room temperature is shown in Figure 2.1 (see Chapter 2). A frequency-tripled output of a Q-switched Nd:YAG

laser (Continuum NY 60B, $\lambda = 335$ nm, pulse width = 10 ns, repetition rate = 20 Hz) was used as an excitation source. The pump laser beam was focused onto the sample with a 2.5 cm diameter lens of 20 cm focal length and at an incidence angle of 30° from the normal to the sample surface, giving a beam diameter at the sample of about $300 \mu\text{m}$. As the average power of the excitation pulse increases above the lasing threshold, a well-defined lasing beam was vertically emitted from the surface of the sample in both the forward and backward directions and the backward emitted light was collected using a fiber-optic spectrometer (Ocean Optics HR 2000). A set of neutral density filters were used to control the average power of the excitation pulses.

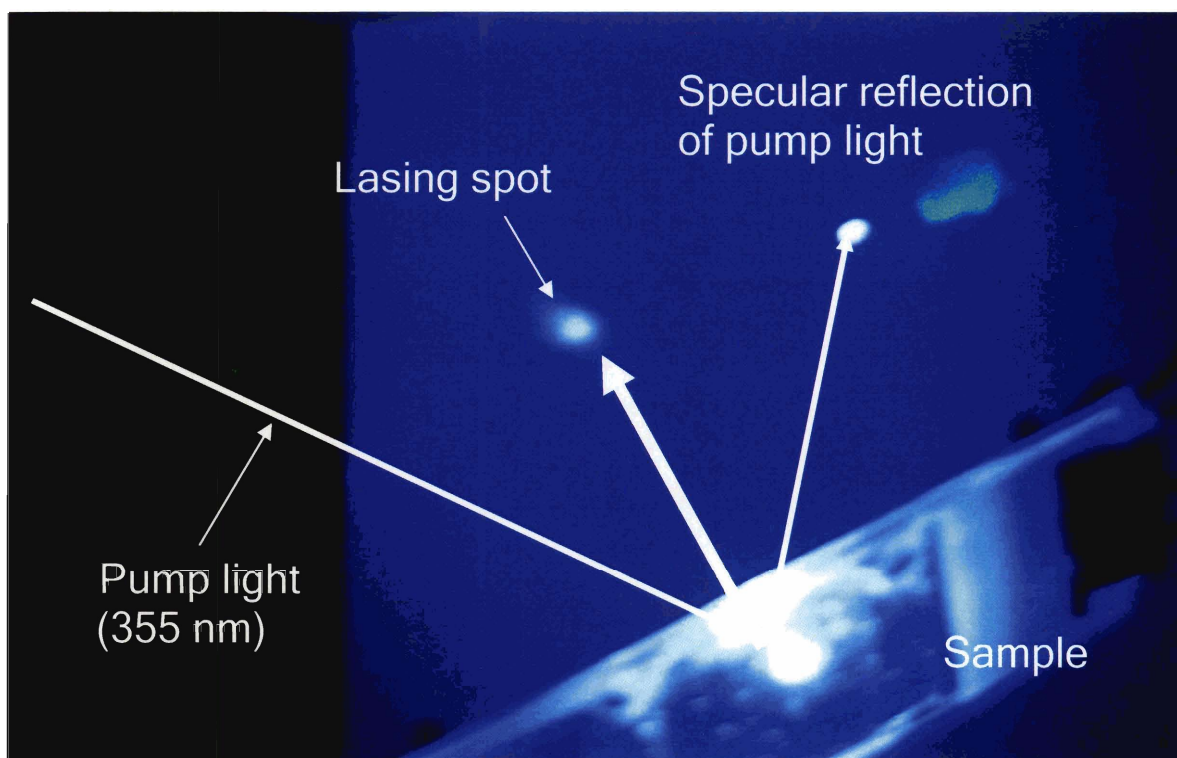


Figure 4.6: Photograph of the 410 nm lasing from the block copolymer based laser structure. A highly directional lasing output in the backward direction was observed on a white background.

Figure 4.6 shows a highly directional stimulated emission from the sample surface at a pump power greater than the lasing threshold, which is clear evidence for lasing. The corresponding emission spectra were recorded at various excitation pump powers as shown in Figure 4.7. Above the lasing threshold, sharp single-mode lasing occurs at around 410 nm with a significant spectral narrowing (FWHM \sim 1.0 nm). In order to further confirm lasing activity, the pump power dependence of the emission intensity at the lasing wavelength was obtained as shown in the inset of Figure. 4.7. Under the experimental conditions of this study, the lasing threshold was around 280 mJ/cm^2 (0.2 mJ/pulse on the area of $300 \text{ }\mu\text{m}$ diameter). Figure 4.8 shows a lasing spectrum with the same gain medium (Bis-MSB in PMMA) but obtained from a cavity sandwiched between an aluminum-coated mirror and a glass slide using the same pump configuration in Figure 2.1. In this arrangement the metallic mirror and the glass slide do not provide any spectrally-selective feedback. The lasing thus occurs at 425 nm where the dye emission is maximum (Figure 4.3) and the FWHM is 4 nm. This result further confirms that the narrow spectral selectivity of the lasing output obtained from the block copolymer laser cavity results from the selective feedback of block copolymer based distributed Bragg reflectors.

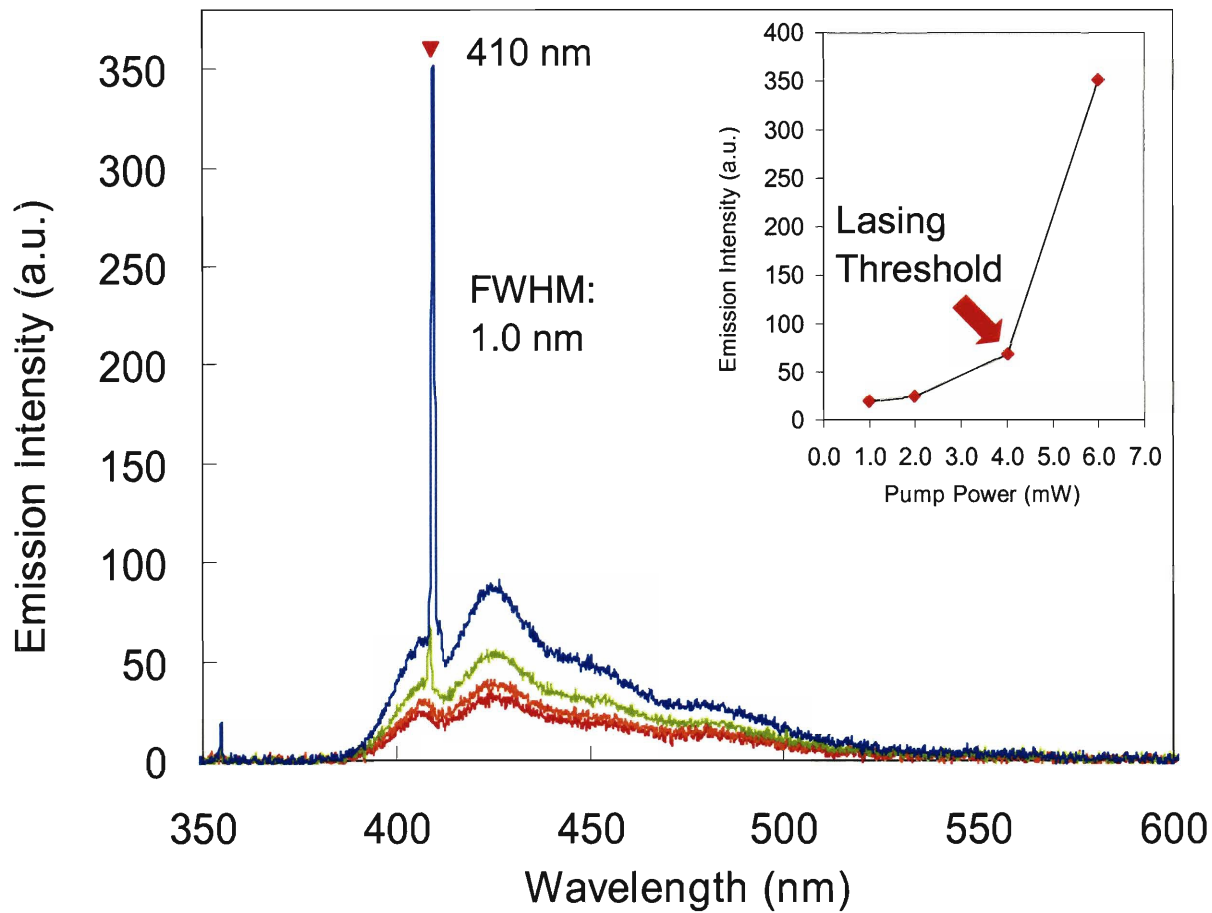


Figure 4.7: The emission spectra obtained at various pump powers. The FWHM of the lasing peak is 1 nm. Inset shows the emission intensity at the lasing wavelength (410 nm) as a function of pump power, which clearly shows a threshold for lasing at around 4 mW pump power (0.2 mJ pulse energy).

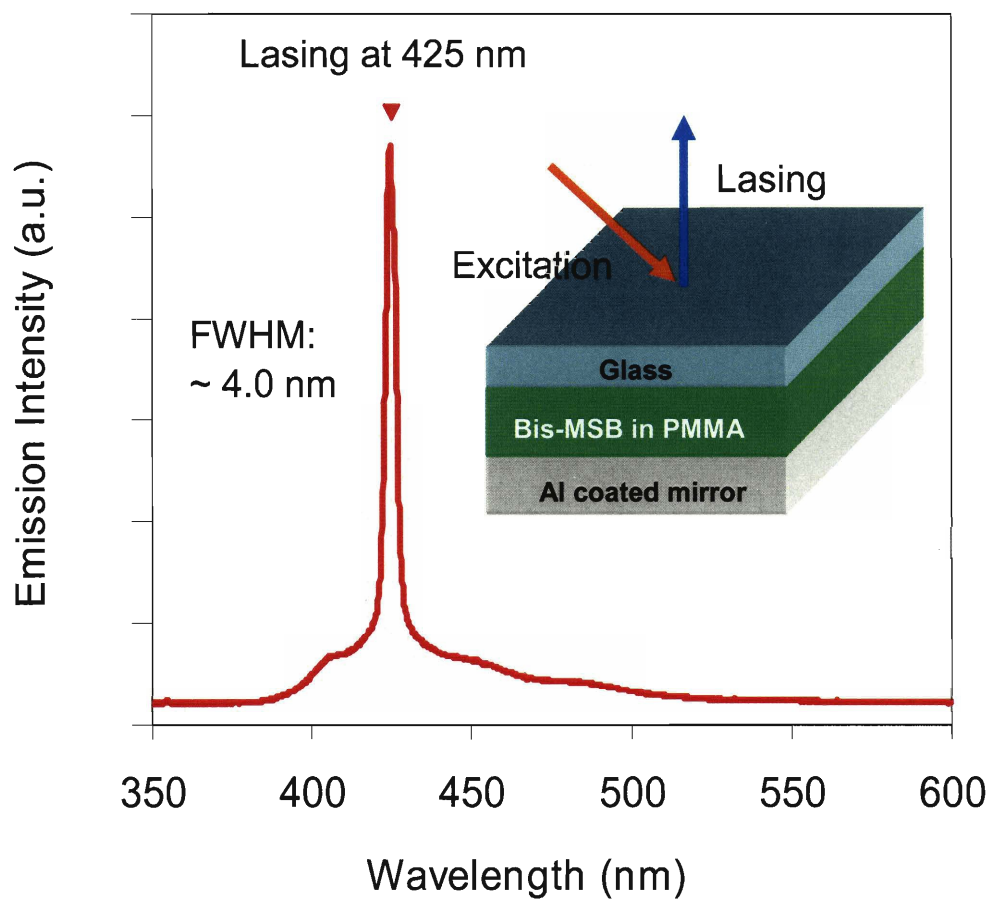


Figure 4.8: Lasing spectrum from a solid film of Bis-MSB (0.1 wt %) in PMMA sandwiched between an aluminum-coated mirror and a glass slide pumped by 355 nm pulse laser, where the lasing peak occurs at 425 nm and the FWHM is 4 nm. The inset shows a schematic of the sample.

4.3. Conclusion

In summary, we have utilized thin films of a high molecular weight PS-b-PI block copolymer as a narrow spectral-band selective feedback element for constructing a laser cavity. With fluorescent organic laser dyes in a PMMA polymer matrix as a gain medium, optically pumped surface-emitting lasing action has been demonstrated. This block copolymer based photonic structure opens the possibility for creating all-organic, flexible, and self-assembled laser devices with fast and low-cost processing. Further studies regarding stimulus responsive tunable block copolymer photonic crystals with various parameters such as solvent (solvatochromic), temperature (thermochromic), mechanical strain (mechanochromic), and electric field (electrochromic) are currently under investigation and their applications for lasing, sensing, and display are quite promising (see Chapter 5 for more details).

4.4. References

1. Yoon, J.; Lee, W.; Thomas, E. L. "Self-assembly of block copolymers for photonic-bandgap materials" *MRS Bulletin* **2005**, 30, 721-726.
2. Bates, F. S.; Fredrickson, G. H. "Block copolymer thermodynamics: theory and experiment" *Annual Review of Physical Chemistry* **1990**, 41, 525-57.
3. Thomas, E. L.; Lescanec, R. L. "Phase morphology in Block Copolymer Systems" *Philosophical Transactions of the Royal Society A* **1994**, 348, 149-166.
4. Urbas, A.; Fink, Y.; Thomas, E. L. "One-dimensionally periodic dielectric reflectors from self-assembled block copolymer-homopolymer blends" *Macromolecules* **1999**, 32, 4748-4750.
5. Deng, T.; Chen, C.; Honeker, C.; Thomas, E. L. "Two-dimensional block copolymer photonic crystals" *Polymer* **2003**, 44, 6549-6553.
6. Urbas, A. M.; Maldovan, M.; DeRege, P.; Thomas, E. L. "Bicontinuous cubic block copolymer photonic crystals" *Advanced Materials* **2002**, 14, 1850-1853.
7. Yoon, J.; Mathers, R. T.; Coates, G. W.; Thomas, E. L. "Optically transparent and high molecular weight polyolefin block copolymers toward self-assembled photonic band gap materials" *Macromolecules* **2006**, 39, 1913-1919.
8. Urbas, A.; Sharp, R.; Fink, Y.; Thomas, E. L.; Xenidou, M.; Fetters, L. J. "Tunable block copolymer/homopolymer photonic crystals" *Advanced Materials* **2000**, 12, 812-814.
9. Osuji, C.; Chao, C. Y.; Bitá, I.; Ober, C. K.; Thomas, E. L. "Temperature-dependent

- photonic bandgap in a self-assembled hydrogen-bonded liquid-crystalline diblock copolymer" *Advanced Functional Materials* **2002**, 12, 753-758.
10. Bockstaller, M.; Kolb, R.; Thomas, E. L. "Metallodielectric photonic crystals based on diblock copolymers" *Advanced Materials* **2001**, 13, 1783-1786.
 11. Fink, Y.; Urbas, A. M.; Bawendi, M. G.; Joannopoulos, J. D.; Thomas, E. L. "Block copolymers as photonic bandgap materials" *Journal of Lightwave Technology* **1999**, 17, 1963-1969.
 12. Valkama, S.; Kosonen, H.; Ruokolainen, J.; Haatainen, T.; Torkkeli, M.; Serimaa, R.; Ten Brinke, G.; Ikkala, O. "Self-assembled polymeric solid films with temperature-induced large and reversible photonic-bandgap switching" *Nature Materials* **2004**, 3, 872-876.
 13. Jakubiak, R.; Bunning, T. J.; Vaia, R. A.; Natarajan, L. V.; Tondiglia, V. P. "Electrically switchable, one-dimensional polymeric resonators from holographic photopolymerization: A new approach for active photonic bandgap materials" *Advanced Materials* **2003**, 15, 241-244.
 14. Finkelmann, H.; Kim, S. T.; Munoz, A.; Palffy-Muhoray, P.; Taheri, B. "Tunable mirrorless lasing in cholesteric liquid crystalline elastomers" *Advanced Materials* **2001**, 13, 1069-1072.
 15. Lawrence, J. R.; Ying, Y. R.; Jiang, P.; Foulger, S. H. "Dynamic tuning of organic lasers with colloidal crystals" *Advanced Materials* **2006**, 18, 300-303.
 16. Ndoni, S.; Papadakis, C. M.; Bates, F. S.; Almdal, K. "Laboratory-Scale Setup For Anionic-Polymerization Under Inert Atmosphere" *Review of Scientific Instruments*

- 1995, 66, 1090-1095.
17. Born, M.; Wolf, E., *Principle of Optics, 7th edition*. Cambridge University Press: Cambridge, 1999.
 18. Siegman, A. E., *Lasers*. University Science Books: Palo Alto, 1986.
 19. Dienes, A. "Comparative Gain Measurements For 12 Organic Laser Dye Solutions" *Applied Physics* **1975**, 7, 135-139.
 20. Itoh, U.; Takakusa, M.; Moriya, T.; Saito, S. "Optical Gain Of Coumarin Dye-Doped Thin-Film Lasers" *Japanese Journal of Applied Physics* **1977**, 16, 1059-1060.

Chapter 5.

Chemically, Thermally, and Mechanically Responsive Tunable Self-Assembled Reflectors Based on Block Copolymer Photonic Crystals

In this chapter, we present three types of stimulus responsive tunable self-assembled reflectors based on block copolymer one-dimensional (1D) photonic crystals. Three external stimuli: (1) solvent, (2) temperature, and (3) compressive mechanical strain were used to modulate the microstructural and material properties including the domain thickness, the domain orientation, and the effective refractive indices of the respective microdomains, resulting in effective tuning of the spectral response of block copolymer photonic structures.

The work on solvatochromism was in collaboration with Dr. Wonmok Lee and Dr. Hyunjung Lee.

5.1. Introduction

Over the past two decades, interest in the possibility of next generation optoelectronic devices has motivated considerable research efforts into photonic crystals.¹⁻⁴ In particular, switchable or tunable photonic bandgap materials have been highly sought after due to their potential to create numerous applications such as variable-wavelength lasers, sensor platforms, switchable color filters, and reflective color display devices.⁵⁻¹² The dispersion relation ($\omega(\mathbf{k})$) of a photonic crystal can be tuned by tailoring a combination of the two characteristic parameters, namely the thicknesses and the refractive indices of the respective domains. A host of materials systems and numerous external fields have been employed to fabricate tunable photonic crystals. Various one- (1D), two- (2D), three-dimensional (3D) photonic bandgap structures doped with nematic liquid crystals (LCs) have been extensively investigated as electro-optic or thermo-optic tunable optical elements, where the refractive index of the LC-containing domains is modulated as the optic-axis orientation of the LC mesogens varies with electric fields or as the phase of LC mesogens changes with temperature, leading to a tunability of the band gap or of localized defect-modes.^{5, 9} Another interesting strategy is to use photonic crystals based on elastomeric (rubber or gels) materials, where the lattice dimension can change in response to various applied mechanical, chemical (e.g. pH or ionic strength), or thermal fields, resulting in a reversible shift in spectral responses.^{6-8, 12-14}

Recently, block copolymers have attracted increasing attention as a versatile material platform for creating photonic crystals, due in large part to a range of accessible

periodic structures and a possibility to accommodate various optically active/passive guest molecules to engineer desired functionalities.¹⁵ Block copolymer based photonic structures also offer novel routes to tune the photonic band gap by manipulating microstructural and material properties. Indeed, block copolymer based photonic crystals provide a much larger range of tunability compared to inorganic based photonic crystals. One previous method of altering the peak reflectivity of 1D lamellar stack involved swelling block copolymers with homopolymers, where the microdomain size or the stop band of the blends depends on the amount of added homopolymers.¹⁶ The idea of using a nanocomposite composed of block copolymers and surface-functionalized inorganic nanoparticles offered another way to tune and enhance photonic properties of block copolymer based photonic materials.^{17, 18} Block copolymers having LC-containing block have been also demonstrated as thermally tunable photonic bandgap structures either by changing the domain spacing and/or the refractive index of the LC-containing domains with thermal fields.^{10, 19}

In this chapter, we illustrate three types of stimulus responsive self-assembled reflectors based on block copolymer one-dimensional (1D) photonic crystal gels, in which a dynamic control of microstructural and material properties are achieved through the application of solvent, thermal, and mechanical fields.

5.2. Results and Discussion

For better understanding of the experimental optical responses of the 1D block

copolymer reflectors in this study, we first examine the effect upon its photonic bandgap properties of the characteristic parameters such as the lattice constant, lattice orientation, and effective refractive indices of the respective domains of a model finite 1D photonic crystal. We characterize the center wavelength (λ_{\max}), the width ($\Delta\omega$), and the magnitude (R_{\max}) of the photonic stop band. The reflectivity spectra of the model photonic bandgap structure has been computed using a transfer matrix method (TMM)²⁰. The model 1D photonic crystal is composed of N layers of alternating high (n_H) and low (n_L) refractive domains having domain thicknesses of d_H and d_L as schematically presented in Figure 5.1.

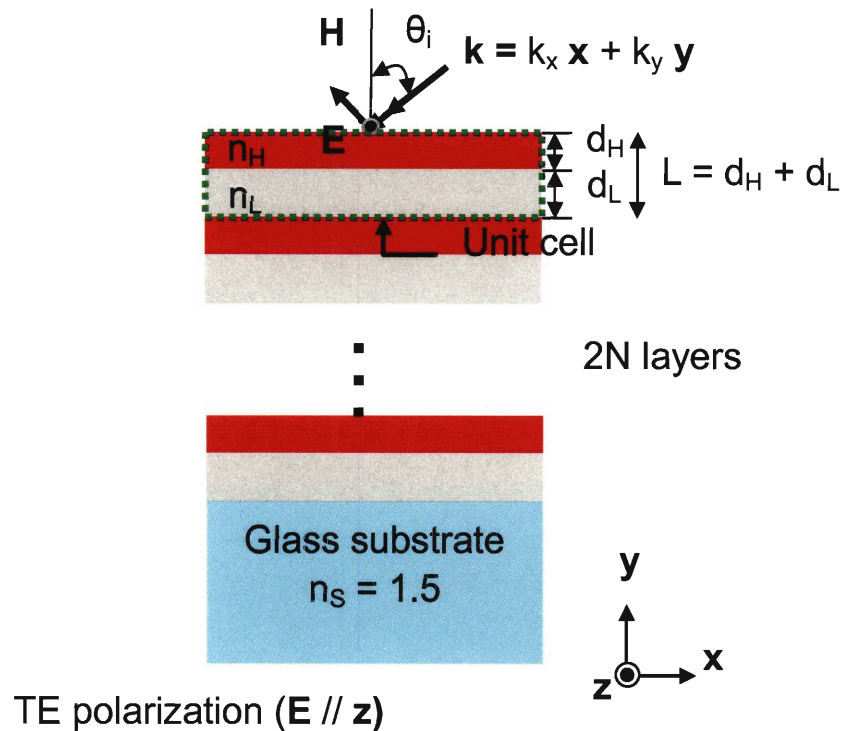


Figure 5.1: A schematic of a model 1D photonic crystal, air-(high index layer-low index layer)^N-glass substrate, with incident electromagnetic wave of a transverse-electric (TE) polarization (the electric field vector (\mathbf{E}) is perpendicular to the plane of incidence or parallel to the z -axis (\mathbf{z})).

The spectral position of photonic band gap scales with the lattice constant.²¹ As the lattice constant becomes larger, the wavelength of electromagnetic waves that satisfy the Bragg condition also increases due to the increased optical thickness ($n \times d$, n : refractive index, d : domain thickness). This results in a shift of the bandgap toward longer wavelengths. The lattice constant also affects the width of the bandgap. If the respective refractive indices and layer numbers are held constant, the bandgap width ($\Delta\omega$) increases with increasing lattice constant. Figure 5.2 shows normal incidence reflectivity spectra obtained from TMM calculations of 1D photonic crystals having a range of domain periodicity ($L = d_H + d_L$, $d_H = d_L$) with the constant refractive indices ($n_H = 1.59$, $n_L = 1.51$) and fixed total number of layers ($2N = 50$). As the domain periodicity increases from 120 nm to 280 nm, both the bandgap center wavelength (λ_{max}) and the bandgap width (FWHM) also increase. However, the magnitude of the reflectivity remains constant.

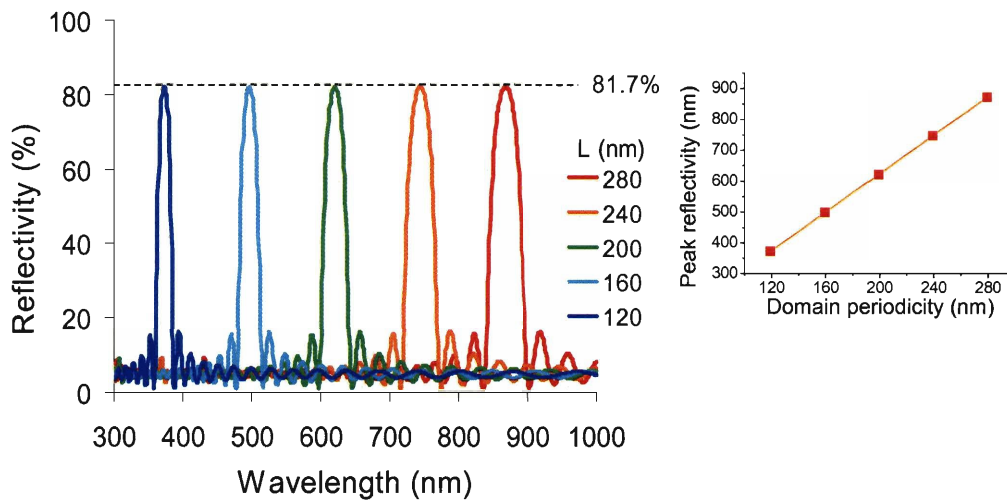


Figure 5.2: Reflectivity spectra of model 1D photonic crystals at normal incidence as a function of the domain periodicity ($L = d_H + d_L$, $d_H = d_L$), assuming constant refractive indices ($n_H = 1.59$, $n_L = 1.51$) and fixed total number of layers ($2N = 50$). The peak reflectivity wavelength at each domain periodicity is shown in the inset.

The refractive index also affects the spectral characteristics of photonic crystals. As the refractive indices of respective domains increase, the reflectivity spectrum shifts to a longer wavelength range due to the increased optical thickness. The refractive index contrast (n_H/n_L) is also important. In particular, the bandgap width ($\Delta\omega$) varies with the refractive index contrast quite sensitively. As the refractive index contrast increases, the bandgap width also increases. Figure 5.3 shows reflectivity spectra of a model 1D photonic crystal (see Figure 5.1) at normal incidence as a function of a refractive index contrast (n_H/n_L), assuming constant domain thicknesses ($d_H = d_L = 100$ nm) and a fixed number of layers ($2N = 20$). As the refractive index contrast increases from 1.5/1.4 to 1.5/1.0, the bandgap width (FWHM) increases from 58 nm to 148 nm. The blue-shift of the peak reflectivity wavelength (λ_{\max}) with increased refractive index contrast results from the decreased optical thickness of the low index layers. The strength of bandgap is also affected by the index contrast. Equation 5.1 is the analytical solution of peak reflectivity (R) of quarter-wave stacks ($n_H d_H = n_L d_L = \lambda_0/4$, λ_0 : center wavelength of the bandgap) having $2N$ alternating layers at normal incidence and is graphically presented in Figure 5.4.²⁰ With constant domain thicknesses and a fixed total number of layers, the reflectivity increases with the index contrast, which is also clearly shown in Figure 5.3.

$$R = \left\{ \frac{1 - \left(\frac{n_L}{n_H} \right)^{2N}}{1 + \left(\frac{n_L}{n_H} \right)^{2N}} \right\}^2 \quad (5.1)$$

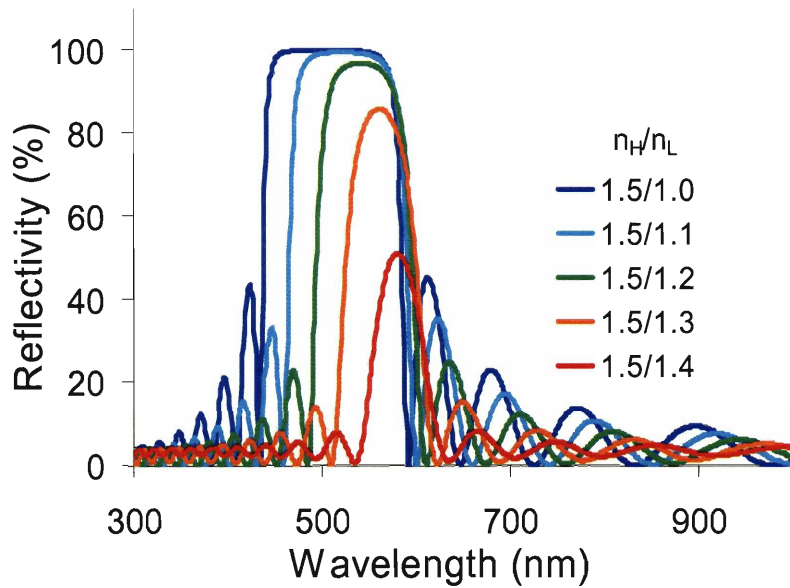


Figure 5.3: Reflectivity spectra at normal incidence of a model 1D photonic crystal (Figure 5.1) as a function of the refractive index contrast (n_H/n_L), assuming constant domain thicknesses ($d_H = d_L = 100$ nm) and a fixed total number of layers ($2N = 20$).

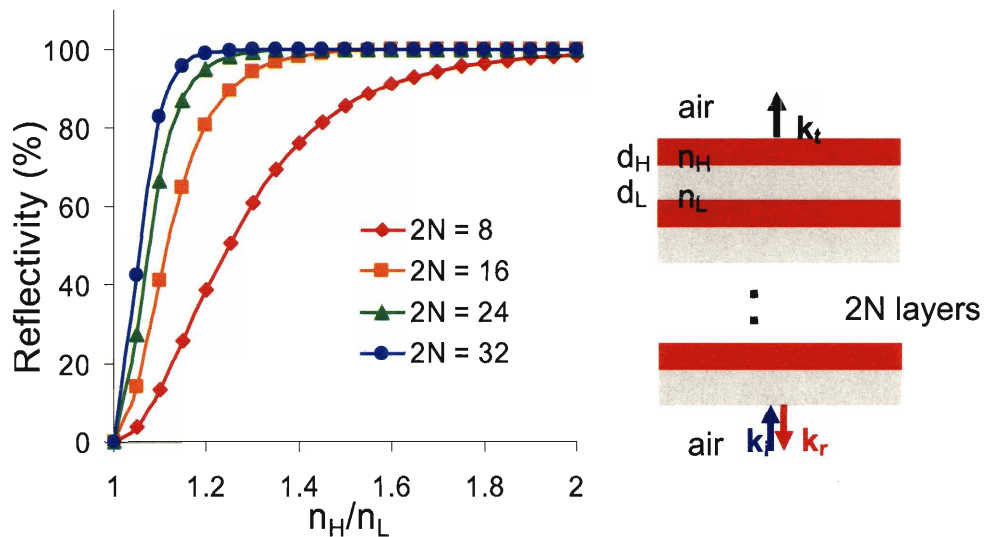


Figure 5.4: Peak reflectivity of quarter-wave multilayer stacks (see the inset) at normal incidence as a function of refractive index contrast (n_H/n_L) and a total number of layers ($2N$) from Equation 5.1. ($d_H = \lambda_0/4n_H$, $d_L = \lambda_0/4n_L$, \mathbf{k}_i : incident wave vector, \mathbf{k}_r : reflected wave vector, \mathbf{k}_t : transmitted wave vector).

The effect of domain orientation is equivalent to the effect of the direction of the incident light. Given a certain direction (\mathbf{k}) of the incident electromagnetic waves, the variation of domain orientation has the same effect as the variation of incidence angle with a fixed domain orientation as schematically shown in Figure 5.5. Figure 5.6 shows calculated reflectivity maps of the dielectric multilayer structure, where the reflectivity strength is displayed as a function of incidence angle, wavelength, and polarization of incident electromagnetic waves for (a) low refractive index contrast ($n_H/n_L = 1.59/1.51 \sim 1.05$) and (b) high refractive index contrast ($n_H/n_L = 2.27/1.51 \sim 1.50$), assuming quarter-wave layer thicknesses of 500 nm and total 30 layers ($2N = 30$). As the incidence angle increases from normal incidence ($\theta = 0^\circ$) to grazing angle ($\theta = 90^\circ$), the reflectivity peak moves to a lower wavelength range (blue-shift). However, if the refractive index contrast is sufficiently large ($n_H/n_L > \sim 1.5$), there exists a wavelength range where the reflectivity is independent of the incidence angle, or *omnidirectional*.²²

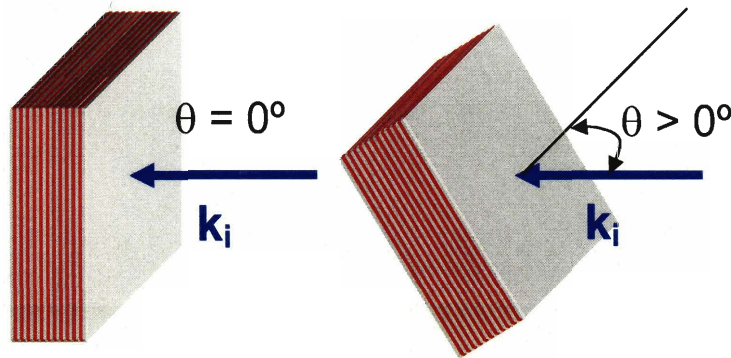


Figure 5.5: Schematic of 1D photonic crystals having different domain orientations with respect to a certain direction of incident light (\mathbf{k}_i), (a) $\theta = 0^\circ$, (b) $\theta > 0^\circ$.

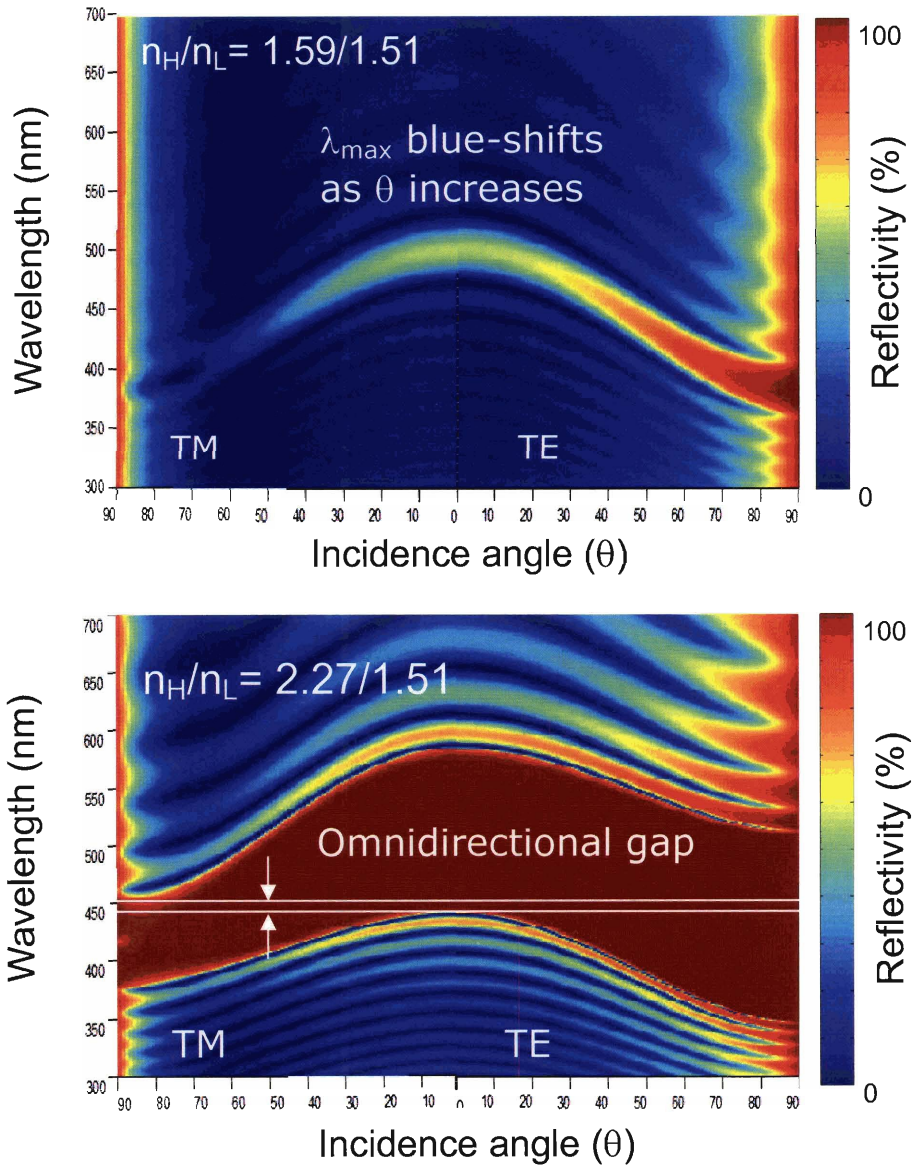


Figure 5.6: Reflectivity map computed by TMM for a 15-period ($2N = 30$) stack of alternating high and low index layers for (a) low refractive index contrast ($n_H/n_L = 1.59/1.51$) and (b) high refractive index contrast ($n_H/n_L = 2.27/1.51$) for TE (right) and TM (left) polarizations, assuming quarter-wave layer thicknesses of 500 nm and total 30 layers. The color represents the strength of the reflectivity at a particular frequency, a polarization, and an angle of incidence. The omnidirectional reflectivity band is shown for the high refractive index contrast 1D photonic crystal.

Now we examine the tunability of self-assembled reflectors based on block copolymers. Three types of external stimuli, (1) solvent (solvatochromic), (2) temperature (thermochromic), and (3) compressive mechanical strain (mechanochromic), are applied for dynamic control of microstructural and material properties of block copolymer photonic crystals.

A high molecular weight poly(styrene-*b*-isoprene) (PS-*b*-PI) block copolymer sample was synthesized via anionic polymerization with sequential addition of styrene and isoprene monomer in cyclohexane/benzene mixed solvent. The molecular weight and composition of the block copolymer was determined to be 8.40×10^5 g/mol (PDI: 1.08), 57/43 (PS/PI, wt/wt) by gel permeation chromatography (GPC) and nuclear magnetic resonance (NMR) analysis. Figure 5.7 is a bright field transmission electron microscopy (TEM) micrograph from the cryomicrotomed sample of the PS-*b*-PI block copolymer exhibiting the 1D periodic lamellar morphology, in which the dark regions correspond to the PI domains preferentially stained with osmium tetroxide (OsO_4) and the bright regions correspond to the PS domains. The domain periodicity from the TEM micrograph is approximately 200 nm (PS: 110 nm, PI: 90 nm). Samples were fabricated by casting solutions of the lamellar-forming PS-*b*-PI block copolymer in a solvent (cumene for solvato-, thermochromic study, dioctyl phthate (DOP) for mechanochromic study) between two glass substrates.

Figure 5.8 shows a time-sequence of pictures taken of a block copolymer based self-assembled reflector exhibiting a *solvatochromism*, i.e. the color of this material system changes as a function of solvent concentration which varies with time.²² As the

concentration of block copolymers in the solution increases and reaches the order-to-disorder transition concentration (ϕ_{ODC}), the transparent block copolymer solution microphase separates to form 1D periodic dielectric multilayers. Since the domain spacing of the block copolymer is on the order of the wavelength of visible light, the multilayer structure from the confined block copolymer solution exhibits a visible wavelength partial photonic bandgap in the blue. As the solvent evaporation proceeds through the rim of the sample, i.e. in the radial direction, the concentration gradient ($\nabla\phi(\mathbf{r})$), gives rise to concentric regions exhibiting different colors as shown in Figure 5.8. The blue reflective region is in the center and becomes smaller over time while the red or orange region at the edge grows larger as the solvent concentration decreases.

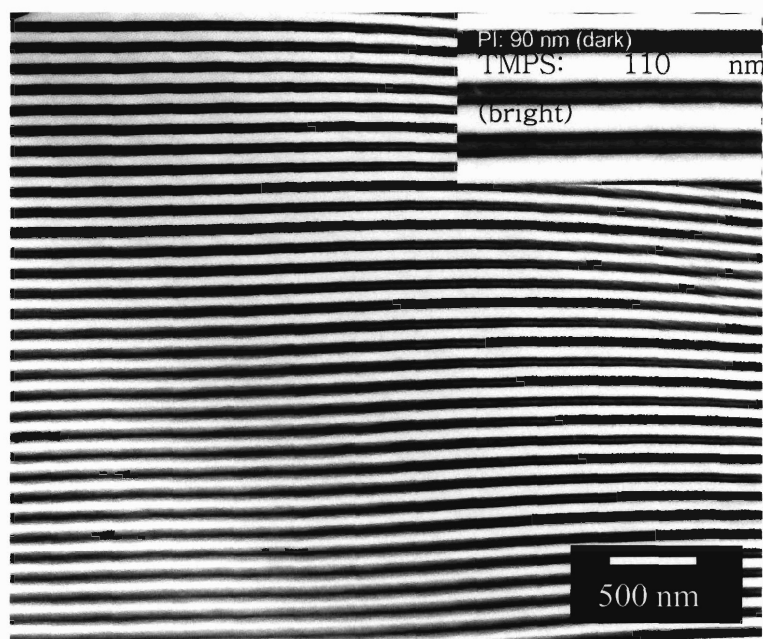


Figure 5.7: Bright field TEM micrograph of crymictotomed PS-b-PI block copolymer, in which PI domains are preferentially stained with OsO_4 . The domain periodicity from the TEM micrograph is approximately 200 nm (PS: 110 nm, PI: 90 nm).

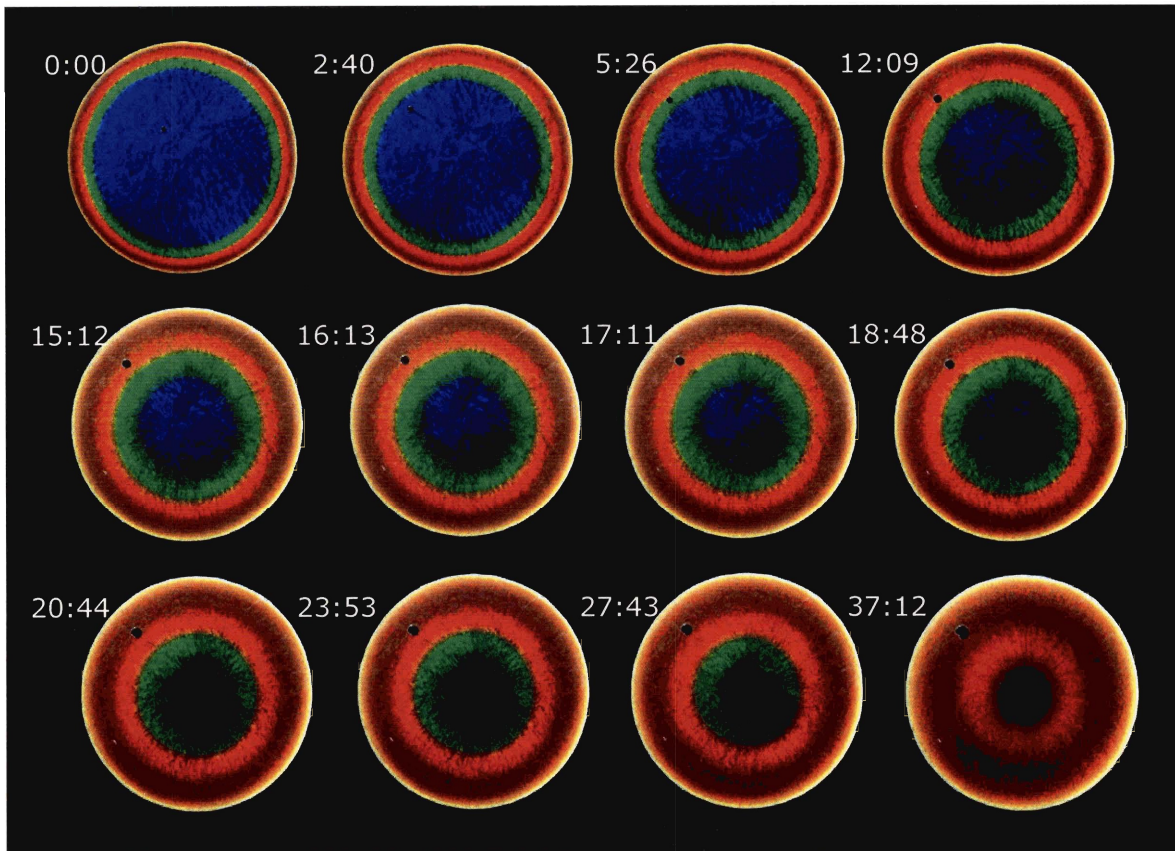


Figure 5.8: A series of pictures taken from confined block copolymer gel at different solvent evaporation times (e.g. 2:40 means 2 h 40 min). These pictures were taken by Felice Frankel at MIT.

Figure 5.9 shows the corresponding reflectivity spectra taken from the sample in the early stage of solvent evaporation at various radial positions from the center to the edge using normal incidence light. Reflectivity spectra were taken using an optical microscope (Zeiss Axioscop) equipped with a fiber-optic spectrometer (Stellarnet EPP2000) with a silver-coated metallic mirror as a 100% reference. Due to the effect of the numerical aperture of objective lens (10X, $N.A. = n_{\text{air}} \sin\theta = 0.3$), the reflectivity spectrum is not a pure normal

incidence spectrum but a convolution of multiple reflectivity spectra over the incidence angles of 0° to $\sim 17.5^\circ$. The measured reflectivity shows that the range of colors from this sample covers nearly the entire visible wavelength regime. As the concentration of the block copolymer increases, the reflectivity moves towards longer wavelength range (from blue (488 nm) to red (677 nm)) and the width of reflectivity band (the full width at half maximum, FWHM) gets broader (from 11 nm to 57 nm).

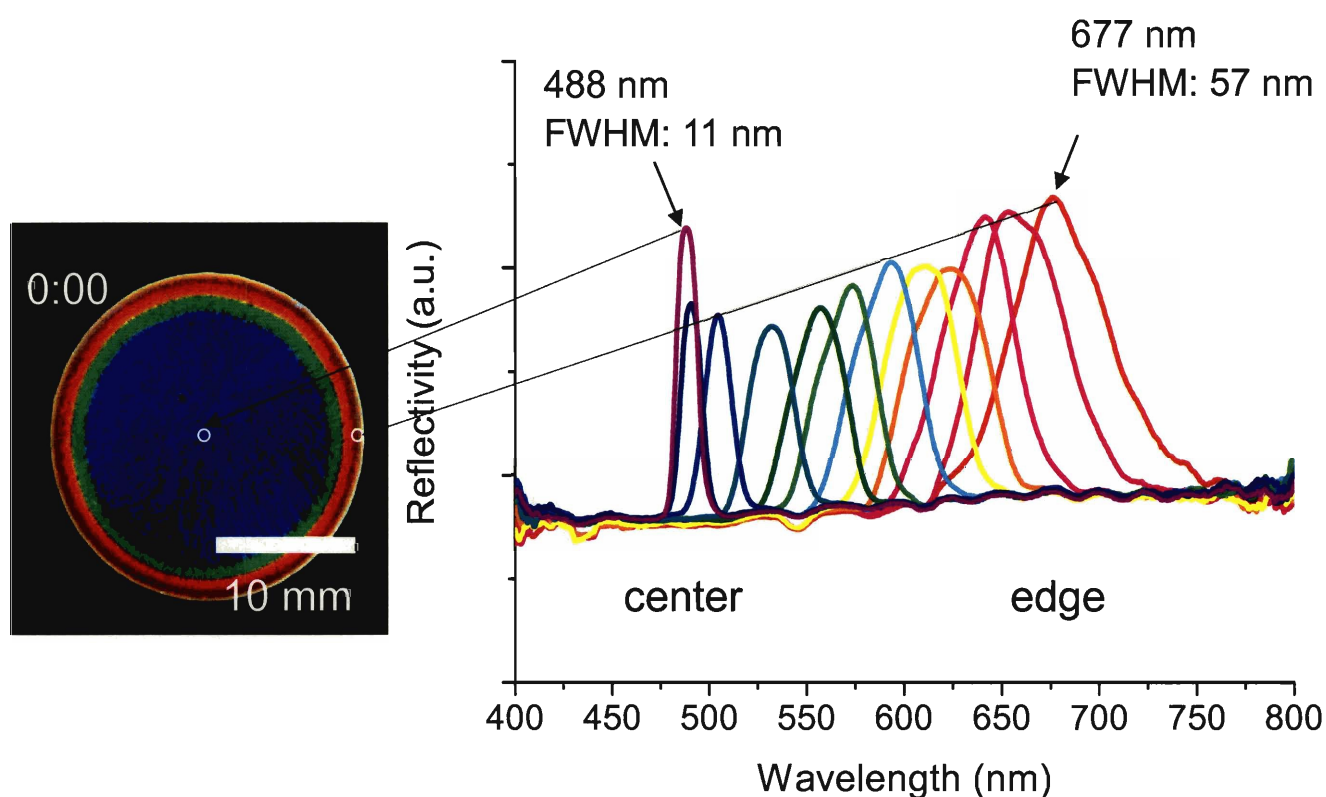


Figure 5.9: Reflectivity spectra taken in the early stage of solvent evaporation at various radial positions from the center to the edge with normal incident light using a microscope spectrometer. Note the continuous change in the peak wavelength with radial distance from the sample center. The sample in the photograph appears to the eye as having a large single color near the center, but the measured spectra show a significant variation of the actual color with radial position.

The observed solvatochromic effect can be understood by considering the effect of the solvent on the microstructural and materials properties of block copolymer gels such as the domain spacing, the domain orientation, and the effective refractive index of the respective lamellar microdomains, all of which can sensitively affect the spectral characteristics of the system. Obviously, over the time the solvent concentration of the system is decreasing, leading to an increase in the refractive index contrast (n_H/n_L). Also solvents can induce changes in the respective layer spacings (d_H and d_L). Additionally, there may be a re-orientation of the lamellae upon solvent evaporation. First we examine the effect of re-orientation of the block copolymer lamellae with different solvent concentrations. As previously described, the lamellar domain orientation can contribute to the shift of the reflectivity band of 1D photonic crystal. But it is reasonable to assume that this lamellar re-orientation is not a dominant factor for explaining observed “rainbow” reflectivity spectra in the current system. This can be understood as follows. If the film thickness is not too large, the orientation of block copolymer lamellae confined between two flat substrates tends to be parallel to the surface.^{23,24} Especially near the center area of the sample (the blue reflective region) the solvent concentration is relatively higher than the edge and both the PS and PI chains have enough mobility at room temperature for the surface-directed organization. The well-ordered lamellar orientation is also supported by the narrow FWHM (~ 11 nm) of the reflectivity band observed near the center of the specimen. As the solvent concentration decreases toward the edge, the mobility of polymer chains decreases and therefore the effect of surface becomes weaker. At some critical concentration, the glass transition temperature of the PS block passes through room

temperature and the microstructure of block copolymer becomes kinetically frozen. Poorer lamellar ordering with decreased solvent concentration partly explains why the FWHM of reflectivity band becomes larger from the center to the edge, in which the surface-induced uniformity of lamellar orientation is limited, due to the shorter time the system has to adopt the lamellae parallel to the substrate orientation. Moreover if there were any re-orientation of the lamellae from the parallel orientation, this would contribute to the blue-shift of bandgap instead of the observed red-shift of the measured reflectivity. Thus lamellar re-orientation is essentially ruled out as an explanation for the observed reflectivity spectra.

We next consider the variation of the domain spacing and the effective domain refractive index in the presence of a solvent. The effect of a solvent on the lamellar domain spacing can be understood by considering the effective repulsive potential (or χ_{eff} , the effective Flory-Huggins interaction parameter) between PS and PI blocks under different solvent concentrations.

In a block copolymer solution with a nonselective neutral solvent, there exist two competing effects of the solvent on the lamellar microdomain formation.^{25, 26} One obvious effect of the added solvent is to swell the microdomain and increase the domain spacing. On the other hand, the segregation strength (χ_{eff}) between PS and PI chains decreases with increasing solvent concentration due to a screening effect by solvent molecules and consequently the block copolymer chains can adopt more random-coil configurations, resulting in a decrease of the lamellar domain spacing. If this de-swelling effect due to the decreased segregation strength outweighs the swelling effect due to the added solvent, the resulting lamellar domain spacing can decrease with increasing solvent concentration and

this corresponds to the observed blue-shift of reflectivity spectra with increasing solvent concentration in this study. In the same manner, as a solvent concentration decreases with evaporation, the segregation strength between blocks increases and the polymer chains get more extended to minimize mixing free energy of the unlike segments. If this effect prevails over the de-swelling effect due to decreased volume of solvent, the lamellar domain spacing can increase. This can explain why the reflectivity spectra red-shift from the center to the edge as the solvent concentration increases.

The other important physical factor which can be affected by a solvent is the effective refractive indices of the respective domains. Both the refractive index of each domain and the refractive index contrast between high and low refractive domains are modulated by an added solvent. Figure 5.10 shows the effective refractive indices of PS and PI domains as a function of solvent concentration with three nonselective solvents of different refractive indices assuming a simple rule of mixing, i.e. $n_{\text{eff}} = n_p \cdot (1 - w_s) + n_s \cdot w_s$, where n_{eff} is the effective refractive index of a solvent-containing domain, n_p is the refractive index of polymer, n_s is a refractive index of solvent, and w_s is the weight fraction of solvent.

Depending on the refractive index of a solvent, the effective refractive index of each domain changes differently. If the refractive index of a solvent is smaller than both PS and PI, which is the case (c) in Figure 5.10 as in the present study, the effective refractive indices of both PS and PI domains decrease. If the refractive index of a solvent is larger than both PS and PI (case (a) in Figure 5.10), the effective refractive indices of both PS and PI domains increase. If the refractive index of a solvent is between PS and PI (case (b) in

Figure 5.10), the effective refractive index of PS domain decreases while that of PI domain increases. These different trends can be also illustrated by an average effective refractive index, which is defined as $n_{avg} = (n_{eff, H} + n_{eff, L})/2$. As shown in Figure 5.11, the average effective refractive index can increase ($n_s > n_H > n_L$), decrease ($n_s < n_L < n_H$), or even be constant ($n_s = (n_H + n_L)/2$) with increasing solvent concentration.

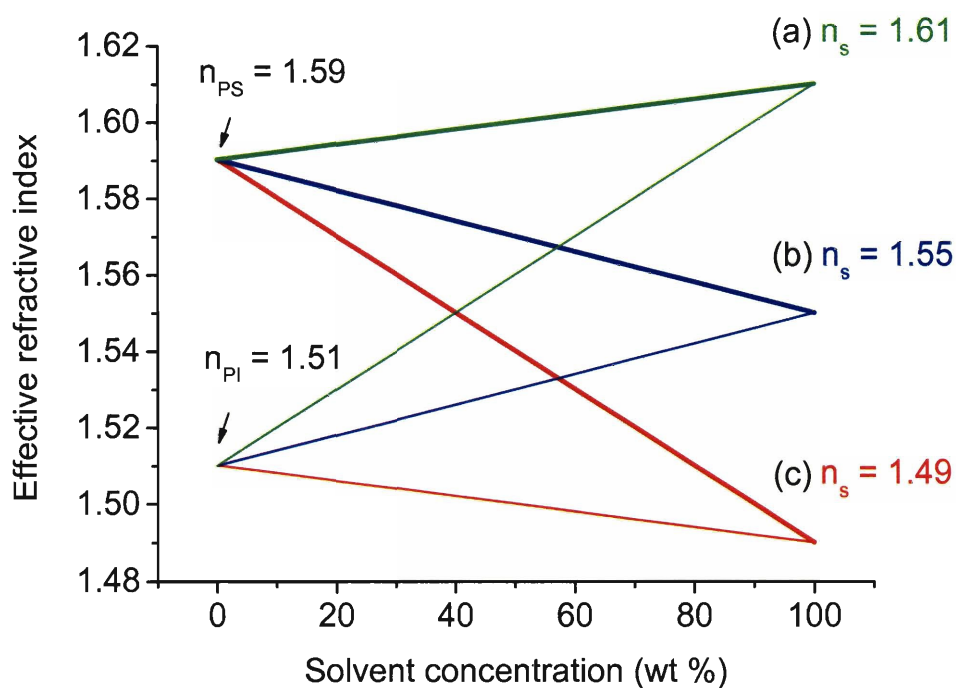


Figure 5.10: Effective refractive indices of PS (thick line) and PI (thin line) microdomains as a function of solvent concentration at various solvent refractive indices, (a) $n_s = 1.61 > n_H > n_L$, (b) $n_H > n_s = 1.55 > n_L$, (c) $n_H > n_L > n_s = 1.49$. Case (c) is relevant to the experiments on PS-b-PI with cumene ($n = 1.49$).

The effective refractive index contrast decreases with solvent concentration regardless of the solvent refractive index as shown in Figure 5.10. In the case of a

nonselective neutral solvent, the effective refractive index contrast (Δn_{eff}) is independent of a choice of solvent and represented by $\Delta n_{\text{eff}} = (1 - \phi_s)(n_H - n_L)$.

As a consequence of this solvent-induced refractive index variation both the center wavelength and the width of the bandgap can change for the present system of a PS-b-PI diblock and cumene. As the refractive indices of the respective domains decrease with increased cumene concentration, the optical thickness of each domain also decreases, leading to a peak narrowing and a blue shift of the bandgap center, which is in agreement with the experimental data.

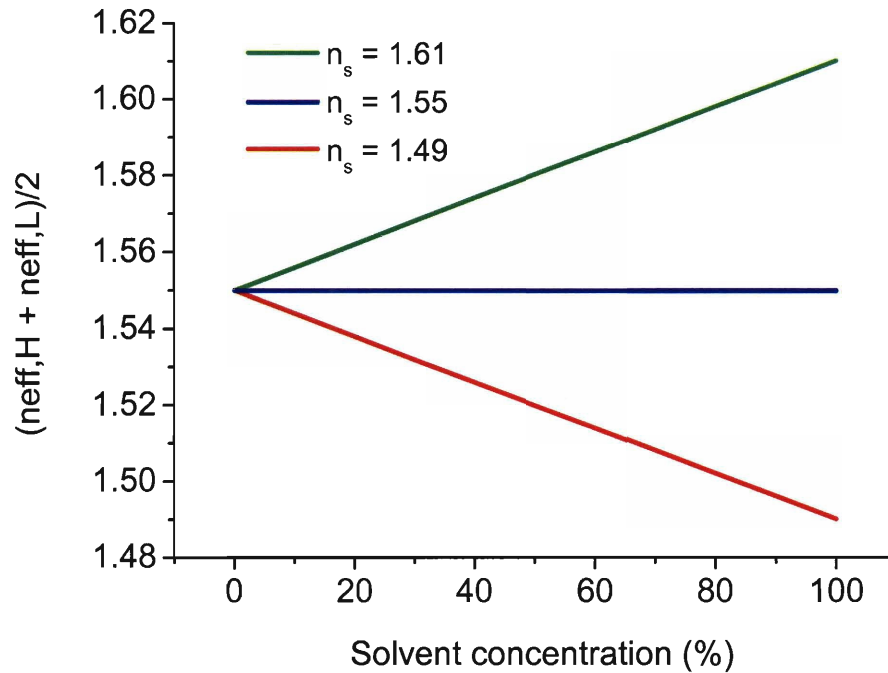


Figure 5.11: Average effective refractive indices ($n_{\text{avg}} = (n_{\text{eff}, H} + n_{\text{eff}, L})/2$) as a function of solvent concentration at various solvent refractive indices, (a) $n_s = 1.61 > n_H > n_L$, (b) $n_H > n_s = 1.55 > n_L$, (c) $n_H > n_L > n_s = 1.49$. Case (c) is relevant to the experiments on PS-b-PI with cumene ($n = 1.49$).

Next we examine *thermochromism*, or the effect of temperature on bandgap characteristics, of a 1D photonic crystal fabricated from a block copolymer-solvent gel where the composition of the system is held approximately constant as the temperature is varied. For this experiment, the lamellar-forming PS-*b*-PI block copolymer in cumene was cast between two glass substrates and then sealed with a fast-curing epoxy to maintain a constant solvent concentration. Using a temperature-controllable hot stage (Linkam), the sample temperature was varied and the reflectivity spectra at normal incidence were measured at various temperatures on a fiber-optic spectrometer attached to a microscope. Figure 5.12 shows measured reflectivity spectra between 30 °C and 140 °C in 10 °C increments. The sample temperature was increased at a rate of 5 °C/min and the reflectivity data were taken after the system reached thermal equilibrium (after ~ 10 minutes) and the reflectivity peak was stationary. As the temperature increases, the peak reflectivity shifts to shorter wavelengths from 510 nm (30 °C) to 450 nm (140 °C) while the width of reflectivity band remains almost unchanged (FWHM: ~ 12 nm). It was also observed that this thermochromic effect was reversible (data not included here).

The temperature dependence of refractive indices of solvent (cumene) and the polymers (PS and PI) provides a partial explanation for the observed thermochromism of the block copolymer gel. The thermally induced decrease in the density (ρ) of the solvent and the polymer ($dp/dT < 0$) results in the decrease of their respective refractive indices (n) with temperature, $dn/dT < 0$, which contributes to the decrease of the optical thickness of layers and therefore shifts the reflectivity band to a shorter wavelength range. A second important effect of temperature on the block copolymer gel is the change of lamellar

domain spacing due to the change of the segregation strength between PS and PI blocks with increased temperature (this effect far outweighs thermal expansion). When the block copolymer concentration is constant, the lamellar spacing decreases with temperature due to the decreased segregation strength ($\chi \sim 1/T$, χ is the Flory-Huggins interaction parameter between repeat units of block copolymers) and due to the resulting relaxation of the stretched chains, which also contributes to the blue-shift of reflectivity band with temperature. Hashimoto and co-workers showed that the thermodynamically controlled lamellar domain periodicity (L) varies with absolute temperature (T) given by $L \sim (1/T)^{1/3}$ for a nonselective solvent.^{26,27}

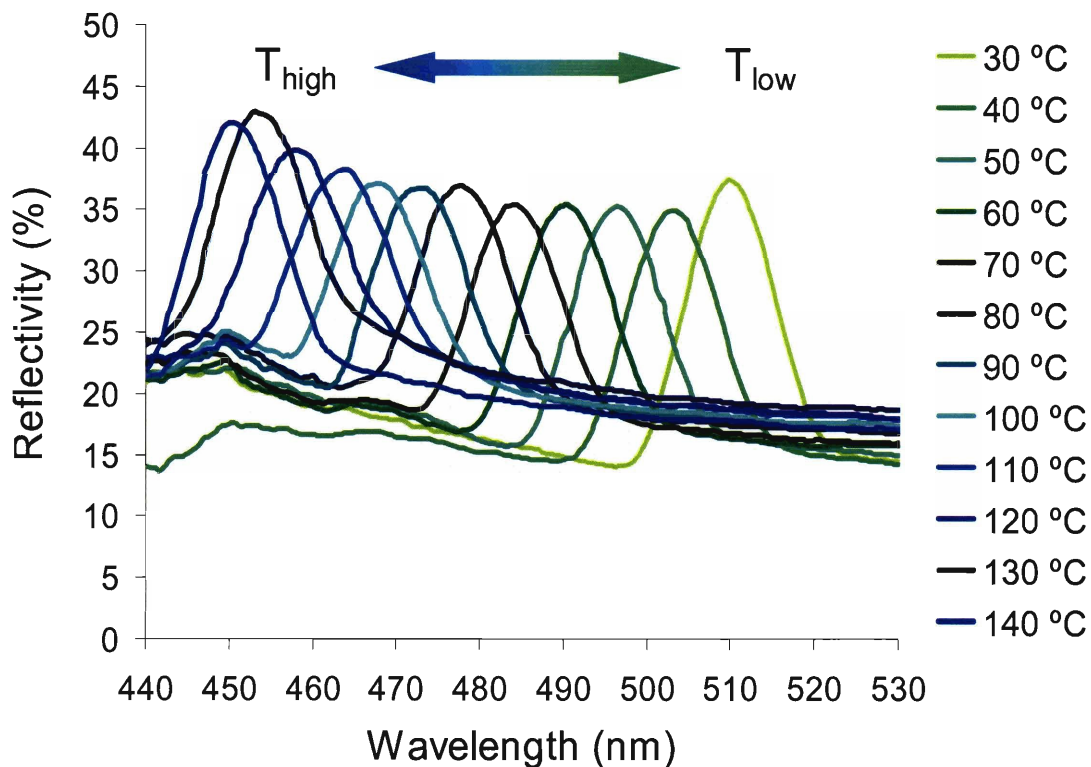


Figure 5.12: Measured reflectivity spectra of the block copolymer lamellar photonic gel at various temperatures between 30 °C and 140 °C.

In order to examine the competition of these two effects on sample reflectivity, we calculated the shift of the reflectivity band due to the change of refractive index, domain spacing and both of these two factors with temperature. Given the experimentally measured reflectivity spectrum at 30 °C, in which the peak reflectivity occurs at 510 nm with a FWHM of 12 nm, we first estimated an initial solvent concentration, domain thicknesses, and refractive indices. For this estimation, we modeled our system as a perfect 1D photonic crystal in TMM calculation and assumed refractive indices of PS and PI at 30 °C as 1.590 and 1.510, a uniform lamellar orientation parallel to the glass substrates (a normal incidence of light), a constant ratio of PS and PI domain thicknesses (i.e. $d_{PS}/d_{PI} = 1.1/0.9$ as observed in TEM for a dried sample), and total 400 layers.

$d_{eff, PS}$ (nm)	$d_{eff, PI}$ (nm)	Peak reflectivity wavelength (nm)
90.0	73.6	506.5
90.2	73.8	507.5
90.4	74.0	508.5
90.6	74.1	510.0
90.8	74.3	511.0
91.0	74.5	512.5

Table 5.1: Calculated normal incidence peak reflectivity wavelengths of a PS-b-PI photonic gel in a range of domain thicknesses with 10 wt % solvent concentration, assuming refractive indices of high and low index layers as 1.580 and 1.508, a fixed ratio of PS and PI domain thicknesses ($d_{PS}/d_{PI} = 1.1/0.9$), and total 400 layers.

For example, at 10 wt % of solvent concentration, the refractive indices of PS and PI domains are calculated as 1.580 and 1.508 if we apply a simple rule of mixing. With these effective refractive indices, we can determine domain thicknesses which give a reflectivity peak at 510 nm. Table 5.1 summarizes the peak reflectivity wavelengths for a range of domain thicknesses, from which the estimated lamellar spacings are 90.6 nm for PS and 74.1 nm for PI domain. In the similar manner, we can also estimate domain thicknesses at other solvent concentrations and FWHMs of the corresponding reflectivity spectra as summarized in Table 5.2. The initial solvent concentration was then determined as about 40 wt % for which the FWHM of the calculated reflectivity band approximately matches with the FWHM of the experimentally measured reflectivity spectra.

W_s (wt%)	n_{eff, PS}	n_{eff, PI}	d_{eff, PS} (nm)	d_{eff, PI} (nm)	FWHM (nm)
10	1.580	1.508	90.6	74.1	16.3
20	1.570	1.506	91.0	74.5	15.2
30	1.560	1.504	91.4	74.8	14.9
40	1.550	1.502	91.8	75.1	11.8
50	1.541	1.501	92.2	75.4	11.1

Table 5.2: Effective refractive indices and effective domain thicknesses of PS and PI domains at various solvent concentrations determined from TMM calculations, which give a peak wavelength of the corresponding reflectivity spectrum at 510 nm.

With the estimated refractive indices and domain thicknesses at 30 °C as an initial condition, we computed the shift of reflectivity band as a function of temperature, due to the change of 1) refractive indices of solvent and polymer, 2) lamellar domain spacings, and 3) both refractive indices and domain spacings. First, we examined the effect of temperature-dependent refractive indices on the peak wavelength of reflectivity spectra. Given dn/dT of the solvent ($\sim -5.68 \times 10^{-4} \text{ K}^{-1}$ (toluene), assumed to be the same value for toluene and cumene)²⁸ and of the polymer ($\sim -1.27 \times 10^{-4} \text{ K}^{-1}$ (PS), assumed same values for both PS and PI)²⁹, the effective refractive indices of respective domains were calculated at various temperatures between 30 °C and 140 °C. Further, assuming that the domain thicknesses are held constant as the estimated values at 30 °C (i.e. $d_{\text{eff, PS}}$: 91.8 nm, $d_{\text{eff, PI}}$: 75.1 nm), the corresponding reflectivity peak wavelengths as a function of temperature were obtained by TMM calculations as summarized in Table 5.3. Second, we investigated the effect of temperature-dependent lamellar thicknesses on the peak wavelength of reflectivity spectra. For this analysis, we adopted the scaling law by Hashimoto and co-workers, $L \sim (1/T)^{1/3}$, where L is the lamellar domain periodicity and T is absolute temperature.²⁷ Using this scaling law and the estimated domain thicknesses at 30 °C, the respective domain thicknesses at various temperatures were calculated. Peak reflectivity wavelengths at various temperatures were then obtained by TMM calculations as summarized in Table 5.4, in which the refractive indices of respective domains were assumed constant as the estimated values at 30 °C (i.e. $n_{\text{eff, PS}}$: 1.550, $n_{\text{eff, PI}}$: 1.502). Third, we considered the effects of both temperature-dependent refractive indices and temperature-dependent domain spacings. Using the values of the refractive indices and

domain spacings at various temperatures in Table 5.3 and 5.4, peak reflectivity wavelengths were calculated as summarized in Table 5.5.

Temperature (°C)	n_{PS}	n_{PI}	n_{cumene}	$n_{eff,PS}$	$n_{eff,PI}$	Peak reflectivity wavelength (nm)
30	1.590	1.510	1.491	1.550	1.502	510.5
40	1.589	1.509	1.485	1.547	1.499	509.5
50	1.587	1.507	1.480	1.544	1.496	508.5
60	1.586	1.506	1.474	1.541	1.493	507.5
70	1.585	1.505	1.468	1.538	1.490	506.5
80	1.584	1.504	1.463	1.535	1.487	505.5
90	1.582	1.502	1.457	1.532	1.484	504.5
100	1.581	1.501	1.451	1.529	1.481	503.5
110	1.580	1.500	1.446	1.526	1.478	502.5
120	1.579	1.499	1.440	1.523	1.475	501.5
130	1.578	1.497	1.434	1.520	1.472	500.5
140	1.576	1.496	1.429	1.517	1.469	499.5

Table 5.3: Effective refractive indices of PS and PI domains and peak reflectivity wavelengths at various temperatures obtained from TMM calculations, in which the domain spacings of the respective domains are held constant as the estimated values at 30 °C.

Temperature (°C)	$d_{\text{eff,PS}}$ (nm)	$d_{\text{eff,PI}}$ (nm)	Peak reflectivity wavelength (nm)
30	91.8	75.1	510.5
40	90.8	74.3	504.5
50	89.9	73.5	499.5
60	89.0	72.8	494.5
70	88.1	72.1	489.5
80	87.2	71.4	485.0
90	86.4	70.7	480.5
100	85.7	70.1	476.5
110	84.9	69.5	472.0
120	84.2	68.9	468.0
130	83.5	68.3	464.0
140	82.8	67.7	460.0

Table 5.4: Effective domain spacings of PS and PI domains and peak reflectivity wavelengths at various temperatures obtained from TMM calculations, in which the refractive indices of respective domains are held constant as the estimated values at 30 °C.

Temperature (°C)	$n_{\text{eff,PS}}$	$n_{\text{eff,PI}}$	$d_{\text{eff,PS}}$ (nm)	$d_{\text{eff,PI}}$ (nm)	Peak reflectivity wavelength (nm)
30	1.550	1.502	91.8	75.1	510.5
40	1.547	1.499	90.8	74.3	503.5
50	1.544	1.496	89.9	73.5	497.5
60	1.541	1.493	89.0	72.8	491.5
70	1.538	1.490	88.1	72.1	486.0
80	1.535	1.487	87.2	71.4	480.0
90	1.532	1.484	86.4	70.7	474.5
100	1.529	1.481	85.7	70.1	469.5
110	1.526	1.478	84.9	69.5	464.5
120	1.523	1.475	84.2	68.9	459.5
130	1.520	1.472	83.5	68.3	455.0
140	1.517	1.469	82.8	67.7	450.5

Table 5.5: Effective refractive indices, effective domain thicknesses of PS and PI domains, and peak reflectivity wavelengths at various temperatures obtained from TMM calculations.

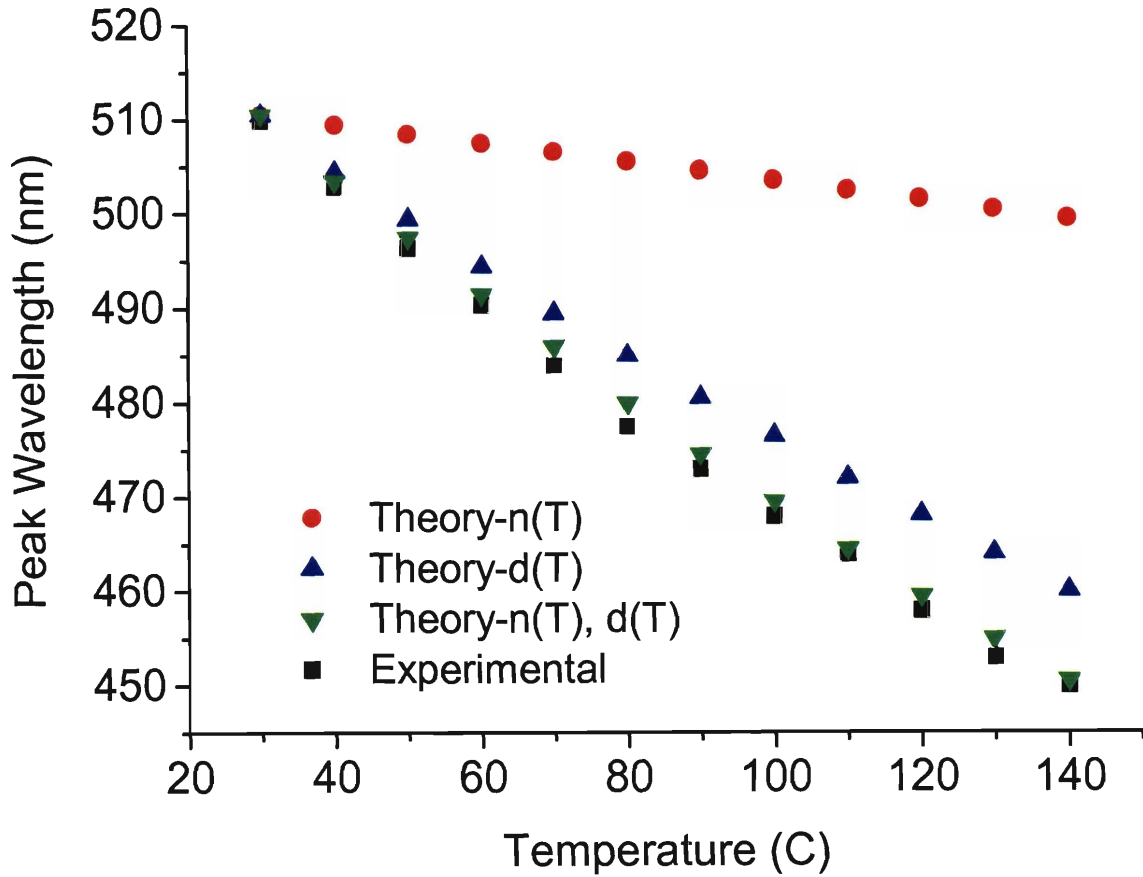


Figure 5.13: Peak reflectivity wavelengths obtained from TMM calculations with temperature-dependent refractive indices (red data points), with temperature-dependent domain thicknesses (blue data points), and with both temperature-dependent refractive indices and domain thicknesses at various temperatures. The observed peak reflectivity wavelengths (black data points) are also shown.

Figure 5.13 shows the calculated peak reflectivity wavelengths with temperature-dependent refractive indices (red data points), temperature-dependent domain thicknesses (blue data points), both temperature-dependent refractive indices and domain thicknesses

(green data points), and the observed peak reflectivity wavelength (black data points) as a function of temperature. As evidently shown in Figure 5.12, the change of refractive indices of polymer and solvent alone does not explain such a large shift of reflectivity band while the effect of domain thicknesses with temperature is dominant and produces the peak reflectivity positions close to the experimental values. If we consider both the effect of refractive indices and domain thicknesses, the match is excellent between experimental and theoretical peak reflectivity wavelengths at various temperatures. Therefore, the observed thermochromism from the self-assembled block copolymer reflector is a consequence of both the change of refractive indices and more importantly, the change of lamellar domain spacing induced by the variation of $\chi(T)$.

Finally, we investigated *mechanochromism*, or the effect of mechanical strain on reflectivity, of the block copolymer based photonic structure. For this study, an elastomeric gel has been prepared by blending the PS-b-PI block copolymer with a nonvolatile solvent, dioctyl phthalate (DOP, Aldrich) (~ 50/50 wt %), in order to lower the glass transition temperature of PS block and to make the sample a soft viscoelastic material at a room temperature. The mechanochromic gel was compressed between two glass substrates using spacers of various thickness and the normal incidence reflectivity has been measured by the microscope-spectrometer setup at different compressive strains. Figure 5.14 shows corresponding spectral measurements, a graph of measured peak reflectivity wavelength (blue data points) versus the compressed sample thickness. As the sample is compressed, the sample color changes from yellow-orange to green-blue as shown in the image insets in Figure 5.12.

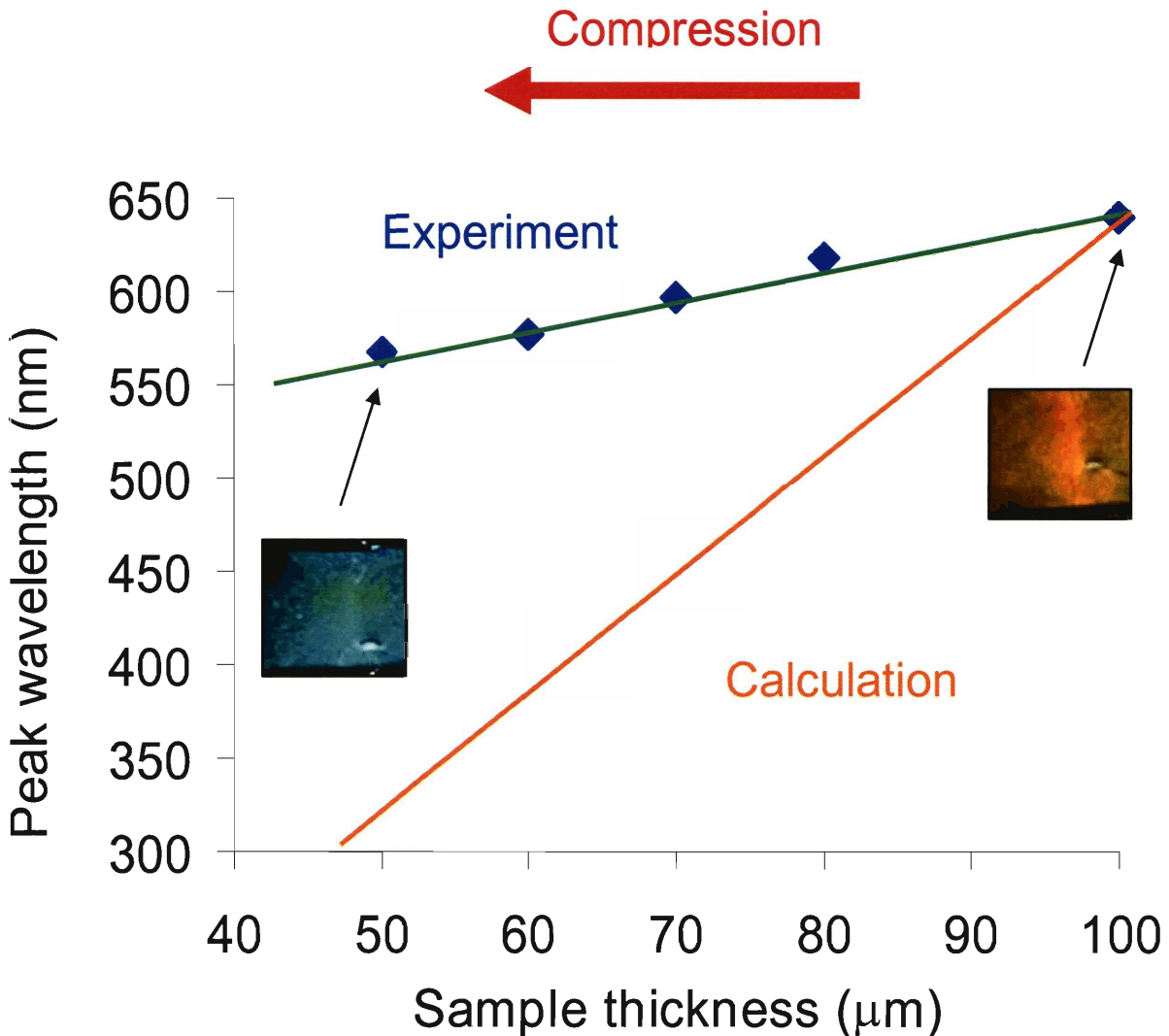


Figure 5.14: Measured peak reflectivity wavelength (blue data points) versus sample thickness of mechanochromic block copolymer gel. The orange line is obtained from the TMM calculation. Inset shows photographs taken from the sample at different sample thicknesses.

A simple explanation is the decrease of microdomain thickness due to the compression, which shifts the reflectivity band to shorter wavelengths. Given the initial reflectivity peak wavelength (640 nm) and the known solvent concentration (50%), we can

estimate the initial domain thickness of the PS and PI domains, again assuming a quarter-wave stack, parallel domain orientation, and uniform solvent distribution. If we further assume the macroscopic strain is the same as the microscopic strain of domains (i.e. affine deformation), we can calculate the reflectivity peak as a function of compressed sample thickness as shown in Figure 5.14 (orange line). We see that the change of the experimental peak reflectivity wavelength is much smaller than the values expected from the TMM calculation. Another possible effect of compression is the change of domain orientation. This reorientation effect not only makes the initially tilted lamellar domains more parallel to the substrates upon compression, which contributes to the red-shift of the bandgap center, but also makes the effective strain of respective domains less than the expected value based on the assumption of affine deformation. By crosslinking the PI domains, we also can achieve reversibility of mechanochromic response of block copolymer photonic gels (data not include here).

5.3. Conclusion

In summary, stimulus responsive tunable self-assembled reflectors have been demonstrated using block copolymer based one-dimensional (1D) photonic crystals. Solvent, temperature, and compressive mechanical strain have been applied to modulate microstructural and material properties of block copolymer gels, resulting in effective tuning of the spectral response of the system. The decreased lamellar domain spacing (due

to the decreased segregation strength between PS and PI blocks) and the decreased refractive index contrast with increasing solvent concentration resulted in a peak narrowing and a blue-shift of the photonic stop band of the solvatochromic reflector. The observed thermochromism from the self-assembled block copolymer reflector was induced by both the temperature-dependent refractive indices and more importantly, the temperature-dependent domain spacings with the variation of $\chi(T)$. The mechanochromic effect of the block copolymer photonic gel can be understood by considering the variation of domain thickness and domain orientation under the applied compressive strain. These stimulus responsive tunable self-assembled reflectors can be potentially used for novel sensor and display applications.

5.4. References

1. Yablonovitch, E. "Inhibited Spontaneous Emission in Solid-State Physics and Electronics" *Physical Review Letters* **1987**, 58, 2059-2062.
2. John, S. "Strong Localization of Photons in Certain Disordered Dielectric Superlattices" *Physical Review Letters* **1987**, 58, 2486-2489.
3. Cao, W. Y.; Munoz, A.; Palffy-Muhoray, P.; Taheri, B. "Lasing in a three-dimensional photonic crystal of the liquid crystal blue phase II" *Nature Materials* **2002**, 1, 111-113.
4. Qi, M. H.; Lidorikis, E.; Rakich, P. T.; Johnson, S. G.; Joannopoulos, J. D.; Ippen, E. P.; Smith, H. I. "A three-dimensional optical photonic crystal with designed point defects" *Nature* **2004**, 429, 538-542.
5. Busch, K.; John, S. "Liquid-crystal photonic-band-gap materials: The tunable electromagnetic vacuum" *Physical Review Letters* **1999**, 83, 967-970.
6. Finkelmann, H.; Kim, S. T.; Munoz, A.; Palffy-Muhoray, P.; Taheri, B. "Tunable mirrorless lasing in cholesteric liquid crystalline elastomers" *Advanced Materials* **2001**, 13, 1069-1072.
7. Foulger, S. H.; Jiang, P.; Lattam, A.; Smith, D. W.; Ballato, J.; Dausch, D. E.; Grego, S.; Stoner, B. R. "Photonic crystal composites with reversible high-frequency stop band shifts" *Advanced Materials* **2003**, 15, 685-689.
8. Lee, Y. J.; Braun, P. V. "Tunable inverse opal hydrogel pH sensors" *Advanced Materials* **2003**, 15, 563-566.

9. Ozaki, R.; Matsui, T.; Ozaki, M.; Yoshino, K. "Electrically color-tunable defect mode lasing in one-dimensional photonic-band-gap system containing liquid crystal" *Applied Physics Letters* **2003**, 82, 3593-3595.
10. Valkama, S.; Kosonen, H.; Ruokolainen, J.; Haatainen, T.; Torkkeli, M.; Serimaa, R.; Ten Brinke, G.; Ikkala, O. "Self-assembled polymeric solid films with temperature-induced large and reversible photonic-bandgap switching" *Nature Materials* **2004**, 3, 872-876.
11. Lawrence, J. R.; Shim, G. H.; Jiang, P.; Han, M. G.; Ying, Y. R.; Foulger, S. H. "Dynamic tuning of photoluminescent dyes in crystalline colloidal arrays" *Advanced Materials* **2005**, 17, 2344-+.
12. Arsenault, A. C.; Clark, T. J.; von Freymann, G.; Cademartiri, L.; Sapienza, R.; Bertolotti, J.; Vekris, E.; Wong, S.; Kitaev, V.; Manners, I.; Wang, R. Z.; John, S.; Wiersma, D.; Ozin, G. A. "From colour fingerprinting to the control of photoluminescence in elastic photonic crystals" *Nature Materials* **2006**, 5, 179-184.
13. Holtz, J. H.; Asher, S. A. "Polymerized colloidal crystal hydrogel films as intelligent chemical sensing materials" *Nature* **1997**, 389, 829-832.
14. Holmstrom, S. A.; Natarajan, L. V.; Tondiglia, V. P.; Sutherland, R. L.; Bunning, T. J. "Mechanical tuning of holographic polymer-dispersed liquid crystal reflection gratings" *Applied Physics Letters* **2004**, 85, 1949-1951.
15. Yoon, J.; Lee, W.; Thomas, E. L. "Self-assembly of block copolymers for photonic-bandgap materials" *MRS Bulletin* **2005**, 30, 721-726.
16. Urbas, A.; Sharp, R.; Fink, Y.; Thomas, E. L.; Xenidou, M.; Fetters, L. J. "Tunable

- block copolymer/homopolymer photonic crystals" *Advanced Materials* **2000**, 12, 812-814.
17. Fink, Y.; Urbas, A. M.; Bawendi, M. G.; Joannopoulos, J. D.; Thomas, E. L. "Block copolymers as photonic bandgap materials" *Journal of Lightwave Technology* **1999**, 17, 1963-1969.
 18. Bockstaller, M.; Kolb, R.; Thomas, E. L. "Metallodielectric photonic crystals based on diblock copolymers" *Advanced Materials* **2001**, 13, 1783-1786.
 19. Osuji, C.; Chao, C. Y.; Bitá, I.; Ober, C. K.; Thomas, E. L. "Temperature-dependent photonic bandgap in a self-assembled hydrogen-bonded liquid-crystalline diblock copolymer" *Advanced Functional Materials* **2002**, 12, 753-758.
 20. Born, M.; Wolf, E., *Principles of Optics*. 7th ed.; Cambridge University Press: Cambridge, 1999.
 21. Joannopoulos, J. D.; Meade, R. D.; Winn, J. N., *Photonic Crystals: Molding the Flow of Light*. Princeton University Press: Princeton, 1995.
 22. Fink, Y. *Polymeric Photonic Crystals. Ph.D. Thesis*, Massachusetts Institute of Technology, Cambridge, 2000.
 23. Hashimoto, T.; Nagatosh, K.; Todo, A.; Hasegawa, H.; Kawai, H. "Domain-Boundary Structure of Styrene-Isoprene Block Copolymer Films Cast From Toluene Solutions" *Macromolecules* **1974**, 7, 364-373.
 24. Hashimoto, T.; Todo, A.; Itoi, H.; Kawai, H. "Domain-Boundary Structure of Styrene-Isoprene Block Copolymer Films Cast From Solutions.2. Quantitative Estimation of Interfacial Thickness of Lamellar Microphase Systems"

- Macromolecules* **1977**, 10, 377-384.
25. Shibayama, M.; Hashimoto, T.; Hasegawa, H.; Kawai, H. "Ordered Structure in Block Polymer-Solutions.3. Concentration-Dependence of Microdomains In Non-Selective Solvents" *Macromolecules* **1983**, 16, 1427-1433.
 26. Shibayama, M.; Hashimoto, T.; Kawai, H. "Ordered Structure in Block Polymer-Solutions.5. Equilibrium and Non-Equilibrium Aspects of Microdomain Formation" *Macromolecules* **1983**, 16, 1434-1443.
 27. Hashimoto, T.; Shibayama, M.; Kawai, H. "Ordered Structure In Block Polymer-Solutions.4. Scaling Rules on Size of Fluctuations with Block Molecular-Weight, Concentration, and Temperature in Segregation and Homogeneous Regimes" *Macromolecules* **1983**, 16, 1093-1101.
 28. El-Kashef, H. "Thermo-optical and dielectric constants of laser dye solvents" *Review of Scientific Instruments* **1998**, 69, 1243-1245.
 29. Brandrup, J.; Immergut, E. H.; Grulke, E. A., *Polymer Handbook*. 4 ed.; Wiley-Interscience: 1999.

Chapter 6.

Highly Oriented Thin Film Microdomain Patterns of Ultrahigh Molecular Weight Photonic Block Copolymers via Directional Solidification of a Solvent

In this chapter we present excellent control of thin film microdomain orientation of lamellar- and cylinder-forming ultrahigh molecular weight block copolymers ($M_n \sim 10^6$ g/mol) over a large area via directional solidification of a crystallizable solvent. Moreover, we found an intriguing ordering behavior of the ultrahigh molecular weight block copolymers, which is dramatically different from that of typical molecular weight block copolymers ($M_n \sim 5 \times 10^4$ g/mol), as revealed by 3D optical imaging via laser scanning confocal microscopy (LSCM). These highly oriented thin film microdomain patterns have a domain size on the order of wavelength of visible light and can potentially be used for creating useful thin film photonic structures.

The LSCM investigation was in collaboration with Dr. Wonmok Lee and parts of this chapter will appear in: J. Yoon, W. Lee, E. L. Thomas *Advanced Materials* (submitted).

6.1. Introduction

Self-assembly is rapidly emerging as a simple and effective method for creating large-area functional periodic structures in various nanotechnologies.²⁻⁴ In particular, block copolymers have been considered as a promising self-organizing material platform because of their tunability in shape, size, and physical/chemical properties of the domains, with the capability of hosting many types of nano-additives for desirable multifunctional composites.⁵ In order to fulfill the potential of these materials, it is necessary to control microdomain orientation and long-range translational order, as well as to prevent randomly occurring defects. Considerable research into developing well-ordered block copolymer nanostructures has been undertaken with the common strategy of using various external biases such as mechanical flow fields,⁶⁻⁹ temperature gradient,¹⁰ electric fields,¹¹ solvent annealing,¹² and topological and/or chemical patterns^{13,14} during the self-assembly process. Directional solidification (DS) is a thin film process that can generate highly-ordered nanoscale patterns of block copolymers, in which the block copolymer solute rapidly solidifies from a mixture with a crystallizable organic solvent, as the organic solvent undergoes directional crystallization. A range of block copolymer systems having both cylindrical and lamellar microdomains with typical molecular weights of $\sim 5 \times 10^4$ g/mol have been successfully organized in thin films with this fast ordering process.¹⁵⁻¹⁷

Recently, ultrahigh molecular weight ($M_n \sim 10^6$ g/mol) block copolymers possessing a domain size comparable to the wavelength of visible light have received increasing attention as self-assembled photonic materials.¹⁸ One-, two-, and three-dimensional

photonic crystals for visible frequencies have been successfully demonstrated using lamellar, cylindrical, and double gyroid morphologies of poly(styrene-*b*-isoprene) (PS-*b*-PI) block copolymers.¹⁹⁻²¹ While most of previous work on these photonic block copolymers has been limited to relatively thick samples with only modest control over microdomain order, numerous engineering applications such as thin film waveguides, reflectors, and microcavities for lasing can potentially be achieved from controlled nanostructured thin films of these materials, all of which depend critically on the overall order of the microdomains to meet desired functionalities.

Here we demonstrate the excellent control of thin film microdomain patterns of lamellar- and cylinder-forming ultrahigh molecular weight block copolymers (~ 20 times larger molecular weight than for previously studied block copolymers) over a large area via directional solidification of a solvent. The ordering behavior of these photonic block copolymers via the DS process is dramatically different from that of directionally solidified conventional molecular weight BCPs. Due to the relatively large domain sizes of ultrahigh molecular weight BCPs, laser scanning confocal microscopy (LSCM) could be used to optically characterize the lamellar and cylindrical thin film structures in 3D.

6.2. Results and Discussion

The ultrahigh molecular weight PS-*b*-PI diblock copolymers having lamellar and cylindrical morphologies were anionically synthesized by sequential addition of styrene and

isoprene monomer in cyclohexane/benzene mixed solvent.²² Molecular weights and compositions of the block copolymers are 8.4×10^5 g/mol (PDI: 1.08), 57/43 (PS/PI, wt/wt) for the lamellar-forming block copolymer (SI_{LAM}) and 1.15×10^6 g/mol (PDI: 1.05), 22/78 (PS/PI, wt/wt) for the cylinder-forming block copolymer (SI_{CYL}) as determined by gel permeation chromatography (GPC) and nuclear magnetic resonance (NMR) analysis. In order to prepare highly oriented block copolymer samples in thin films, the directional solidification method with benzoic acid (BA) was applied as described in previous studies.^{15, 16} Once the sample cooled down to a room temperature, it was analyzed by reflection-mode LSCM (Leica TCS SPII) using a 488 nm probe laser beam without further treatment. Since the PS-b-PI BCP does not contain any fluorophore, reflection signals of the probe light were scanned for every LSCM image through an oil-immersion objective lens (Leica, HCX PL APO 63X/1.40-0.60).

The directional solidification of block copolymers with BA resulted in orientational control of the self-assembled microdomains over a large area ($\sim 100 \times 100 \mu\text{m}^2$), as shown in the reflection-mode LSCM micrographs. Figure 6.1 shows the highly oriented lamellar microdomains of SI_{LAM} with the lamellar microdomains oriented such that their intermaterial dividing surfaces (IMDSs) are approximately perpendicular to the fast-growth direction of the BA crystal (\mathbf{b}_{BA} , i.e. the crystallographic b-axis of BA crystal). Directional solidification of SI_{CYL} also created well-ordered cylindrical microdomains in a thin film as shown in Figure 6.2, where the PS cylindrical domains are lying in the xy-plane and the cylinder axes are perpendicular to \mathbf{b}_{BA} . The relative microdomain orientation with respect to the BA growth direction was determined from low magnification LSCM images, where

the fast-growth direction of BA crystal was readily identified. For example, Figure 6.3 shows a low magnification LSCM image of SI_{CYL} in which a long and narrow region represents the highly ordered cylindrical domains aligned normal to the fast-growth direction of BA.

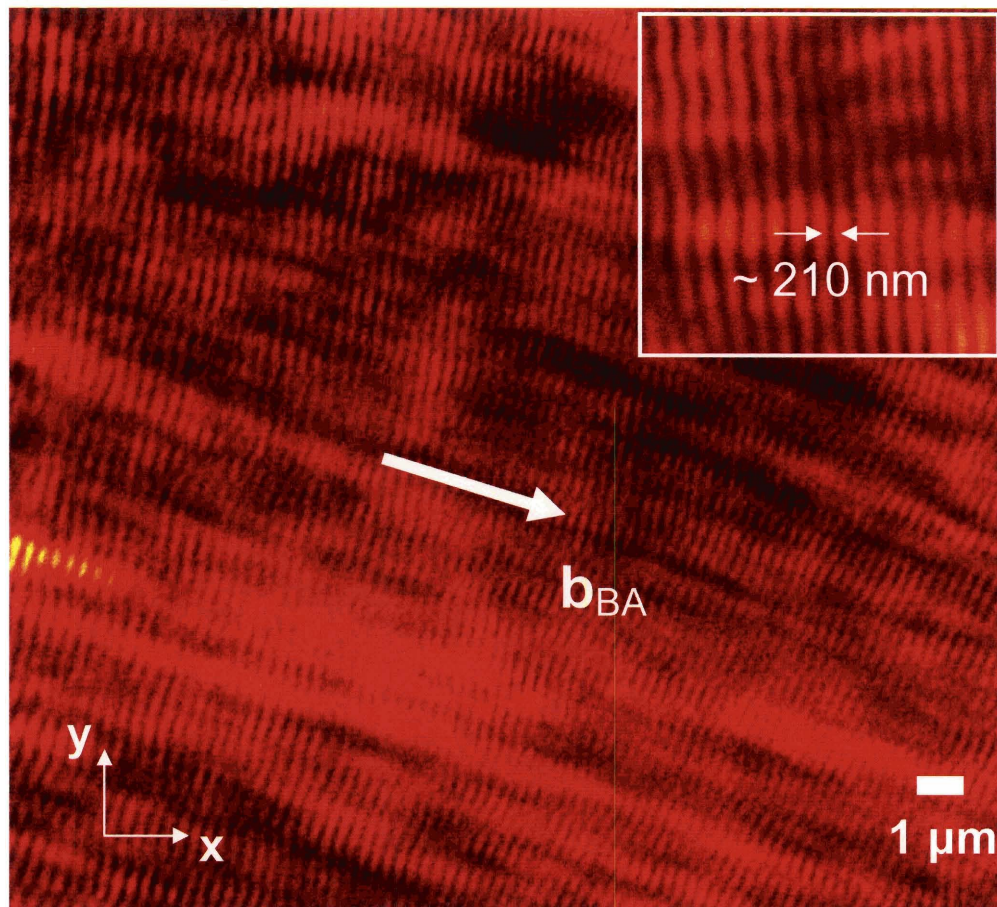


Figure 6.1: Reflection mode LSCM image (xy-scan) of PS-b-PI block copolymers showing highly-oriented lamellar microdomains in a thin film obtained from directional solidification process with benzoic acid (BA). Inter-material dividing surfaces (IMDSs) are principally aligned perpendicular to the fast growing direction of benzoic acid (the b-axis of BA crystal). The inset is a high magnification image of the edge-on lamellae, for which the lamellar periodicity ($d_{LAM} \sim 210$ nm) is shown.

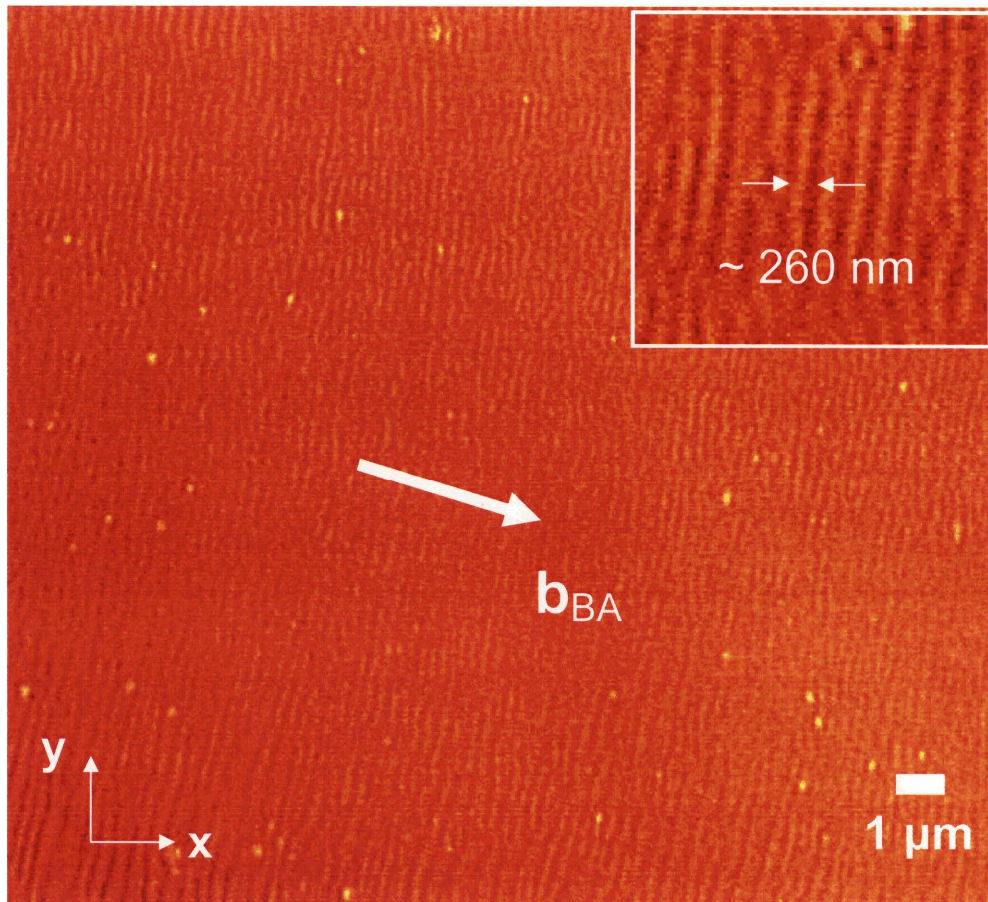


Figure 6.2: Reflection mode LSCM image (xy-scan) of PS-b-PI block copolymers showing highly-oriented cylindrical microdomains in a thin film obtained from directional solidification process with benzoic acid (BA). Inter-material dividing surfaces (IMDSs) are principally aligned perpendicular to the fast growing direction of benzoic acid (the b-axis of BA crystal) The inset is a high magnification image of the in-plane cylinders, for which the inter-cylinder spacing ($d_{\text{CYL}} \sim 260$ nm) is shown.

To further explore the block copolymer thin film nanostructure, a series of LSCM xy-images were taken varying the z position (i.e. an image slice (focal plane) along the film thickness direction) to permit 3D image reconstruction. Figure 6.4 and 6.5 show the 3D

LSCM representations of the SI_{LAM} and SI_{CYL} thin films and corresponding schematics. Interestingly, the lamellar microdomains are tilted by about 60° to \mathbf{b}_{BA} as shown in Figure 6.4. 3D imaging of the SI_{CYL} thin film revealed that it is composed of approximately four layers of hexagonally packed PS cylinders in the film thickness direction as shown in Figure 6.5. From the side view of SI_{CYL} thin film (yz -plane), the second and fourth layers of cylinders appear brighter since the first and third layers of cylinders are offset from the focal plane. The elongated shape of the cylindrical cross-section in the xz -plane can be attributed to the limited axial resolution of LSCM.^{23, 24} The hexagonal packing of cylindrical domains in the xz -plane was also confirmed by xy -scans of the film in varying z -locations, which clearly shows alternating registration of cylindrical domains at different depths as shown in Figure 6.6.

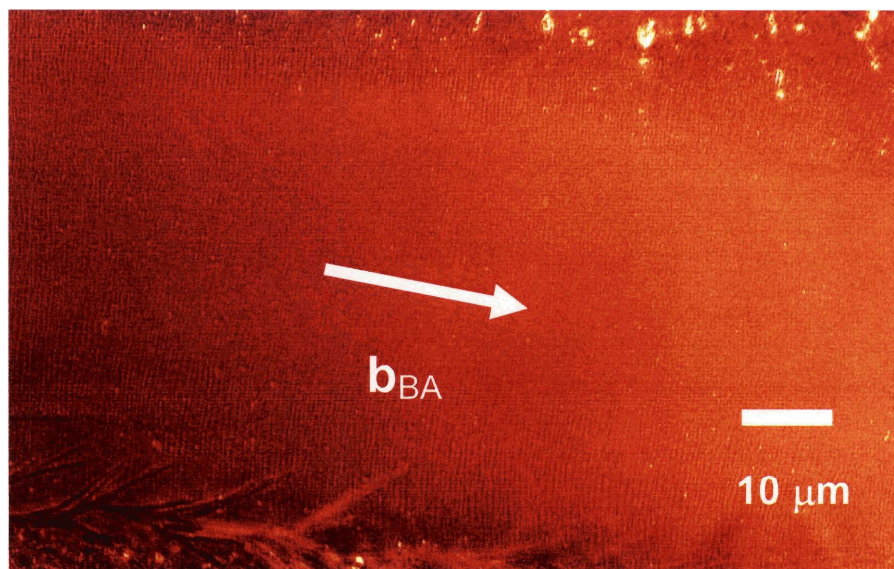


Figure 6.3: A low magnification LSCM image (xy -scan) of SI_{CYL} showing the relative orientation of cylindrical microdomains with respect to the fast-growth direction of BA crystal.

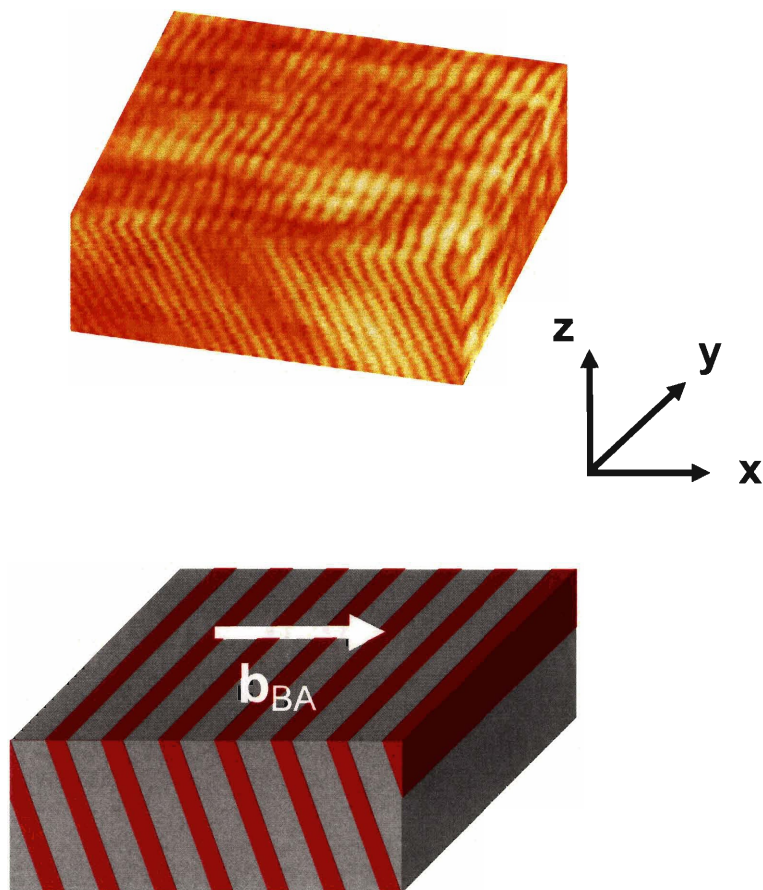


Figure 6.4: 3D reconstruction of reflection mode LSCM image of a highly-ordered lamellar PS-b-PI block copolymer in a thin film obtained from the DS process. 3D imaging revealed that lamellae were tilted by about 60° to the fast-growth direction of BA. Corresponding schematic with the direction of BA crystallization is also shown.

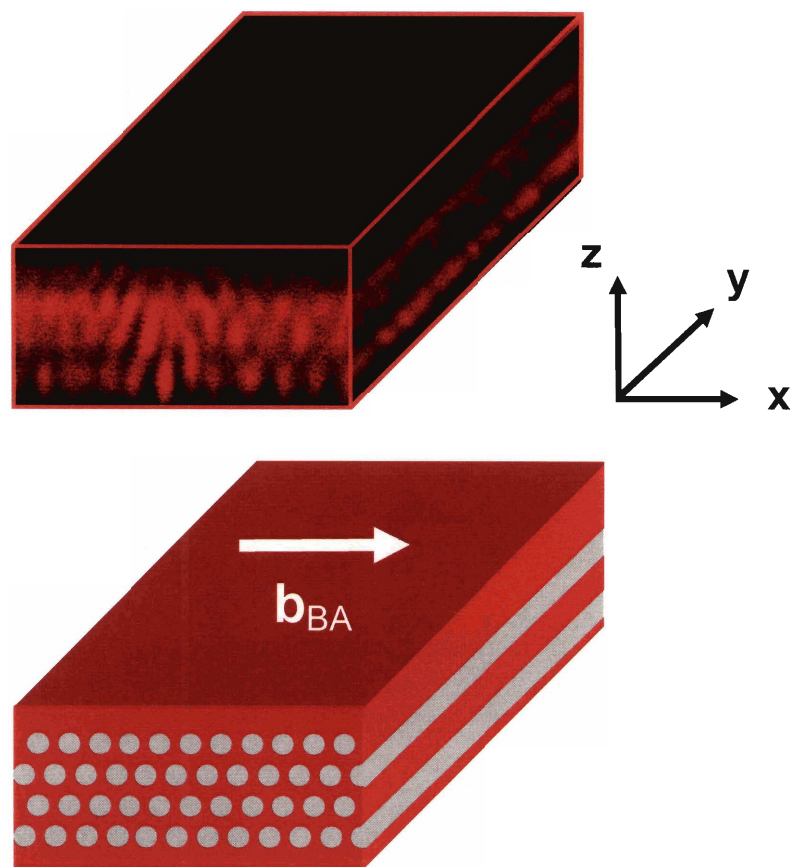


Figure 6.5: 3D reconstruction of reflection mode LSCM image of a highly-ordered cylindrical PS-b-PI block copolymer in a thin film obtained from the DS process. 3D imaging revealed cylindrical microdomains were hexagonally packed in the xz -plane. Corresponding schematic with the direction of BA crystallization is also shown.

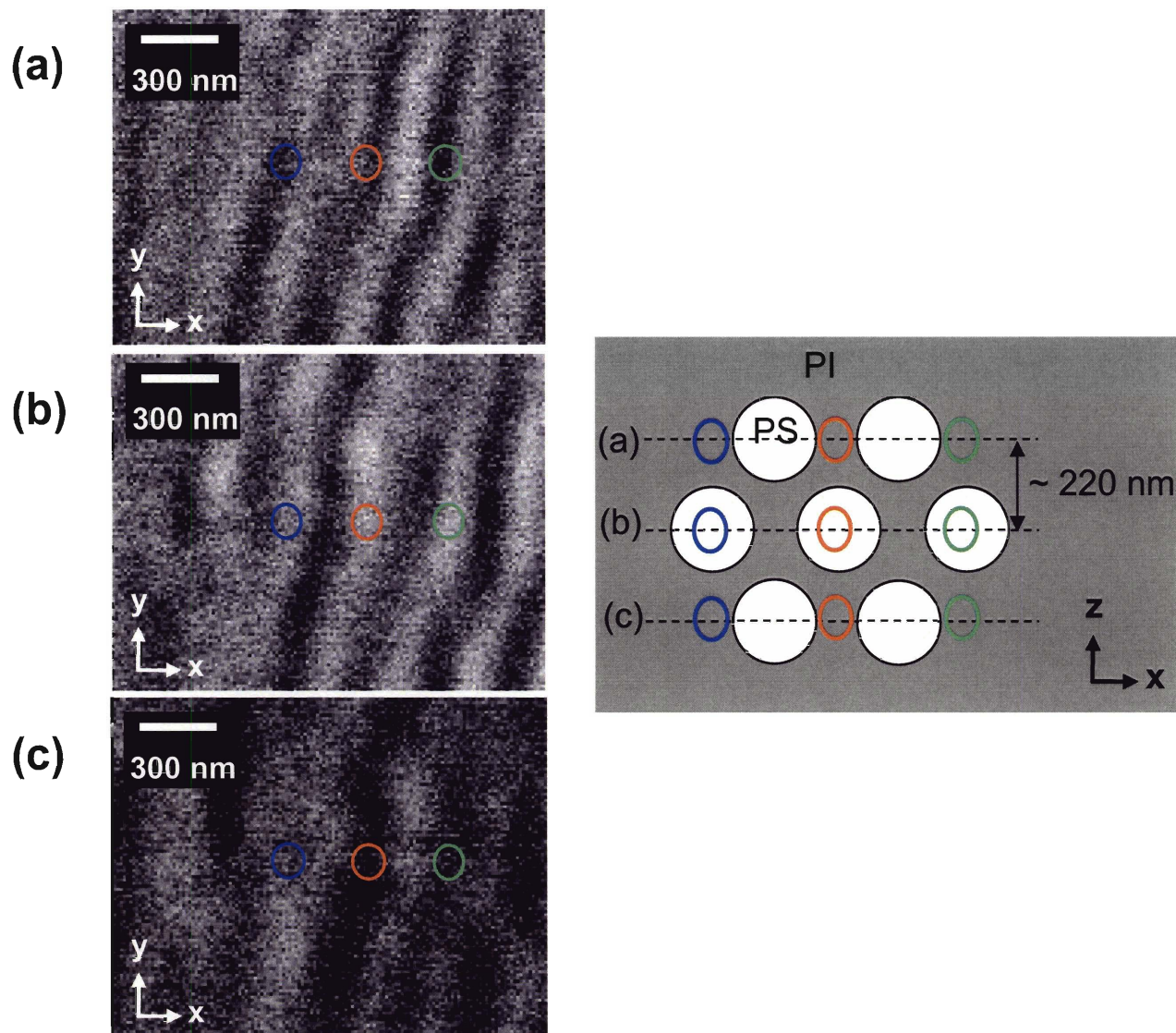


Figure 6.6: Reflection-mode LSCM images (xy -scan) of PS- b -PI block copolymer (SI_{CYL}) taken every 220 nm along the z -axis on the same sample position. In each figure, three circled regions show the alternating registration of PS cylindrical domains (bright region) in PI matrix (dark region) along the z axis.

An intriguing phenomenon in the DS process found in this study is the molecular weight dependence of the block copolymer microdomain orientation with respect to the fast-growth direction of BA. According to our previous studies using conventional molecular weight lamellar and cylindrical block copolymers ($M_n \sim 5 \times 10^4$ g/mol), the IMDSs are predominantly oriented parallel to \mathbf{b}_{BA} , that is, the lamellar normal was aligned perpendicular to \mathbf{b}_{BA} and the cylinder axis was aligned parallel to \mathbf{b}_{BA} .^{5,16} However, with the present 20 times higher molecular weight block copolymers, the microdomain orientations change by about 90°.

In the DS process, the symmetry breaking external field inducing the microdomain orientation is a concentration gradient of the BCP molecules generated by a directional crystallization of the BA solvent. Figure 6.7 shows hypothetical schematic diagrams of the block copolymer concentration profiles during the DS process along the fast-growth direction (\mathbf{b}_{BA}) of BA for (a) high and (b) low molecular weight block copolymers, in which the y-axis is the concentration (ϕ) of dissolved block copolymers and the x-axis is the spatial coordinate along \mathbf{b}_{BA} . Above the melting temperature of BA ($T_{m,BA} \sim 123$ °C), the solution of block copolymers in BA is a homogeneous liquid and the dissolved block copolymer chains are in a disordered state below the order-disorder transition concentration (ϕ_{ODC}). When the temperature is dropped down below the $T_{m,BA}$, directional growth of BA crystals is initiated and simultaneously the block copolymer concentration in the remaining liquid increases with directional extraction of solvent along the fast-growth direction of the solvent crystal. As the directional crystallization of BA proceeds further, the block copolymer concentration also increases and eventually reaches the ϕ_{ODC} , at which

microphase separation of the block copolymer domains is initiated. After the onset of microphase separation at the phase separation boundary, the block copolymer concentration continues to increase and reaches the value of pure block copolymer ($\phi=1.0$) as the remaining BA molecules diffuse out of the polymer, and crystallize onto the essentially pure BA domains.

The molecular weight dependent microdomain orientation in the DS process can be understood in terms of a combination of the following three physical factors: (i) the order-disorder transition concentration (ϕ_{ODC}) (ii) the diffusivity of block copolymer molecules in solution and (iii) the solubility of PS and PI block with respect to BA. All of these factors have a strong molecular weight dependence and may play important roles during the course of microphase separation. Scaling laws for semi-dilute solutions suggest that the order-disorder transition of A-B diblock copolymer varies as: $\phi_{\text{ODC}} \sim (\chi N)^{-1/1.59}$, where χ is the Flory-Huggins interaction parameter, and N is the total degree of polymerization.^{25, 26} Thus, ϕ_{ODC} scales as $N^{0.62}$ at a fixed temperature. The order-disorder transitions for the present high molecular weight block copolymer systems therefore occur at much lower concentrations than that for the low molecular weight block copolymers due to the factor 20 increase in the block copolymer molecular weight. As mentioned earlier, while a solvent (BA) crystallizes in the DS process, the directional extraction of the solvent generates a concentration gradient (i.e. $d\phi/dx$ in Figure 6.7) along the solidification direction. Assuming that the growth velocity of BA crystals and the resulting concentration profile are the same for high and low molecular weight block copolymers, then the order-disorder concentration of high molecular weight block copolymer is reached much faster and the block copolymer

microphase separation front (vertical line β in Figure 6.7(a)) is much closer to the BA crystallization front (vertical line α in Figure 6.7(a)) than for low molecular weight block copolymers (Figure 6.7(b)).

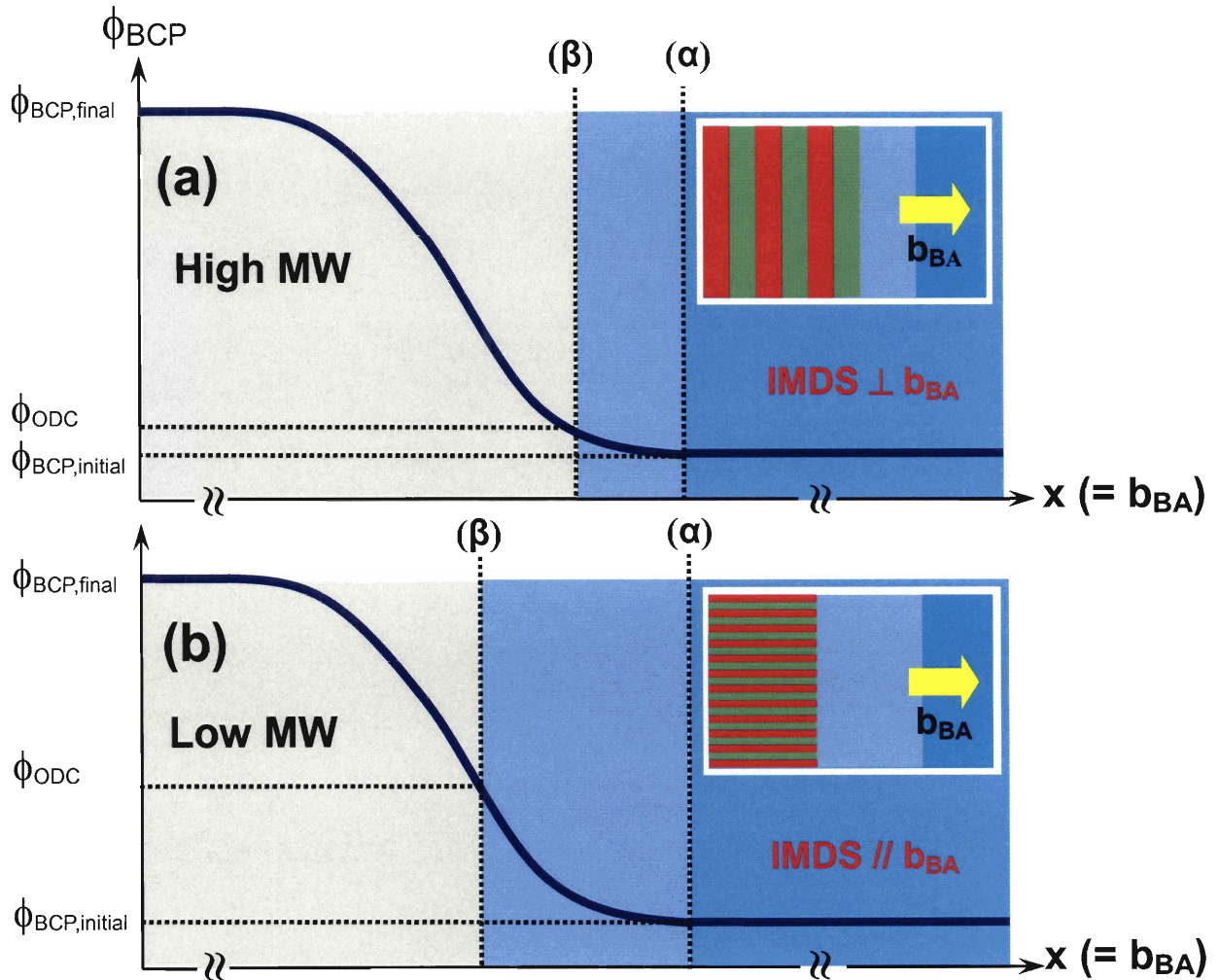


Figure 6.7: Schematic diagrams showing the hypothetical concentration profiles of block copolymer (ϕ_{BCP}) along b_{BA} , the fast-growth direction of benzoic acid (BA) crystal during the DS process for (a) high and (b) low molecular weight block copolymer samples. The dotted lines represent BA crystallization front (α) and block copolymer microphase separation front (β). The insets show respective schematics of corresponding microdomain orientations with respect to b_{BA} induced during the DS process.

The diffusion coefficient also strongly depends on the molecular weight. According to scaling laws for block copolymer solutions, the diffusion coefficient (D) of block copolymer in solution scales as $N^{-0.85}$ (in semidilute regime with an athermal solvent),²⁷ and hence the high molecular weight block copolymers in the present study should have much lower diffusion coefficient than the previously studied low molecular weight block copolymers. During microphase separation, the system will tend to minimize the interfacial free energy at the phase separation front. As the ordered block copolymer phase grows, the increment of interfacial free energy per unit growth is minimized if the interface between different phases grows perpendicular to the phase separation front. The previous results obtained from the relatively low molecular weight block copolymers correspond to this case, in which the IMDSs are aligned perpendicular to the phase separation front (or parallel to \mathbf{b}_{BA}). On the other hand, if a block copolymer has sufficiently high molecular weight and thus has a rather low diffusion coefficient, the microphase separation is essentially a diffusion-controlled process and the block copolymer molecules can not adopt the morphology of minimum interfacial energy due to kinetic limitations. The order-disorder transition which occurs relatively sooner as a result of the relatively lower value of the ϕ_{ODC} in the high molecular weight case also contributes to this diffusion-controlled process for high molecular weight block copolymer samples.

Another physical factor which may influence the ordering behavior in the DS process is the solubility of PS-*b*-PI block copolymer in BA. The PS monomeric repeat should have a higher solubility in BA than the PI unit due to the similar chemical structure between styrene and benzoic acid. In block copolymer solution, the solubility of each block

strongly depends on its molecular weight and its solubility parameter with respect to a solvent. As the concentration of high molecular weight block copolymer increases with the crystallization of BA, the PI block, which has a poorer solubility in BA, reaches the solubility limit in BA faster than the PS block. If this is the case, we can envision that under the diffusion-controlled process for high molecular weight block copolymers, the PI block tends to phase separate first and PS block follows, which produces the ordered structures where the IMDSs are aligned perpendicular to the fast-growth direction of BA crystal. Such perpendicularly ordered IMDSs with respect to microphase growth direction were also previously observed in surface-induced microphase separation of a block copolymer melt in a temperature gradient^{10, 28}, and blends in a concentration gradient²⁹, where the phase separation of one block is initiated due to the preferential wetting of the block to substrate and the microphase separation of the other block follows along the direction of the field gradient, resulting in the perpendicularly oriented domains.

6.3. Conclusion

In summary, highly oriented thin film microdomain patterns of ultrahigh molecular weight block copolymers having lamellar and cylindrical morphologies have been successfully created over a large area via directional solidification of a solvent. These interesting ordered textures of ultrahigh molecular weight block copolymers were characterized by means of 3D optical LSCM imaging. The dramatic difference in the

microdomain orientation obtained from ultrahigh molecular weight block copolymers vs. low molecular weight block copolymers can be understood by diffusion- and solubility-controlled microphase separation of block copolymers in solution during the directional extraction of the crystallizable solvent. These ultrahigh molecular weight block copolymer patterns have a domain size comparable to visible wavelengths and can be potentially used for fabricating useful thin film photonic structures.^{18, 22}

6.4. References

1. Lee, W.; Yoon, J.; Lee, H.; Thomas, E. L. "Direct three-dimensional imaging of block copolymer nanostructures using laser scanning confocal microscopy" *in preparation* **2006**.
2. Huang, Y.; Chiang, C.-Y.; Lee, S. K.; Gao, Y.; Hu, E. L.; De Yoreo, J.; Belcher, A. M. "Programmable Assembly of Nanoarchitectures Using Genetically Engineered Viruses" *Nano Letters* **2005**, 5, 1429-1434.
3. Jiang, P.; Bertone, J. F.; Colvin, V. L. "A lost-wax approach to monodisperse colloids and their crystals" *Science* **2001**, 291, 453-457.
4. Stoykovich, M. P.; Mueller, M.; Kim, S. O.; Solak, H. H.; Edwards, E. W.; de Pablo, J. J.; Nealey, P. F. "Directed assembly of block copolymer blends into nonregular device-oriented structures" *Science* **2005**, 308, 1442-1446.
5. Park, C.; Yoon, J.; Thomas, E. L. "Enabling nanotechnology with self assembled block copolymer patterns" *Polymer* **2003**, 44, 6725-6760.
6. Chen, Z. R.; Kornfield, J. A.; Smith, S. D.; Grothaus, J. T.; Satkowski, M. M. "Pathways to macroscale order in nanostructured block copolymers" *Science* **1997**, 277, 1248-1253.
7. Albalak, R. J.; Capel, M. S.; Thomas, E. L. "Solvent swelling of roll-cast triblock copolymer films" *Polymer* **1998**, 39, 1647-1656.
8. Hamley, I. W. "Structure and flow behaviour of block copolymers" *Journal of Physics-Condensed Matter* **2001**, 13, R643-R671.

9. Angelescu, D. E.; Waller, J. H.; Register, R. A.; Chaikin, P. M. "Shear-induced alignment in thin films of spherical nanodomains" *Advanced Materials* **2005**, *17*, 1878-1881.
10. Hashimoto, T.; Bodycomb, J.; Funaki, Y.; Kimishima, K. "The Effect of Temperature Gradient on the Microdomain Orientation of Diblock Copolymers Undergoing an Order-Disorder Transition" *Macromolecules* **1999**, *32*, 952-954.
11. Thurn-Albrecht, T.; Schotter, J.; Kastle, C. A.; Emley, N.; Shibauchi, T.; Krusin-Elbaum, L.; Guarini, K.; Black, C. T.; Tuominen, M. T.; Russell, T. P. "Ultra-high-density nanowire arrays grown in self-assembled diblock copolymer templates" *Science* **2000**, *290*, 2126-2129.
12. Kim, S. H.; Misner, M. J.; Russell, T. P. "Solvent-induced ordering in thin film diblock copolymer/homopolymer mixtures" *Advanced Materials* **2004**, *16*, 2119-2123.
13. Segalman, R. A.; Yokoyama, H.; Kramer, E. J. "Graphoepitaxy of spherical domain block copolymer films" *Advanced Materials* **2001**, *13*, 1152-1155.
14. Kim, S. O.; Solak, H. H.; Stoykovich, M. P.; Ferrier, N. J.; de Pablo, J. J.; Nealey, P. F. "Epitaxial self-assembly of block copolymers on lithographically defined nanopatterned substrates" *Nature* **2003**, *424*, 411-414.
15. De Rosa, C.; Park, C.; Thomas, E. L.; Lotz, B. "Microdomain patterns from directional eutectic solidification and epitaxy" *Nature* **2000**, *405*, 433-437.
16. Park, C.; De Rosa, C.; Thomas, E. L. "Large Area Orientation of Block Copolymer Microdomains in Thin Films via Directional Crystallization of a Solvent"

- Macromolecules* **2001**, 34, 2602-2606.
17. Park, C.; De Rosa, C.; Fetters, L. J.; Lotz, B.; Thomas, E. L. "Alteration of classical microdomain patterns of block copolymers by degenerate epitaxy" *Advanced Materials* **2001**, 13, 724-728.
 18. Yoon, J.; Lee, W.; Thomas, E. L. "Self-assembly of block copolymers for photonic-bandgap materials" *MRS Bulletin* **2005**, 30, 721-726.
 19. Urbas, A.; Fink, Y.; Thomas, E. L. "One-dimensionally periodic dielectric reflectors from self-assembled block copolymer-homopolymer blends" *Macromolecules* **1999**, 32, 4748-4750.
 20. Deng, T.; Chen, C.; Honeker, C.; Thomas, E. L. "Two-dimensional block copolymer photonic crystals" *Polymer* **2003**, 44, 6549-6553.
 21. Urbas, A. M.; Maldovan, M.; DeRege, P.; Thomas, E. L. "Bicontinuous cubic block copolymer photonic crystals" *Advanced Materials* **2002**, 14, 1850-1853.
 22. Edrington, A. C.; Urbas, A. M.; DeRege, P.; Chen, C. X.; Swager, T. M.; Hadjichristidis, N.; Xenidou, M.; Fetters, L. J.; Joannopoulos, J. D.; Fink, Y.; Thomas, E. L. "Polymer-based photonic crystals" *Advanced Materials* **2001**, 13, 421-425.
 23. Halhuber, K. J.; Konig, K. "Modern laser scanning microscopy in biology, biotechnology and medicine" *Annals of Anatomy-Anatomischer Anzeiger* **2003**, 185, 1-20.
 24. Wilson, T.; Sheppard, C. J. R. "*Theory and Practice of Scanning Optical Microscopy* (Academic, New York, 1984).

25. Joanny, J. F.; Leibler, L.; Ball, R. "Is Chemical Mismatch Important In Polymer-Solutions" *Journal of Chemical Physics* **1984**, 81, 4640-4656.
26. Broseta, D.; Leibler, L.; Joanny, J. F. "Critical Properties of Incompatible Polymer Blends Dissolved In A Good Solvent" *Macromolecules* **1987**, 20, 1935-1943.
27. Rubinstein, M.; Colby, R. H., *Polymer Physics*. Oxford University Press: New York, 2003.
28. Bodycomb, J.; Funaki, Y.; Kimishima, K.; Hashimoto, T. "Single-grain lamellar microdomain from a diblock copolymer" *Macromolecules* **1999**, 32, 2075-2077.
29. Koizumi, S.; Hasegawa, H.; Hashimoto, T. "Ordered Structures of Block Copolymer/Homopolymer Mixtures.5. Interplay of Macrophase And Microphase Transitions" *Macromolecules* **1994**, 27, 6532-6540.

Chapter 7.

Summary and Future Work

In this chapter, the main accomplishments of the thesis will be summarized and a list of suggestions for future research directions will be presented.

7.1. Thesis Summary

The work presented in this thesis deals with structure-property relationships and applications of block copolymer enabled photonic bandgap materials. Over the past years, block copolymers have proven to be promising building blocks in the fields of photonic crystals.¹⁻⁴ On the basis of this successful introduction as passive photonic platforms, we extended our interest of these materials towards realizing active photonic elements such as photonic microcavity for optically driven lasing and stimulus responsive self-assembled reflectors for sensing and display application. Three separate but related projects have been accomplished.

In the first part of this thesis (chapters 3 and 4), we pursued thin film organic lasers using block copolymer based self-assembled Bragg reflectors in conjunction with organic chromophores. The study of a defect-mode laser structure described in chapter 3 provided a basic understanding of photonic microcavity for optically pumped lasing with an organic gain medium. Using TiO₂ nanoparticles and PMMA as the high and low index materials with the organic laser dye (DCM), a novel organic/inorganic hybrid 1D photonic crystal containing a dye-doped defect layer was successfully demonstrated. With the aid of TMM calculations, a localized defect-mode having the highest photon density of states was purposefully matched with the location of the maximum peak wavelength of the spontaneous emission from the organic gain medium. Low threshold single-mode lasing was thus induced at the defect-mode frequency resulting from the suppressed density of states of photons within the photonic bandgap and the enhanced rates of spontaneous

emission at the localized resonant defect mode. In chapter 4, we considered the fabrication of a photonic microcavity using a self-assembled block copolymer photonic crystal. Well-ordered thin film microstructures of a high molecular weight PS-b-PI block copolymer were obtained by confining the block copolymer solution between glass substrates. These self-assembled Bragg reflectors provided narrow spectral-band selective feedback for an organic gain thin film laser cavity. Above the lasing threshold, sharp single-mode surface-emitting lasing was successfully demonstrated with a significant spectral narrowing of lasing emission.

In the second part of this thesis (chapter 5), we examined stimulus responsive tunable reflectors based on 1D block copolymer photonic crystals. Three types of external stimuli: (1) solvent (solvatochromic), (2) temperature (thermochromic), and (3) compressive mechanical strain (mechanochromic) were successfully employed to tailor the structural (a lattice constant) and material (effective refractive indices of respective layers) properties of lamellar block copolymer photonic crystals, resulting in effective tuning of their spectral characteristics. Using TMM calculations with a model finite 1D photonic crystal system, semi-quantitative explanations for how the peak reflectivity wavelength depends on the magnitude of the particular stimulus have been provided.

In the third part of this thesis (Chapter 6), we explored control of the thin film microdomain orientation and a novel 3D optical characterization method for block copolymer photonic crystals. Using directional solidification (DS) of a crystallizable solvent, we successfully created highly oriented thin film microdomain patterns of 1D and 2D periodic block copolymer photonic crystals over a large area. Moreover, it was shown

that the orientational behavior of these ultrahigh molecular weight photonic block copolymers (~ 20 times larger molecular weight than for previously studied block copolymers) in the DS process is dramatically different from that of directionally solidified conventional molecular weight block copolymers. Due to the large domain sizes of the ultrahigh molecular weight block copolymers, laser scanning confocal microscopy (LSCM) could be successfully used to optically characterize the lamellar and cylindrical thin film structures in 3D space.

7.2. Future Work

Some of the issues covered in this thesis are worthy of further investigations. In this section, future research directions that can build upon the results of the present work will be presented.

In the area of optically driven lasing with block copolymer photonic crystals explored in Chapter 4, one interesting work which can be continued is to develop a self-assembled distributed feedback (DFB) laser device, for which an organic chromophore is distributed throughout block copolymer lamellae, a feedback structure. Some key issues for this work include the optimization of block copolymer microstructure for achieving a higher reflectivity, and the choice of high-gain organic laser dyes such as Rhodamin 6G and Bis-MSB and an effective pump source. A preliminary experiment conducted with PS-b-PI (320k/270k) block copolymer containing Bis-MSB and cumene cast between glass

substrates showed a quite promising result (this work is in collaboration with Dr. Songho Cho at MIT) as shown in Figure 7.1. The spectral characteristics of the self-assembled DBF structure can be further tuned by various external stimuli as described in Chapter 5. This block copolymer based DFB structure is expected to create self-assembled all-organic thin film laser device with dynamic lasing tunability via various external stimuli.

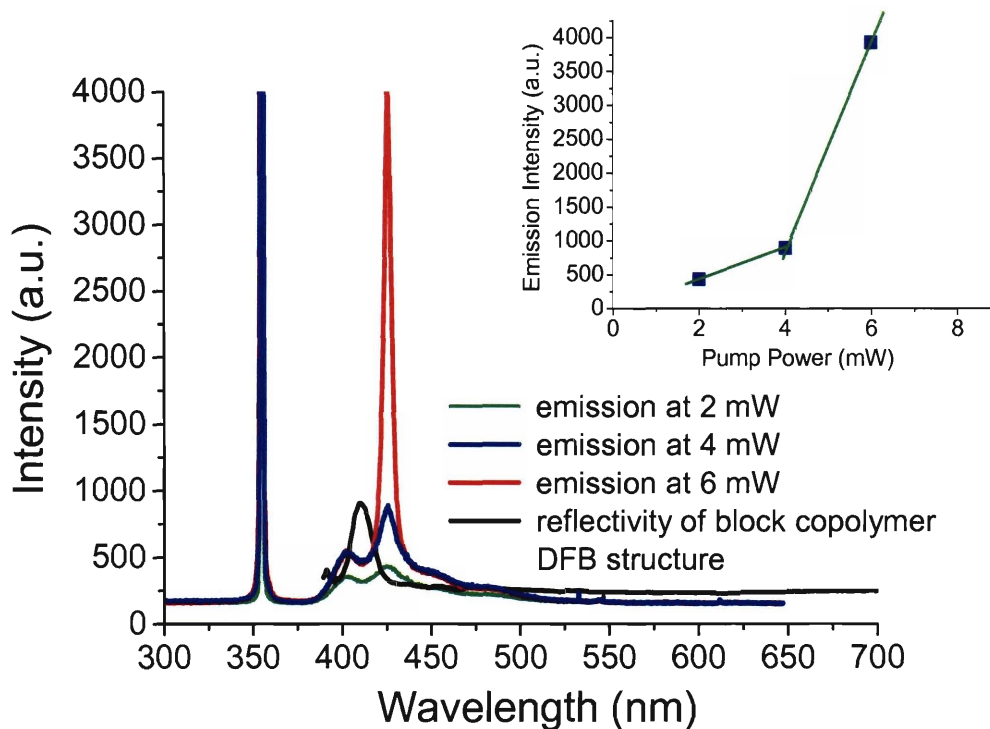


Figure 7.1: Emission spectra of the self-assembled distributed feedback (DFB) laser structure enabled with PS-b-PI (320k/270k) block copolymer and Bis-MSB. The inset shows the pump power dependence of emission intensity of the block copolymer based DFB structure.

Another interesting idea which can be continued based on the work in Chapter 4 is to fabricate an electrically tunable, optically pumped all-organic laser. In this case, liquid

crystal-containing moieties can be introduced into the block copolymer photonic structures as electro-active additives. One of readily available candidate electroactive materials would be side-chain liquid crystalline homopolymers or block copolymers, in which liquid crystalline mesogens are attached to the polymer backbone. Such side-chain liquid crystalline materials could be blended with high molecular weight block copolymers to form electro-optic nanocomposite photonic structures between ITO-coated polymeric substrates. The refractive index of the LC-containing domains would vary as the optic-axis orientation of the LC molecules respond to an applied electric field. A photonic microcavity is then fabricated with a organic gain medium either deposited between electrically responsive self-assembled reflectors or doped within block copolymer reflectors for DFB lasing. With an applied electric field, the optical feedback from the block copolymer reflectors varies and therefore the lasing wavelength can be expected to change, leading to electrically tunable, optically pumped all-organic laser devices on flexible substrates.

In the area of stimulus responsive reflectors explored in Chapter 5, we believe there are still many issues that can be further investigated to improve the spectral properties of the system and elucidate the underlying structure-property relationships more clearly. In particular, it would be very helpful if any experimental methods can characterize the change of lamellar domain orientation and domain spacing in-situ (i.e. LSCM and polarization dependent studies). Additionally, kinetic studies of the stimulus responsive reflectors can be done more systematically, in particular, for the mechanochromic block copolymer gels, the time dependence of the reflectivity peak corresponds to stress relaxation via defect mediated alteration of the number of periods in the compressed stack.

In the area of directional solidification of ultrahigh molecular weight block copolymers as explored in Chapter 7, more experimental work is necessary for a deeper understanding of the dramatically different ordering behavior with different molecular weight of block copolymers. Any experimental techniques that can monitor the growth of the microphase during the directional solidification process will be very desired for this study.

As for the studies of ultrahigh molecular block copolymers, another interesting future research direction is to employ the laser scanning confocal microscopy (LSCM) technique to characterize various dynamic processes of block copolymers in real-space. In particular, it would be of special interest to study the dynamic processes of the order-disorder transition (ODT) (via both lyotropic and thermotropic transitions) and order-order transition (OOT) occurring in various block copolymer/terpolymer morphologies. Although the ordering kinetics of block copolymers have been extensively investigated over the past decade, the previously obtained experimental results on relatively modest molecular weight block copolymers mainly relied on the information in reciprocal space obtained from various scattering techniques⁵⁻⁸ and several ex-situ real-space analyses using transmission electron microscopy (TEM).^{9, 10} These approaches, however, are limited to providing an average description of the overall process and can not follow the detailed changes in microdomain shape and alignment continuously in a specific area over time during the transformation process. In conventional time-resolved temperature drop experimental procedures, the temperature of the specimen is quenched from a temperature above ODT temperature, T_{ODT} , to a temperature below T_{ODT} and the evolution of morphology is

monitored. Since the melt T_{ODT} or the T_{OOT} of the ultrahigh molecular weight block copolymer would be inaccessibly high due to the very high χ_N , we would add nonvolatile neutral solvent (e.g. dioctylphthalate (DOP) for PS-b-PI) to reduce the transition temperatures to a temperature range well below the thermal degradation temperature of the block copolymers.¹¹ The resulting ordered block copolymer gels can be confined between two glass substrates at various concentrations and thicknesses for LSCM studies. For temperature control of the block copolymer material, a conventional or custom-made microscope hot stage for LSCM could be used (e.g. thermoelectric heater). Complementary experiments using ultra small angle X-ray scattering (USAXS) can also be conducted to provide supporting information to LSCM studies. USAXS exposures however require times of more than 1/2 hour and average over the entire sample volume ($\sim 0.25 \text{ mm}^3$) and as previously mentioned can not distinguish the details of locally occurring morphological processes of block copolymers. The expected outcomes of this proposed study include a) first direct 3D visualization of the mechanisms in ordering process of block copolymers (e.g. nucleation and growth of a new phase at defects and (possible) epitaxial relations of the parent and daughter phases), b) identification of novel non-equilibrium phases during the ordering process, and c) elucidation of formation and evolution of grain boundaries and defects (size, shape, and orientation) during the ordering process, all of which have not been fully understood in previous studies using conventional characterization techniques. Such investigations are expected to enable a more comprehensive understanding of the self-assembly process of block copolymers.

7.3. References

1. Fink, Y.; Urbas, A. M.; Bawendi, M. G.; Joannopoulos, J. D.; Thomas, E. L. "Block copolymers as photonic bandgap materials" *Journal of Lightwave Technology* **1999**, 17, 1963-1969.
2. Urbas, A. M. *Block Copolymer Photonic Crystals. Ph. D. Thesis*, Massachusetts Institute of Technology, Cambridge, 2003.
3. Edrington, A. C.; Urbas, A. M.; DeRege, P.; Chen, C. X.; Swager, T. M.; Hadjichristidis, N.; Xenidou, M.; Fetters, L. J.; Joannopoulos, J. D.; Fink, Y.; Thomas, E. L. "Polymer-based photonic crystals" *Advanced Materials* **2001**, 13, 421-425.
4. Yoon, J.; Lee, W.; Thomas, E. L. "Self-assembly of block copolymers for photonic-bandgap materials" *MRS Bulletin* **2005**, 30, 721-726.
5. Sakamoto, N.; Hashimoto, T. "Ordering dynamics of a symmetric polystyrene-block-polyisoprene. 1. Ordering mechanism from the disordered state" *Macromolecules* **1998**, 31, 3292-3302.
6. Balsara, N. P.; Hammouda, B.; Kesani, P. K.; Jonnalagadda, S. V.; Straty, G. C. "In-situ Small-Angle Neutron Scattering from a Block Copolymer Solution under Shear" *Macromolecules* **1994**, 27, 2566-2573.
7. Harkless, C. R.; Singh, M. A.; Nagler, S. E.; Stephenson, G. B.; Jordansweet, J. L. "Small-Angle X-Ray-Scattering Study of Ordering Kinetics in a Block Copolymer" *Physical Review Letters* **1990**, 64, 2285-2288.

8. Abuzaina, F. M.; Garetz, B. A.; Mody, J. U.; Newstein, M. C.; Balsara, N. P. "Birefringence and Depolarized Light Scattering from Ordered Block Copolymers with Anisotropic Distributions of Grain Orientations Produced by Shear Flow" *Macromolecules* **2004**, *37*, 4185-4195.
9. Sakamoto, N.; Hashimoto, T. "Ordering Dynamics of Cylindrical and Spherical Microdomains in Polystyrene-block-Polyisoprene-block-Polystyrene. 1. SAXS and TEM Observations for the Grain Formation" *Macromolecules* **1998**, *31*, 8493-8502.
10. Sota, N.; Sakamoto, N.; Saijo, K.; Hashimoto, T. "Phase Transition from Disordered Sphere to Hex-Cylinder via Transient Ordering into Bcc-Sphere in SIS Triblock Copolymer" *Macromolecules* **2003**, *36*, 4534-4543.
11. Chastek, T. Q.; Lodge, T. P. "Grain Shapes and Growth Kinetics of the Cylinder Phase in a Block Copolymer Solution" *Macromolecules* **2004**, *37*, 4891-4899.

Appendix.

Polyolefin Based Photonic Bandgap Materials

In this appendix, we present the results from our investigation of polyolefin based photonic bandgap materials. Block copolymers based on readily available olefins have been synthesized to construct self-assembled one-dimensional (1D) photonic crystals. Using living olefin polymerization via a bis(phenoxyimine) titanium dichloride/MAO catalyst system, optically transparent and high molecular weight polyolefin block copolymers have been prepared with a narrow molecular weight distribution. The resulting copolymers, poly[(MCP-*co*-VTM)-*b*-(E-*co*-N)] and poly[(E-*co*-P)-*b*-(E-*co*-N)], exhibited a 1D photonic bandgap with an excellent optical transparency. Random copolymerization of olefin monomers provided a route to tune the refractive index of each block as well as to suppress the crystallinity for optical transparency. Ternary blending of diblock copolymer with homopolymers further afforded a pathway to control the wavelength of the peak reflectivity of the polyolefin based photonic structures.

This project was a collaboration with Dr. Robert Mathers and Prof. Geoffrey Coates at Cornell University, who had conducted the synthesis of polyolefin block copolymers used in this study. Parts of this chapter were featured in: J. Yoon, R. T. Mathers, G. W. Coates, E. L. Thomas *Macromolecules* **2006**, *39*, 1913-1919.

A.1. Introduction

Polyolefins have been widely used in various applications due to their versatile thermal, mechanical, and optical properties determined by their composition, chain architecture and the tacticity.¹ Recent advances in catalyst systems for living olefin polymerization have made it possible to synthesize polyolefin-based block copolymers with precisely controlled molecular weight, molecular weight distribution and tacticity.² For example, diblock copolymers of syndiotactic polypropylene-*b*-(ethylene-*co*-propylene) have been synthesized with a controlled molecular weight and a narrow molecular weight distribution ($M_w/M_n \sim 1.1$).³ More recently, bis(phenoxyimine) titanium dichloride/MAO catalysts were used for the polymerization of 1,5-hexadiene to give a random copolymer with 1,3-methylenecyclopentane (MCP) and 3-vinyltetramethylene (VTM) units.⁴ The VTM units in the copolymer have been shown to undergo a cross metathesis reaction with alkenes catalyzed by a ruthenium carbene for additional functionalization of the copolymer.⁵

The work described here is motivated by our interest in preparing polyolefin based photonic bandgap materials, which are expected to have improved thermal stability and processability over more conventional diene-containing block copolymers such as poly(S-*b*-I). Here, we present the synthesis and morphological/optical characterization of lamellar-forming polyolefin block copolymers with highly controlled molecular weight and optical transparency, which can form self-assembled 1D photonic bandgap structures.

A.2. Experimental

A.2.1. Synthesis

All air and moisture sensitive chemistry was carried out in a MBraun Labmaster dry box or using standard Schlenk line techniques. The solvents were dried on solvent columns containing molecular sieves, alumina and activated copper. Propylene (Matheson, Polymer Grade) was purified by a column of molecular sieves and alumina. Ethylene (Matheson, Polymer Grade) was used as received. Polymethylaluminoxane (Akzo Nobel, PMAO-IP, 12.9 wt% Al in toluene) was dried under vacuum at 60 °C overnight. The bis(salicylaldiminato)titanium complex was prepared as previously described.³

Synthesis of poly[(MCP-*co*-VTM)-*b*-(E-*co*-N)] diblock copolymer

A 6 oz. Lab-Crest® glass pressure reaction vessel (Andrews Glass) was charged with PMAO (0.19 g, [Al]/[Ti] = 600), toluene (125 mL) and 1,5-hexadiene (10 mL). The reactor was equilibrated at 0 °C in an ice-bath and a catalyst solution [4 mg of **1** (Scheme 1) in 5 mL of toluene]³ was injected by syringe. After 15 min, the reactor was evacuated to remove excess 1,5-hexadiene for 5 min and backfilled with nitrogen. An aliquot (10 mL) was taken and quenched with acidic methanol. Subsequently, the norbornene (10 g in 10 mL of toluene) was injected by syringe and ethylene was attached at 2 psi. After 29.25 h, acidic methanol (3 mL) was added by syringe to quench the polymerization. The reactor was then vented and the polymer precipitated in acidic methanol (700 mL). After stirring for several hours, the polymer was filtered, washed with methanol and dried under vacuum

(recovered 2.14 g).

Synthesis of poly[(E-co-P)-*b*-(E-co-N)] diblock copolymer

A 6 oz. Lab-Crest® glass pressure reaction vessel (Andrews Glass) was charged with PMAO (0.10 g, [Al]/[Ti] = 250) and toluene (120 mL). The reactor was weighed and placed in an ice-bath. The nitrogen atmosphere in the reactor was exchanged with propylene three times. Propylene (4.0 g) was condensed into the reactor for 30 min at 10 psi. The ethylene was attached at 12 psi. The catalyst solution (10 mg of **1** (Scheme 1) in 4 mL of toluene) was injected by syringe. After 10 min, the reactor was evacuated to remove ethylene and propylene for 2 min. The reactor was backfilled with nitrogen. An aliquot (10 mL) was taken and quenched with acidic methanol. The norbornene (5 g in 10 mL of toluene) was injected by syringe. Ethylene was attached at 1.5 psi. After 21.5 h, acidic methanol (3 mL) was added to quench the polymerization. The reactor was vented and the polymer precipitated in acidic methanol (700 mL). After stirring for several hours, the polymer was filtered, washed with methanol and dried under vacuum (recovered 2.3 g).

A.2.2. Characterization

The 125 MHz ¹³C NMR data were acquired on a Varian Inova 500 spectrometer. The polymer samples were placed in a 5 mm NMR tube with 1,1,2,2-tetrachloroethane-*d*₂ and dissolved by heating. The data were acquired at 130 °C using an inverse gated decoupling sequence with a 5 s relaxation delay. The NMR spectra were referenced to non-deuterated solvent shifts. The copolymer microstructure was calculated according to

published procedures for poly(ethylene-*co*-propylene) copolymers,^{3, 6, 7} and poly(ethylene-*co*-norbornene) copolymers.^{8, 9}

The molecular weights (M_n and M_w) and polydispersity indices (M_w/M_n) were measured by a Waters Alliance GPCV 2000 size exclusion chromatograph (SEC). The SEC columns (4 Waters HT 6E and 1 Waters HT 2) were eluted at 1.0 mL/min with 1,2,4-trichlorobenzene containing 0.01 wt% di-*tert*-butylhydroxytoluene (BHT). The molecular weights (M_n and M_w) and polydispersity indices (M_w/M_n) were measured relative to a polystyrene calibration curve at 140 °C. DSC analysis was performed on a TA Instruments Q1000 equipped with an autosampler and a liquid nitrogen cooling system. Typical DSC samples (2-3 mg) were prepared in crimped aluminum pans and heated under nitrogen at a rate of 10 °C/min from -80 to +200 °C. The reported DSC data was acquired from the second heating run and processed with the TA Q Series software.

In order to measure the wavelength dependence of refractive index (dispersion), ellipsometry was performed using a M2000 variable angle spectroscopic ellipsometer (J. A. Woollam Co., Inc.) with 70° incidence angle. Thin films for ellipsometry (thickness ~ 100 nm) of polyolefin random copolymers were prepared by spin casting the copolymer solution on a silicon wafer. Toluene was used as a solvent for all polyolefin copolymers. Thick films for reflectivity measurement and transmission electron microscopy (TEM) (thickness ~ 0.2-0.3 mm) of poly[(MCP-*co*-VTM)-*b*-(E-*co*-N)] and poly[(E-*co*-P)-*b*-(E-*co*-N)] were cast from a solution of the copolymer in toluene (~ 4 wt%). To minimize defect formation during the solution casting process, a very slow evaporation condition was applied, where the evaporation of a solvent was conducted in a solvent-saturated

atmosphere with a gentle flux of air, requiring two to three weeks for sample drying. The blends of poly[(E-co-P)-*b*-(E-co-N)] were prepared by mixing 80 wt% (60 wt%) of the host block copolymer with 10 wt% (20 wt%) of poly(E-co-P) ($M_n=23.2k$, PDI=1.11) and 10 wt % (20 wt%) of poly(E-co-N) ($M_n=23.8k$, PDI=1.06) in toluene for 20 wt% (40 wt%) blend. All samples were further dried in vacuum at room temperature for 24 h and subsequently annealed at 120 °C for 3 to 10 days, producing films with a final thickness of about 0.2-0.3 mm. Ultrathin sections for TEM were obtained using Reicht-Jung Ultracut FC4E cryomicrotome. To provide mass thickness contrast between block copolymer microdomains, poly[(MCP-co-VTM)-*b*-(E-co-N)] was stained with osmium tetroxide (OsO_4) while poly[(E-co-P)-*b*-(E-co-N)] and its blends were stained with ruthenium tetroxide (RuO_4). TEM micrographs were obtained using JEOL 200CX and JEOL 2000FX microscopes operating at 200 kV. Measurement of film reflectivity spectra was conducted on a Cary 5E UV-VIS-NIR spectrophotometer (Varian Inc.) equipped with a diffuse reflectance accessory. The diffuse reflectance of Halon, a compressed polyfluorocarbon powder with reflectivity above 99% over the visible wavelengths, was used as a reference spectrum. USAXS measurements of the poly[(E-co-P)-*b*-(E-co-N)] diblock copolymer and its ternary blends were performed at beamline X10A at Brookhaven National Laboratory with 8 keV radiation (wavelength $\lambda = 0.1548$ nm). A Bonse-Hart camera setup¹⁰ was employed with single bounce Ge-111 monochromator and analyzer crystals. The slit collimated incident beam intensity was about 5×10^9 cts/s and the beam size was 0.6×0.8 mm² (V-H). Data were collected by a scintillation detector (Bicron) which was swept through an arc to collect a linear data set of intensity versus angular position. All data were

acquired at room temperature and used without additional corrections.

A.3. Results and Discussion

Polyolefins are often crystallizable and can exhibit a semicrystalline morphology due to the configurational regularities of the repeating units. As a result, spherulites containing chain folded lamellae form upon crystallization and can cause a strong scattering of visible light, making polyolefins less appropriate for optical applications compared with highly transparent non-crystalline polymers such as polymethylmethacrylate. The “random copolymer” approach employed in this study is an effective means to introduce configurational irregularities along the main chain of the copolymers, which inhibit crystallization and thus maintain optical transparency of the polyolefin block copolymers. In the design of “photonic” polyolefins, the following monomers were selected as building blocks for the synthesis of polyolefin block copolymers: ethylene (E), propylene (P), norbornene (N) and 1,5-hexadiene. Random copolymers of these monomers were synthesized with a living catalyst system to give a controlled molecular weight, a narrow molecular weight distribution, and an optical transparency, as summarized in Table 1. No melting transitions were observed in all the polyolefin random copolymers studied as determined by DSC.

<i>Entry</i>	<i>Description</i>	<i>E</i> (mol %) ^a	<i>M_n</i> (kg/mol) (<i>M_w/M_n</i>) ^b	<i>T_g</i> (°C) ^c	<i>n</i> ^d	<i>d</i> ₀₀₁ (nm) ^e
1	poly(E-co-N)	62	238 (1.05)	86.5	1.52	-
2	poly(E-co-P)	62	192 (1.09)	-58.3	1.47	-
3	poly(MCP-co-VTM)	-	87 (1.12)	-19.3	1.50	-
4	poly[(MCP-co-VTM)- b-(E-co-N)]	-/ ^h	180 (1.35)/ 451 (1.41) ^e	-19.3/ 73.1 ^f	-	170
5	poly[(E-co-P)- b-(E-co-N)]	58/67	212 (1.12)/ 576 (1.13) ^e	-55.5/ 71.6 ^f	-	91
6	poly(E-co-N)	67	23.8 (1.06)	69.2	1.52	-
7	poly(E-co-P)	58	23.2 (1.11)	- 56.2	1.47	-

^aData measured by ¹³C NMR, 130 °C, in 1,1,2,2-tetrachloroethane-d₂. ^bData measured by GPC eluted with 1,2,4-trichlorobenzene at 140 °C relative to polystyrene standards, each value in parenthesis corresponds to PDI. ^cData measured by DSC (10 °C/min). ^dData at 500 nm, measured by spectroscopic ellipsometry. ^eData refer to the first polymer block/entire diblock copolymer. ^fData refer to the first polymer block/second polymer block. ^gDomain periodicity of lamellae measured from TEM, i.e. $d_{001}=l_A+l_B$. ^hThe ethylene content was not able to be obtained using ¹³C NMR spectra since the ¹³C NMR peak for the poly[(MCP-co-VTM)] block was overlapped with the peak for the poly[(E-co-N)] block. The glass transition temperatures (*T_g*) of poly[(MCP-co-VTM)-b-(E-co-N)] can be used to estimate the ethylene content of the copolymer since the *T_g* of (E-co-N) block sensitively depends on the ethylene content. Given that the glass transition temperature of (E-co-N) of poly[(MCP-co-VTM)-b-(E-co-N)] (entry 4 in Table 1, 73.1 °C) is similar to that of (E-co-N) of poly[(E-co-P)-b-(E-co-N)] (entry 5 in Table 1, 71.6 °C, ethylene content is 67%), 67% would be a reasonable estimate for the ethylene content of poly[(MCP-co-VTM)-b-(E-co-N)], although the effect of the other block (i.e. poly(MCP-co-VTM) or poly(E-co-P) needs to be considered for more precise estimation.

Table A.1. Materials data for polyolefin copolymers

A key intrinsic material property for determining a bandgap of photonic crystal is the respective refractive index of each domain of the crystal. In this study, two different approaches were employed to tailor the dielectric contrast of polyolefin-based photonic crystals. First, monomers of different refractive indices were copolymerized to form a random copolymer. Polyolefin random copolymers made of the above-mentioned monomers were then evaluated to determine an effective refractive index and how the various combinations of random copolymer blocks would influence the dielectric contrast. Figure A.1 shows the wavelength dependence of the refractive index for various polyolefin random copolymers, as measured by spectroscopic ellipsometry over the visible wavelength range. Clearly the refractive index ($=\epsilon^{1/2}$, where ϵ is a dielectric constant of medium) can be readily tuned by simply varying the combination of different monomers. As shown in Figure A.1, in ethylene-containing random copolymers, poly(E-co-N) ($n \sim 1.52 @ 500 \text{ nm}$) exhibited higher refractive index than poly(E-co-P) ($n \sim 1.47 @ 500 \text{ nm}$) at the same ethylene content (62%) due to the lower refractive index of polypropylene ($n \sim 1.47-1.49$)¹¹ than polynorbornene ($n \sim 1.52-1.54$).¹²

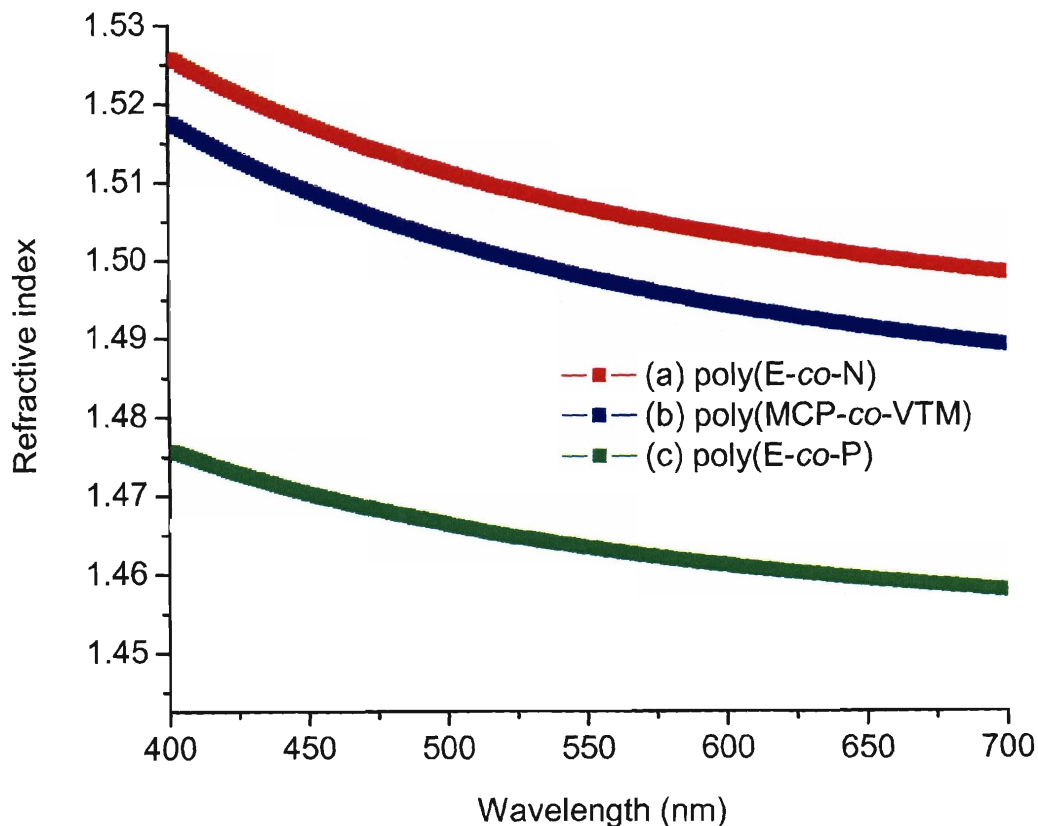


Figure A.1: Refractive index as a function of wavelength for polyolefin random copolymers measured by a spectroscopic ellipsometry, (a) poly(E-co-N) (entry 1 in Table 1), (b) poly(MCP-co-VTM) (entry 3), (c) poly(E-co-P) (entry 2).

Based on the evaluation of refractive index and thermal properties, two sets of polyolefin diblock copolymers, poly[MCP-co-VTM)-*b*-(E-co-N)] and poly[(E-co-P)-*b*-(E-co-N)], were synthesized by a sequential monomer addition. These block copolymer systems were soluble in toluene at room temperature and showed no detectable crystallinity by DSC. Table A.1 summarizes the detailed information of the synthesized block copolymers. TEM was performed on thermally-annealed films of the copolymers after

cryomicrotomy and staining. Figure A.2 shows a bright field TEM micrograph of a poly[(MCP-*co*-VTM)-*b*-(E-*co*-N)]. A lamellar morphology exhibiting a periodicity of about 170 nm is clearly evident with alternating layers of poly(MCP-*co*-VTM) and poly(E-*co*-N). The dark regions correspond to poly(MCP-*co*-VTM) domains, in which VTM units containing the alkene group were preferentially stained with osmium tetroxide (OsO₄) while the bright regions correspond to the poly(E-*co*-N) domains.

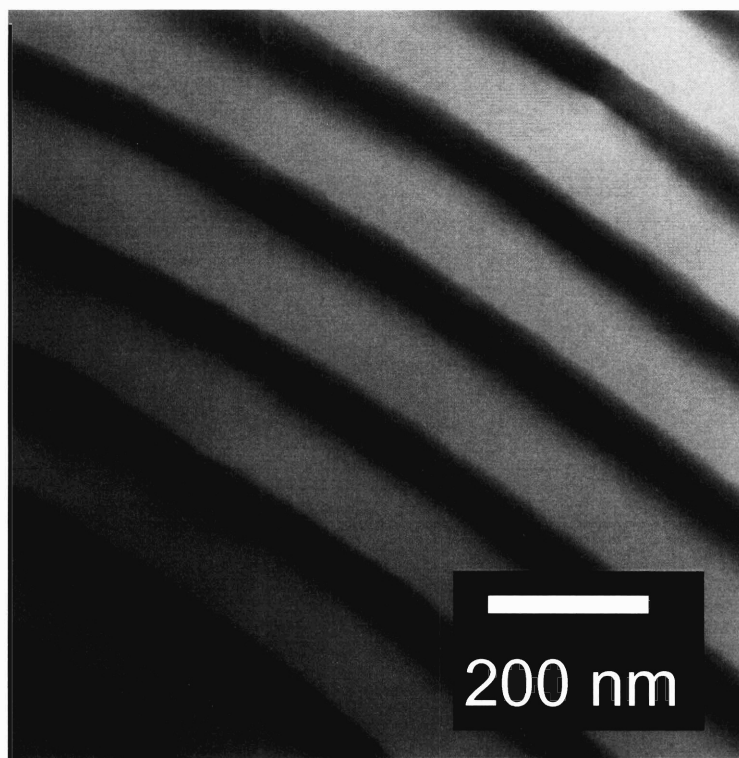


Figure A.2: Bright field TEM micrograph of cryomicrotomed section of the poly[(MCP-*co*-VTM)-*b*-(E-*co*-N)] block copolymer showing a lamellar morphology (domain periodicity ~ 170 nm). The dark regions ($l_{\text{MCP-co-VTM}} = 68$ nm) correspond to poly(MCP-*co*-VTM) microdomains preferentially stained with osmium tetroxide (OsO₄) and the bright regions ($l_{\text{E-co-N}} = 102$ nm) are poly(E-*co*-N) microdomains.

A self-assembled block polymer having a lamellar morphology can form a multilayer stack of one-dimensionally periodic index of refraction or a 1D photonic crystal. In order to examine the optical properties of the self-assembled 1D photonic film, a reflectivity spectrum was obtained by a CARY spectrophotometer equipped with a diffusive reflectivity accessory. As shown in Figure A.3, the spectrum of poly[MCP-*co*-VTM)-*b*-(E-*co*-N)] copolymer film exhibited a reflectivity band resulting from the effect of partial 1D photonic band gap, where the peak reflectivity was centered around 470 nm. A convenient way to understand the obtained reflectivity spectrum is to model the 1D block copolymer photonic structure with a stack of finite number of alternating layers, for which optical properties can be readily calculated by a transfer matrix method (TMM).^{13, 14} Although the computational result with this simple model does not capture all the microstructural details of the block copolymer photonic structure such as the variation of domain size, domain orientation and randomly located defects, it can provide a useful reference to correlate the obtained reflectivity spectrum with morphological properties of the block copolymer photonic structure. Figure A.4 shows a calculated “reflectivity map” of the corresponding model 1D multilayer (100 layers) stack of poly[MCP-*co*-VTM)-*b*-(E-*co*-N)], in which the measured thicknesses (102 nm/68 nm) and refractive indices (1.52/1.50) of the lamellar domains have been used for the calculation and the magnitude of the reflectivity was visualized using different colors as a function of the incidence angle (x-axis), the polarization (x-axis), and the wavelength (y-axis) of the incident light. The region of high reflectivity in Figure A.4, or a partial 1D photonic bandgap, results from a constructive interference of incident light at the set of 1D periodic interfaces between the high and low

refractive domains. The bandgap of the 1D photonic crystal blue-shifts to a shorter wavelength as the incidence angle is increased from zero (normal incidence) to grazing angle. A reflectivity spectrum at a specific incidence angle and polarization can be extracted from a reflectivity map. For example, the inset in Figure A.4 shows a cross-section of the reflectivity map at normal incidence of light (i.e. incidence angle $\theta = 0^\circ$). The calculated peak reflectivity wavelength at normal incidence is around 515 nm while the observed peak reflectivity wavelength is about 470 nm. It is also shown that the width (FWHM) of the measured reflectivity spectrum is much broader than that of the calculated reflectivity spectrum. These comparisons suggest that the lamellar domains of the current block copolymer system are not perfectly oriented along the normal incidence direction but have a distribution of different microdomain orientations. If we assume that the misorientation of lamellae is the dominant factor for the observed reflectivity, the average lamellar orientation (deviation from the normal incidence) can be estimated as 38° , at which the peak reflectivity wavelength is 470 nm from the TMM calculation. Indeed, the self-assembled block copolymer microstructures tend to consist of multiple grains of various domain orientations. The measured reflectivity spectrum in Figure A.4 should be therefore interpreted as the superposed spectral response of many different grains having the distribution of domain thickness, domain orientation, and randomly located defects. In order to do more precise and quantitative modelling of the reflectivity spectrum, we would have to take into account all the above-mentioned microstructural details of the block copolymer photonic structure as well as the optical loss from absorption and scattering.

To further engineer the photonic properties of this poly[(MCP-co-VTM)-*b*-(E-co-

N)] block copolymer, a post-polymerization reaction can be conducted to incorporate a fluorine-containing (low-index) moiety into the poly(MCP-*co*-VTM) block and thus to increase the dielectric contrast. The effect of fluorine-containing group on the microphase separation (increase of Flory-Huggins interaction parameter, χ) and optical properties (increase of Δn by about a factor of 5x) of the block copolymer is currently under investigation.

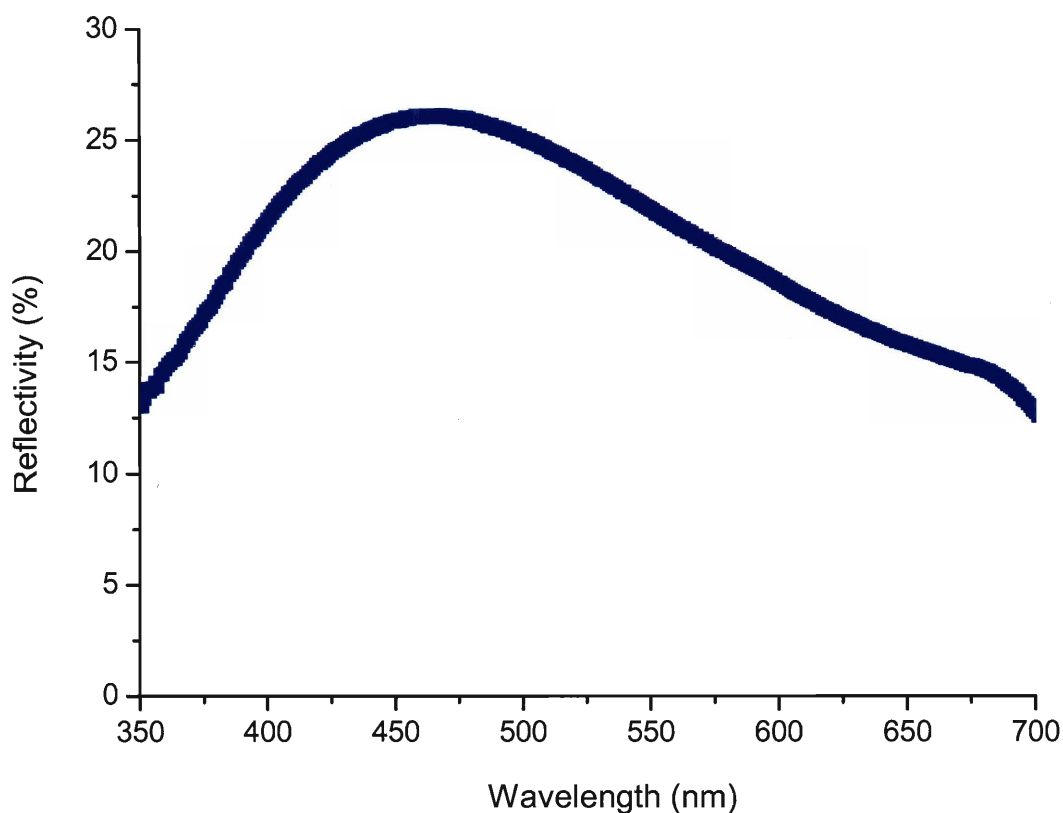


Figure A.3: Measured reflectivity spectrum of poly[(MCP-*co*-VTM)-*b*-(E-*co*-N)] lamellar film by a CARY spectrophotometer equipped with a diffusive reflectivity accessory. The peak reflectivity wavelength is around 470 nm.

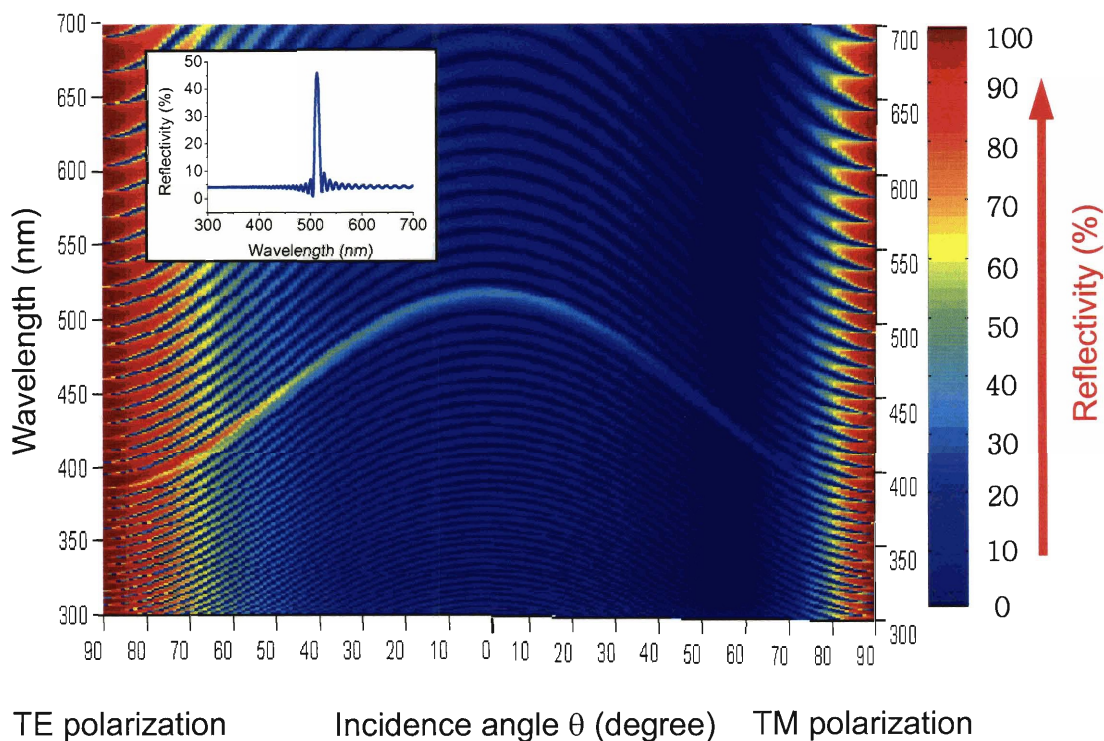


Figure A.4: Calculated reflectivity map of a multilayer stack having the same layer thickness and refractive index as poly[(MCP-co-VTM)-*b*-(E-co-N)] as a function of the incidence angle (x-axis), the polarization (x-axis), and the wavelength (y-axis) of the incident light, assuming the thickness of high (E-co-N)/low (MCP-co-VTM) index layer is 102 nm/68 nm, the refractive index of high/low index layer is 1.52/1.50, and a total number of 100 layers. The inset shows the reflectivity spectrum at normal incidence (incidence angle = 0°) as a function of wavelength, in which the peak reflectivity wavelength is 515 nm.

Another polyolefin diblock copolymer, poly[(E-co-P)-*b*-(E-co-N)], was synthesized using the same living catalyst system. Based on the refractive index and DSC measurements, poly[(E-co-P)-*b*-(E-co-N)] is expected to have a larger dielectric contrast ($\Delta n \sim 0.05$) and be more thermally stable (containing no alkene group in the main chain) than poly[(MCP-co-VTM)-*b*-(E-co-N)]. In this block copolymer system, we further blended lower molecular weight homopolymers of each block, i.e. 10 wt % (20 wt %) of poly(E-co-P) (M_n : 23.2 kg/mol) and 10 wt % (20 wt %) of poly(E-co-N) (M_n : 23.8 kg/mol), with 80 wt % (60 wt %) of the host diblock copolymer, poly[(E-co-P)-*b*-(E-co-N)] (M_n : 212 kg/mol / 364 kg/mol), to swell the lamellar microdomains and to therefore tune the photonic bandgap of the block copolymer photonic crystal to a longer wavelength range. Figure A.5-7 show bright field TEM micrographs of the host poly[(E-co-P)-*b*-(E-co-N)] diblock copolymer and ternary blends of the diblock (80 wt %, 60 wt %) and each homopolymer (10 wt %, 20 wt %), in which the lamellar morphology, composed of dark (E-co-N) domains (stained with ruthenium tetroxide (RuO₄)) and bright (E-co-P) domains, was clearly identified. As shown in Figure A.5-7, the domain periodicity was increased from 91 nm to 127 nm (20 wt % blend) and to 152 nm (40 wt % blend) as a result of swelling of microdomains with added homopolymers.

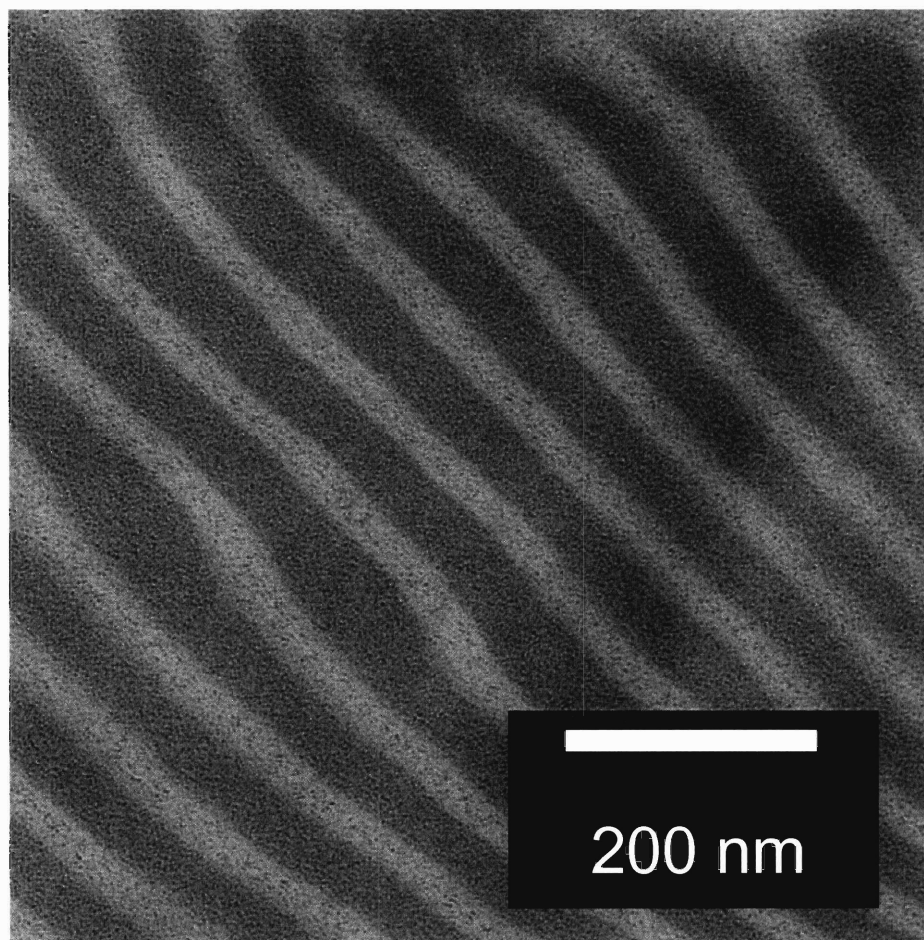


Figure A.5: Bright field TEM micrograph of cryomicrotomed section of the poly[(E-co-P)-*b*-(E-co-N)], in which the domain periodicity is 91 nm ($l_{E-co-N} = 56$ nm, $l_{E-co-P} = 35$ nm). The dark regions correspond to poly(E-co-N) microdomains preferentially stained with ruthenium tetroxide (RuO₄) and the bright regions correspond to poly(E-co-P) microdomains. Small particle-like entities in the micrographs come from ruthenium tetroxide (staining agent) aggregations.

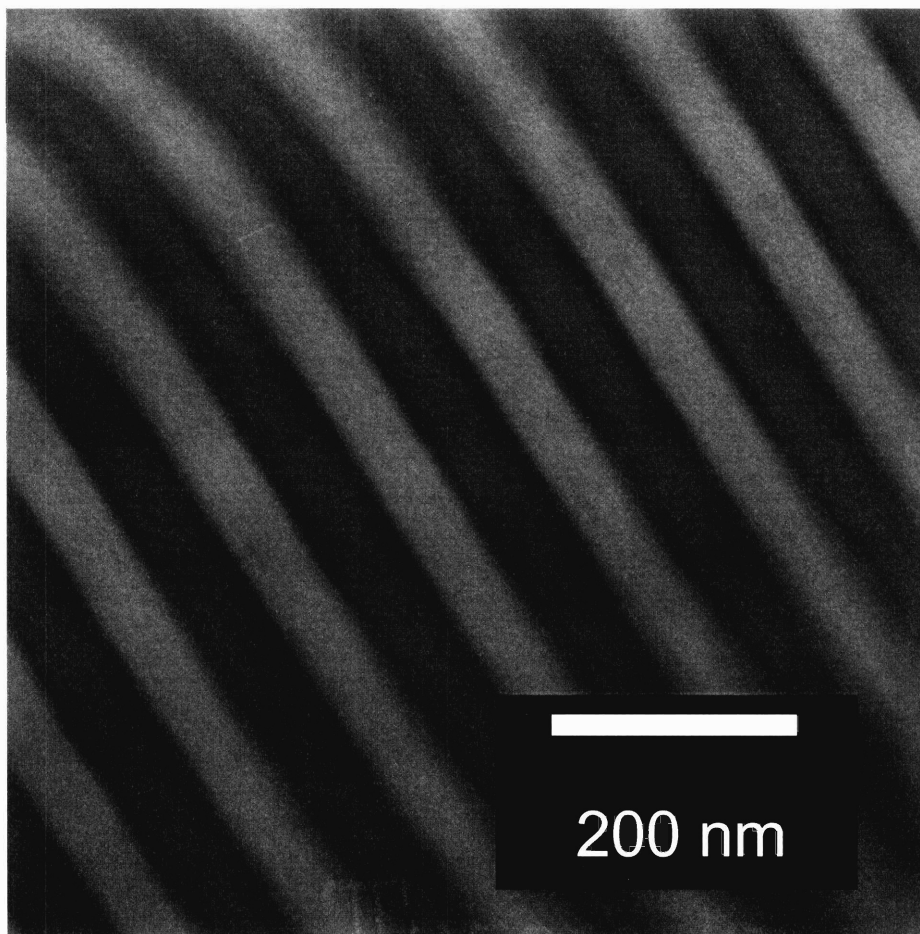


Figure A.6: Bright field TEM micrograph of cryomicrotomed section of the poly[(E-co-P)-*b*-(E-co-N)] ternary blend containing 20 wt % (10/10) homopolymers. The domain periodicity is 127 nm ($l_{E-co-N} = 79$ nm, $l_{E-co-P} = 48$ nm).

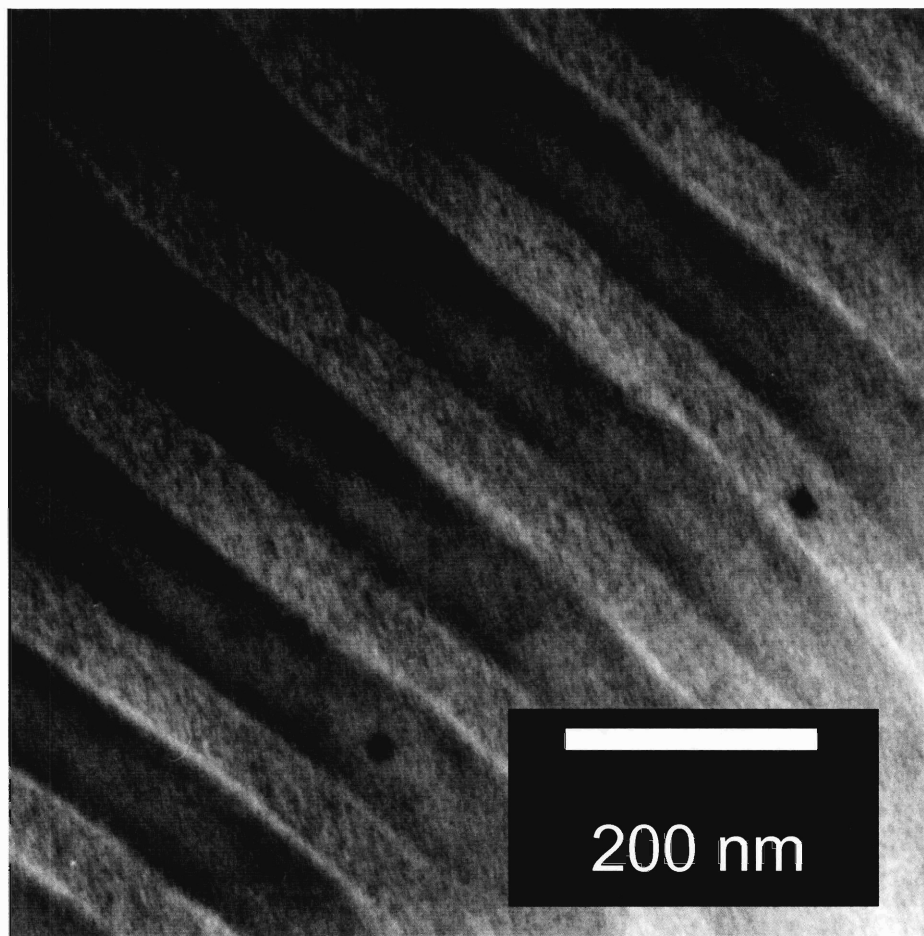


Figure A.7: Bright field TEM micrograph of cryomicrotomed section of the poly[(E-co-P)-*b*-(E-co-N)] ternary blend containing 40 wt % (10/10) homopolymers. The domain periodicity is 152 nm ($l_{E-co-N} = 88$ nm, $l_{E-co-P} = 64$ nm).

The corresponding smeared 1D ultra small angle X-ray scattering (USAXS) data of the samples are presented in Figure A.8, where the shift in the first order peak of scattering vector (q_{001}) to a lower value supports the increase of domain periodicity (d_{001}) in the ternary blends observed in TEM. The domain periodicities obtained from USAXS are in good agreement with those observed from TEM. In order to further confirm the samples have lamellar morphologies, tilting experiments in TEM, which can provide a clear difference between lamellar and cylindrical morphologies, have been conducted and no oblique or end-on views of cylindrical domains have been observed from extensive investigation of many microtomed cross-sectioned samples.

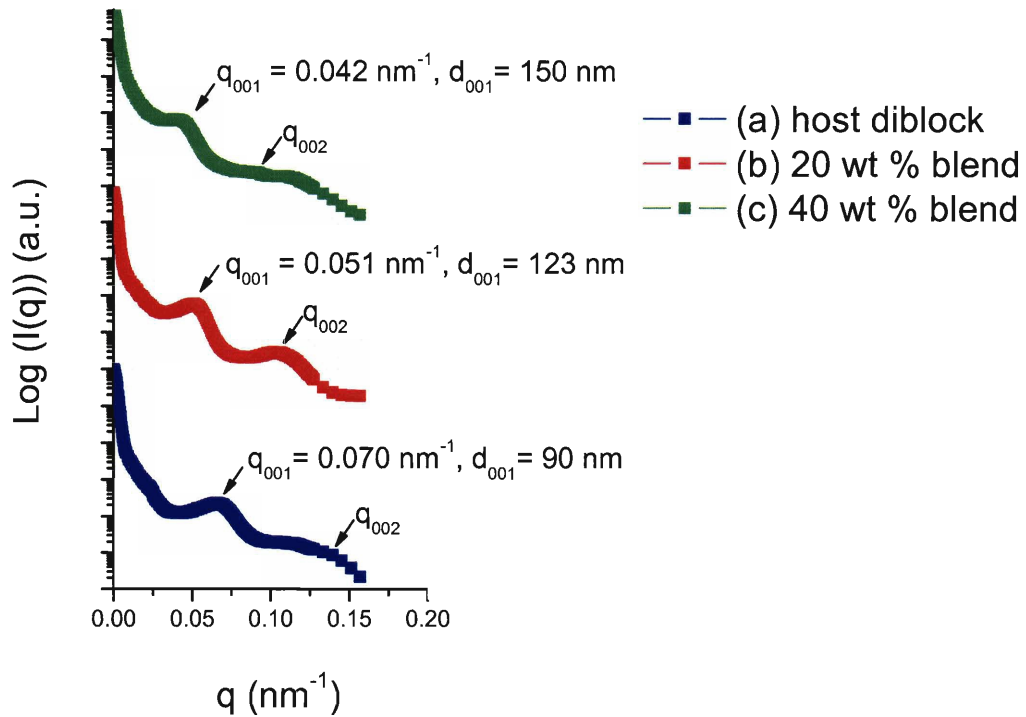


Figure A.8: Smeared USAXS 1D line source data obtained from the polyolefin block copolymer films of (a) the poly[(E-co-P)-b-(E-co-N)] and ternary blends of the diblock containing (b) 20 wt % and (c) 40 wt % homopolymers. The (001) peaks for all three samples correspond well to the lamellar periods measured from TEM micrographs.

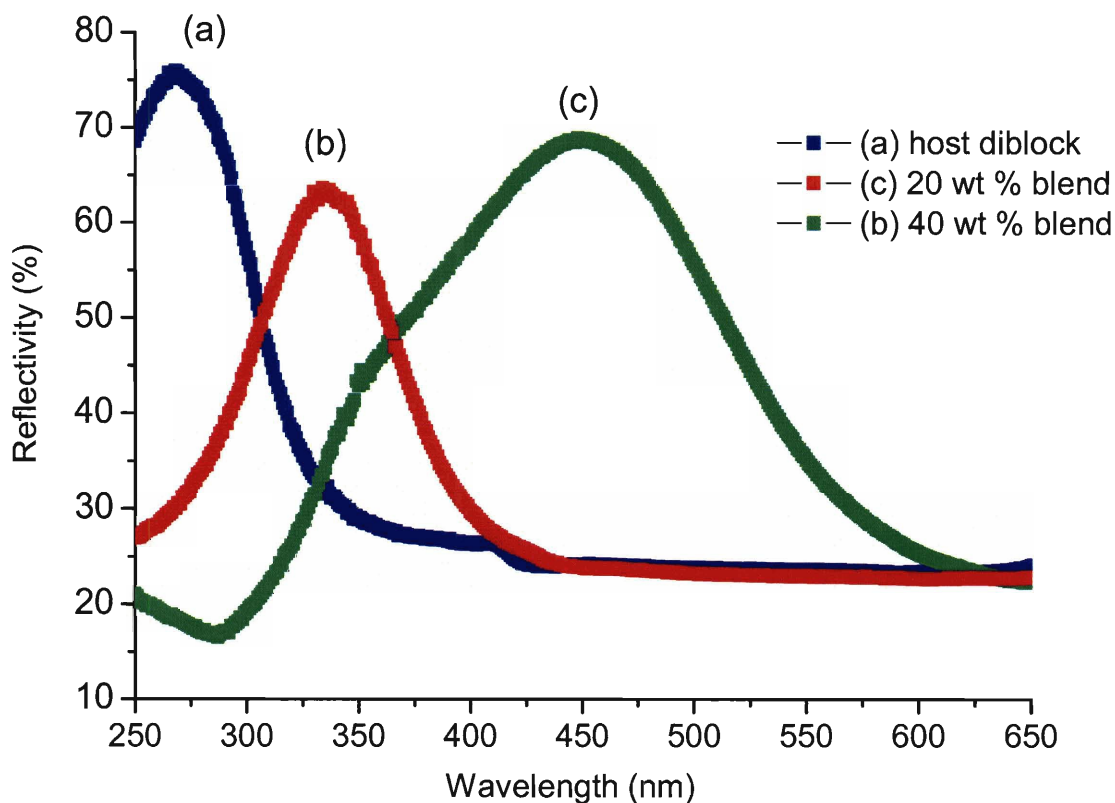


Figure A.9: Measured reflectivity spectra of (a) the poly[(*E-co-P*)-*b*-(*E-co-N*)] and ternary blends of the diblock containing (b) 20 wt % and (c) 40 wt % homopolymers by a CARY spectrophotometer equipped with a diffusive reflectivity accessory. The peak reflectivity wavelengths are (a) 268 nm (host diblock), (b) 335 nm (20 wt % blend), and (c) 448 nm (40 wt % blend), respectively.

In Figure A.9, we show the reflectivity spectra of the host diblock and ternary blend samples measured by a CARY spectrophotometer equipped with a diffusive reflectivity accessory. The peak reflectivity wavelength for the host block copolymer sample occurs at

268 nm, and is red-shifted to 335 nm (20 wt %), and to 448 nm (40 wt %) for the ternary blends as the optical thickness (domain refractive index \times domain thickness) of the blended samples is increased by swelling with added homopolymers.

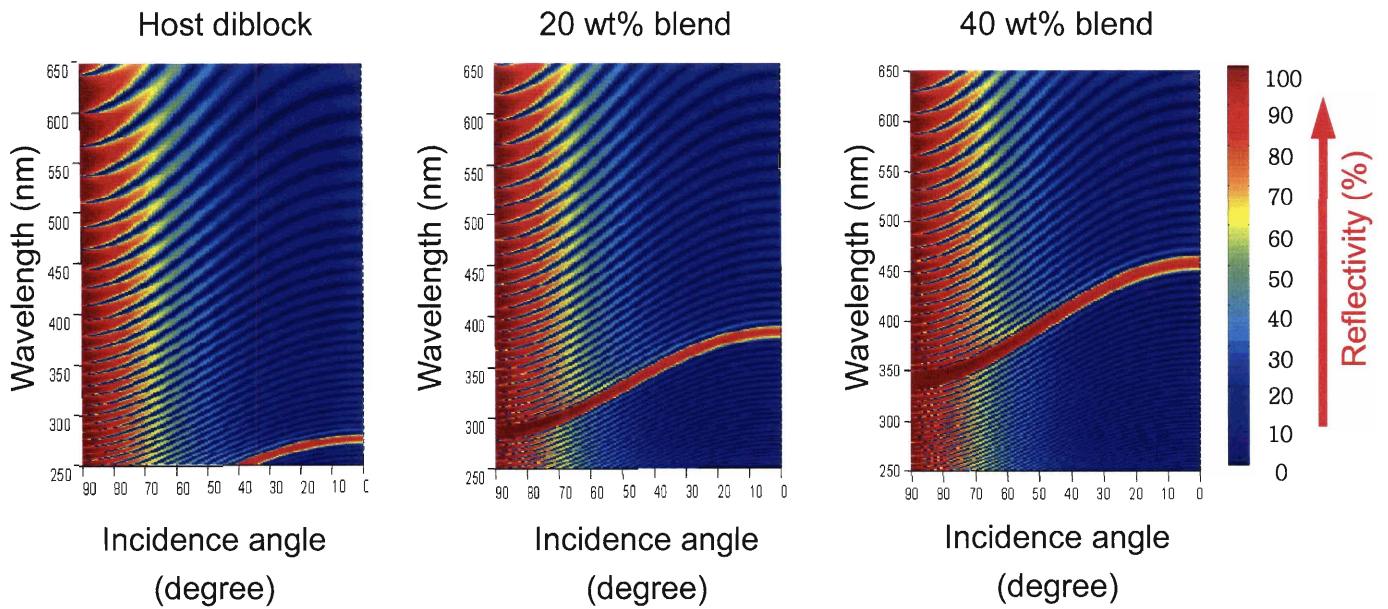


Figure A.10: Calculated reflectivity maps (for TE polarization of incident light) of multilayer stacks having the same layer thickness and refractive index as (a) poly[(E-co-P)-b-(E-co-N)], (b) 20 wt%, and (c) 40 wt% ternary blend as a function of the incidence angle (x-axis) and the wavelength (y-axis) of incident light, assuming that the thickness of high (E-co-N)/low (E-co-P) index layers are (a) 56 nm/35 nm, (b) 79 nm/48 nm, (c) 88 nm/64 nm as obtained from TEM, the refractive index of high/low index layer is 1.52/1.47 as obtained from ellipsometry, and a total number of 100 layers.

For further analysis of the measured reflectivity spectra, TMM calculations have been conducted based on measured domain thicknesses (from TEM) and refractive indices (from ellipsometry). Figure A.10 shows the reflectivity map for corresponding model 1-D

multilayer (100 layer) stacks of the host diblock and ternary blends for TE polarization of incident light, in which the peak reflectivity wavelengths at normal incidence are shown to be 273 nm (host diblock), 382 nm (20 wt % blend), and 456 nm (40 wt % blend), respectively. The measured reflectivity spectra of the blend samples (Figure A.9) are in reasonable agreement with the calculated reflectivity map (Figure A.10) in terms of the peak reflectivity wavelengths. As mentioned earlier, the lower values (blue-shift) of the measured peak reflectivity wavelength compared with calculated values at normal incidence of light result from the deviation of the average lamellar orientation from normal incidence. The broadness of the measured reflectivity spectra in Figure A.9 can be understood by considering the polygrained nature of the cast films containing lamellae of various domain orientations, domain thicknesses and randomly located defects. The assignment of lamellar morphologies is also supported by the obtained reflectivity spectra. Calculation of reflectivity for 2D photonic crystal of hexagonally packed cylinders having an equal periodicity to 1D lamellar structure predicts a peak reflectivity at much lower wavelength.¹⁷

A.4. Conclusion

In conclusion, we have shown that self-assembled lamellar block copolymers based on readily available olefins can be employed to create 1-D photonic structures in the visible wavelength range. With a suitable choice of a catalyst system for living olefin

polymerization, polyolefin block copolymers having a large molecular weight have been prepared with a narrow molecular weight distribution. The resulting copolymers, poly[(MCP-*co*-VTM)-*b*-(E-*co*-N)] and poly[(E-*co*-P)-*b*-(E-*co*-N)], exhibited a partial 1-D photonic bandgap with an excellent optical transparency. Random copolymerization of olefin monomers provided a means to tune the refractive index contrast and to suppress the crystallinity of the polyolefin block copolymers. Ternary blending of the diblock copolymers with homopolymers further afforded a pathway to control the accessible peak reflectivity wavelength of the polyolefin based photonic structures. Further studies for improvements over the current system including the effect of selective fluorination on the morphology and optical properties of polyolefin block copolymers are underway.

A.5. References

1. Galli, P.; Vecellio, G. "Polyolefins: The most promising large-volume materials for the 21st century" *Journal of Polymer Science Part a-Polymer Chemistry* **2004**, *42*, 396-415.
2. Coates, G. W.; Hustad, P. D.; Reinartz, S. "Catalysts for the living insertion polymerization of alkenes: Access to new polyolefin architectures using Ziegler-Natta chemistry" *Angewandte Chemie-International Edition* **2002**, *41*, 2236-2257.
3. Tian, J.; Hustad, P. D.; Coates, G. W. "A new catalyst for highly syndiospecific living olefin polymerization: Homopolymers and block copolymers from ethylene and propylene" *Journal of the American Chemical Society* **2001**, *123*, 5134-5135.
4. Hustad, P. D.; Coates, G. W. "Insertion/isomerization polymerization of 1,5-hexadiene: Synthesis of functional propylene copolymers and block copolymers" *Journal of the American Chemical Society* **2002**, *124*, 11578-11579.
5. Mathers, R. T.; Coates, G. W. "Cross metathesis functionalization of polyolefins" *Chemical Communications* **2004**, 422-423.
6. Wang, W. J.; Zhu, S. P. "Structural analysis of ethylene/propylene copolymers synthesized with a constrained geometry catalyst" *Macromolecules* **2000**, *33*, 1157-1162.
7. Hustad, P. D.; Tian, J.; Coates, G. W. "Mechanism of propylene insertion using bis(phenoxyimine)-based titanium catalysts: An unusual secondary insertion of propylene in a group IV catalyst system" *Journal of the American Chemical*

- Society* **2002**, 124, 3614-3621.
8. Tritto, I.; Marestin, C.; Boggioni, L.; Zetta, L.; Provasoli, A.; Ferro, D. R. "Ethylene-norbornene copolymer microstructure. assessment and advances based on assignments of C-13 NMR spectra" *Macromolecules* **2000**, 33, 8931-8944.
 9. Yoshida, Y.; Mohri, J.; Ishii, S.; Mitani, M.; Saito, J.; Matsui, S.; Makio, H.; Nakano, T.; Tanaka, H.; Onda, M.; Yamamoto, Y.; Mizuno, A.; Fujita, T. "Living copolymerization of ethylene with norbornene catalyzed by bis(pyrrolide-imine) titanium complexes with MAO" *Journal of the American Chemical Society* **2004**, 126, 12023-12032.
 10. Bonse, U.; Hart, M. "*Zeitschrift fur Physik* **1966**, 189, 151.
 11. Brandrup, J.; Immergut, E. H.; Grulke, E. A., *Polymer Handbook*. 4 ed.; Wiley-Interscience: 1999.
 12. Haselwander, T. F. A.; Heitz, W.; Krugel, S. A.; Wendorff, J. H. "Polynorbornene: Synthesis, properties and simulations" *Macromolecular Chemistry and Physics* **1996**, 197, 3435-3453.
 13. Born, M.; Wolf, E., *Principles of Optics, 7th edition*. Cambridge University Press: Cambridge, 1999.
 14. Osuji, C.; Chao, C. Y.; Bitá, I.; Ober, C. K.; Thomas, E. L. "Temperature-dependent photonic bandgap in a self-assembled hydrogen-bonded liquid-crystalline diblock copolymer" *Advanced Functional Materials* **2002**, 12, 753-758.